Dynamic Actuation Properties of Ni–Mn–Ga Ferromagnetic Shape Memory Alloys

by

Christopher P. Henry

B.S., Materials Science and Engineering, Mechanical Engineering,
University of California at Davis, 1997

M.S., Materials Science and Engineering,
Massachusetts Institute of Technology, 2000

M.S., Technology and Policy Program,
Massachusetts Institute of Technology, 2000

Submitted to the Department of Materials Science and Engineering in
Partial Fulfillment of the Requirements for the Degree of

Doctor of Philosophy in Materials Engineering

at the
Massachusetts Institute of Technology

June 2002

Signature of Author.....
Department of Materials Science and Engineering
May 22, 2002

Certified by.....
Samuel M. Allen
POSCO Professor of Physical Metallurgy
Thesis Supervisor

Certified by.....
Robert C. O'Handley
Senior Research Associate
Thesis Supervisor

Accepted by.....
Harry Tuller
Chairman, Departmental Committee on Graduate Students

Dynamic Actuation Properties of Ni–Mn–Ga Ferromagnetic Shape Memory Alloys

By Christopher P. Henry

Submitted to the Department of Materials Science and Engineering on May 22nd, 2002
in partial fulfillment of the requirements for the Degree of
Doctor of Philosophy in Materials Engineering

at the

Massachusetts Institute of Technology

May 2002

ABSTRACT

Dynamic magnetic-field-induced strain actuation of up to 3% with a frequency bandwidth of least 500 Hz in $Ni_{48.5}Mn_{29.5}Ga_{21}$ ferromagnetic shape memory alloys (FMSAs) is achieved. Hardware was designed and constructed to measure frequency bandwidth, magnetic-field-induced strain, stress and magnetization driven from an applied magnetic field. The bandwidth in this investigation was only limited by inductive reactance of the hardware, not by fundamental limitations of Ni–Mn–Ga. Degradation of the peak dynamic actuation strain occurred from 3.0% to 2.6% with increasing number of cycles from $N\approx1{,}000$ to $N\approx100{,}000$.

Measurement of strain, stress, and magnetization driven by a magnetic field permitted the comparison of measured properties versus properly defined thermodynamic properties. The peak thermodynamic piezomagnetic coefficient is $d_{31}|_{\sigma} = 2.5\times10^{-7}\,\mathrm{m/A}$ compared to the experimental slope, $\partial\varepsilon/\partial H$, of 1.0×10^{-7} m / A at $N\approx1{,}000$ cycles and 1.4×10^{-7} m / A at $N\approx100{,}000$ cycles, respectively. The thermodynamic piezomagnetic coefficient is five times greater than Terfenol-D with $d_{31} = 5.0\times10^{-8}\,\mathrm{m/A}$. The magnetic susceptibility varies between 3–10, while the twinning stiffness varies between 30–40 MPa within the average bias stress range of 0.3 to 2.8 MPa. At optimum fields and bias stresses, the mechanical energy density during cyclic deformation was 65 kJ/m^3 at the expense of 20 kJ/m^3 lost

An important first observation of dynamic stress vs. field behavior is understood by an extension of a magnetomechanical phenomenological model. The mechanism of stress generation is thought to be magnetization rotation causing negative magneto-striction with quadratic magnetic-field dependence ($\sigma \propto h^2$) before twin boundaries move. Above the threshold field for twin boundary motion, stress increases in proportion to the magnetic-field-induced strain ($\sigma \propto 2K_u h(1-h/2)/\varepsilon_0$).

Dynamic actuation measurements performed here help put Ni–Mn–Ga FSMAs into perspective with other active materials performance: Ni–Mn–Ga FSMAs are between low bandwidth, high strain, Nitinol and high bandwidth, low strain Terfenol-D and ferroelectrics.

Thesis Supervisor: Samuel M. Allen

Title: POSCO Professor of Physical Metallurgy

Thesis Supervisor: Robert C. O'Handley

Title: Senior Research Associate

ACKNOWLEDGMENTS

I like to express my gratitude to my advisor Sam Allen, for his support and guidance, through my years at MIT. Sam is always willing to spend time helping me sort through my ideas and voicing different considerations. I am also very grateful to Bob O'Handley for being an outstanding advisor. He has a keen sense of exactly what I need and how I should be guided. His patience and acute insights to problems inspire me to continue exploring the unknown world with persistence and confidence. Both have given me a great deal of freedom to pursue my research in my own way, for which I am grateful. I am eternally indebted to David Bono for his electronics wizardry, insightful design decisions and helpful discussions. I am privileged to have worked for Sam, Bob, and with David, without them I would not have reached the successful completion of my thesis.

I want to thank all the members of the Magnetic Materials Group for providing me with such a productive but entertaining environment in which to conduct research. My labmates, Miguel Marioni, Jorge Feuchtwanger, Zil Lyons, Marc Richard, Ryan Wagar, Kate Jenkins, Robin Ivester, Julee Hong, Jessica Dai, Ania Szary, Pablo Tello, Xue-Jun Jin, David Paul, and David Bono have all contributed to making my experience at MIT one I will not forget.

Special thanks are due to my wife and best friend, Julianne, for her patience, love and encouragement throughout my graduate student years. As always, she is a constant source of inspiration, strength and moral support. Finally I like to thank my parents, to whom this thesis is dedicated, for their continuous love and encouragement. They have instilled in me all that I needed to be successful in life's endeavors.

TABLE OF CONTENTS

LIST OF FIGURES

GLOSSARY

Active material: A material that converts energy from one form to another.

Actuator: A device that converts input energy to useful output with a large response of an extensive, dependent variable (such as magnetization or strain) excited by an intensive, independent variable energy (such as field or stress).

Coercivity: (= coercive field) The magnetic field difference of a particular dependent variable, bi-valued state. Commonly used here is the strain vs. field coercive field, not magnetization.

Cyclic behavior: Steady-state, cyclic response of the dependent variable due to the application of an independent variable at a specific frequency.

DATS: Dynamic actuation testing system. The integrated hardware and software to measure the mechanical and magnetic independent and dependent variables simultaneously during dynamic actuation.

Dependent variable: Those variables whose values follow from the independent variables.

Loss tangent: (= loss tangent) A measure of the hysteresis and energy loss during cyclic behavior. It is the tangent of the phase difference between the dependent variable and the independent variable. See Appendix B.

Dynamic properties: (= cyclic or AC properties) The characteristics (usually differential ratios) of dependent to independent variables at a specific cyclic frequency. Though in the context of the time-response

Extensive variable: Usually a variable whose value is related to a physical phenomenon in the material and whose magnitude and direction is proportional to the mass or volume. In this research, magnetization, M, and displacement are extensive variables.

Fatigue: Cycle-number dependence of a material's mechanical response.

Free behavior: Uncontrolled (or free) variation of all variables of the material in response to an applied stimulus. Such behavior is found in a device, though engineered devices are usually designed to remain within limits.

Frequency bandwidth: (=bandwidth) The range of input frequencies over which a desired response occurs.

Frequency response: The output response characteristics over a range of input frequencies.

FSMA: Ferromagnetic shape memory alloy

Hysteresis: A generic term indicating a process that has a bi-valued dependent variable on a closed cycle of an independent variable; generally indicates energy loss per cycle.

Independent variable: Those parameters or variables directly set by the observer in an experiment. Their values govern the values of the dependent variables.

Intensive variable: Usually a field variable whose value is independent of the material mass or volume. Usually its magnitude and direction can be easily controlled and therefore usually is the independent variable or stimulus. In this research, magnetic field, H, and stress, σ, are the intensive variables.

Loss tangent: See loss tangent and Appendix B for mathematical derivation.

MFIS: Magnetic field-induced strain

Path dependent properties: The values of the dependent variable state may be different depending on the path independent variables take to get to the state. Consider a point on a 3-D surface representing the value of the dependent variable and the x- and y-coordinates are the values of two independent variables. The slope of the surface (a measure of the property) in the x-z plane may be different than the slope in the y-z plane, or another arbitrary vertical plane. Thus, the value of the property depends upon the direction, or path, of approach.

Phenomenological model: Model that simply relates independent and dependent variables without description of a microscopic mechanism. One such model is presented here for FSMAs in Chapter 5.

Phonon: A quanta of energy in which electrons move in resonance with lattice vibrations. This provides a way to couple (2^{nd} order) properties (from electrons) to heat energy loss (lattice vibrations).

Quality factor: The mechanical quality factor is equal to the natural frequency divided by the frequency width at 3 dB less than the maximum amplitude. (See appendix B)

Resonant frequency: (=natural frequency) The frequency at which a system or material resonates with little input energy or driving force.

Sensor: A device that amplifies a small change in an applied variable producing a large response in another variable.

Slip: Deformation process by which atoms move by shear displacements.

SMA: Shape memory alloy. Its thermoelastic nature is implied and distinguished from FSMA.

Specific damping capacity: A ratio of the specific energy loss divided by the specific energy input during cyclic behavior. It is related to the loss tangent by a factor of $1/2\pi$.

Static properties: (= static behavior) The characteristics of output responses under quasistatic conditions.

Thermodynamic behavior: Constrained variation of several variables in response to an applied stimulus. Measured behavior of this sort is the result of careful material preparation or experiment / device design.

Training: A cyclic process to improve the strain performance or the twin-boundary yield stress of the material.

Transducer: A device that converts energy from one form to another.

Twinning: Deformation process by which atoms shear in a coordinated way creating a mirror image of atomic positions across the twin-boundary.

Type 1 variant: (=variant 1) A martensite, variant orientation with its *c*-axis parallel to the applied magnetic field direction. Schematically shown in Figure 2.2.

Type 2 variant: (=variant 2) A martensite variant orientation with its *c*-axis orthogonal to the applied magnetic field direction and parallel to the longitudinal strain direction. Schematically shown in Figure 2.2.

Chapter 1

1 Introduction to Ni–Mn–Ga Ferromagnetic Shape Memory Alloys and Performance Properties

Active materials transduce an input stimulus into an output response. By integrating active materials with a controllable feedback mechanism into a device, actuators and sensors can monitor, regulate, react, or control a property of a larger system. In order to integrate these "intelligent structures" into applications, issues related to performance, reliability, robustness, and manufacturability need to be resolved [1]. Of the many types of actuators and sensors, this work focuses on Ni–Mn–Ga ferromagnetic shape memory alloys (FSMA) that deform in response to an applied magnetic field by twin-boundary motion in the martensite phase. Murray *et al.* [2] achieved a near-theoretical maximum magnetic field-induced strain (MFIS) of 6.1% resulting from reorientation of martensite variants under static load and quasi-static magnetic field conditions. The present thesis concentrates on cyclic dynamic measurements associated with large field-induced strain.

The usual measures of active material performance are strain response properties, output mechanical work, coupling energy efficiency, and frequency bandwidth. Other important engineering characteristics are robustness, reliability, and manufacturability. Robustness is an indicator of how damage resistant and fault tolerant the actuator is under different operating conditions. Reliability can include not only a measure of the

robustness over time, but also a measure of repeatability over time. Manufacturability describes the ease with which the actuator or sensor can be made in a replicable fashion with the desired performance, robustness and reliability at a reasonable cost. All these characteristics are necessary to for a new material to gain acceptance by designers.

This work consists of characterizing the frequency bandwidth of 31-mode dynamic actuation performance and calculating dynamic actuation properties of Ni–Mn–Ga FSMAs under different operating conditions.

1.1 Overview of FSMAs

This section is a brief description of four essential material property criteria that need to coexist for a FSMA to demonstrate field-induced strain actuation. For Ni–Mn–Ga alloys composition plays an important role in determining the magnetic, structural and mechanical properties, as will be shown in section 1.2.6. Hence, achieving significant field-induced strain is limited to narrow range of compositions and with an upper temperature limit.

The first of these criteria requires that a low-symmetry phase, martensite, must exist at the actuation conditions for twinning deformation to occur. Not only is the proper martensite structure important, but also the crystallographic c/a ratio determines the maximum twinning strain. Second, the twin-boundary yield stress (σ_{tby}) must be sufficiently low, on the order of 1 MPa, as to permit the material's magnetic moments to

manipulate the twin defect structure. Third, the alloy must be ferromagnetic with a large saturation magnetization (M_s). Lastly, the magnetocrystalline anisotropy (K_u) must be sufficiently large in an easy crystallographic axis rather than an easy crystallographic plane. Without these necessary conditions, a material cannot exhibit MFIS.

First, the proper microstructural phase must exist at actuation temperatures in order for strain to occur. Due to the compositional sensitivity of the martensite transformation temperature, two microstructural phases are possible: austenite and martensite. Austenite is a generic term for a higher temperature parent phase, which is cubic crystal system in Ni–Mn–Ga. Austenite undergoes a structural transition to martensite, the generic term for a lower temperature, lower symmetry structure (tetragonal or orthorhombic in Ni–Mn–Ga). In cubic austenite, all axes are the same length, designated as *a*-axes. The four-fold rotational and mirror symmetries in each of the 3 axes do not allow for the existence of asymmetric or anisotropic second-rank tensor properties. In tetragonal martensite, however, one axis (designated the *c*-axis) becomes longer or shorter than the other two *a*-axes in austenite destroying four-fold symmetries in two axes permitting the existence of anisotropic properties. This is an illustration of a fundamental law of crystal physics known as Neumann's principle: *"The symmetry elements of any physical property of a crystal must include the symmetry elements of the point group of the crystal".*

In order for magnetic and deformation anisotropic properties to exist, Ni–Mn–Ga must be martensitic in the operating temperature range. In Ni–Mn–Ga alloys martensite can exist as any of several different martensite structures, depending on composition. Sozinov *et al.* [3], [4] and Pons *et al.* [5] are good reviews. Structure determination is usually performed via transmission electron microscopy (TEM) or x-ray diffraction (XRD). With a combination of both techniques, Sozinov *et al.* distinguish 5-layer martensite with $c < a$ permitting a maximum axial twinning strain of $\varepsilon_0 \approx |1 - c/a| \approx 6\%$ and a 7-layer martensite with $c > a$ and $\varepsilon_0 \approx 10\%$. Figure 1.1 is an illustration of the deformation caused by the formation of a twin-boundary for a tetragonal martensite with $c < a$. Thus, a low-symmetry martensite is required to permit strain response from external stresses or external magnetic fields.

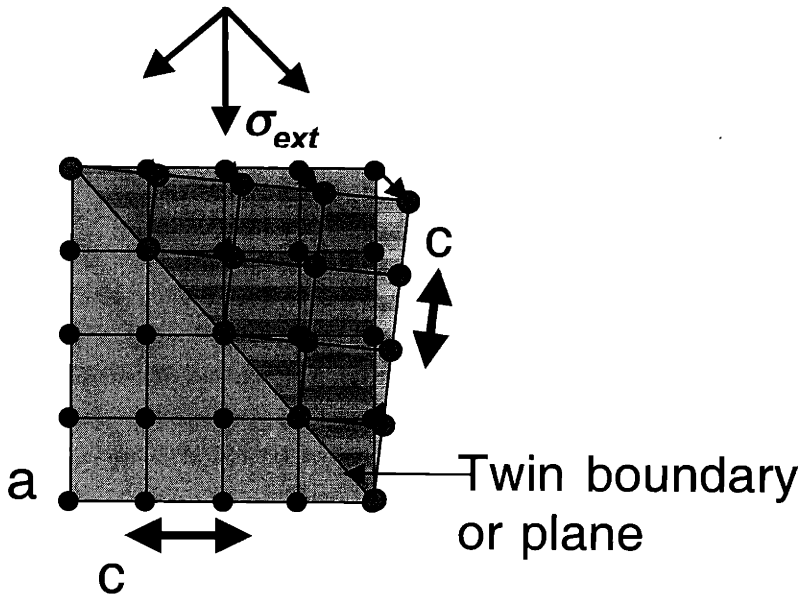

Figure 1.1: A shearing component, σ_{tb}, of an external stress causes coordinated shifting of atoms along the shear direction in the shear or twin plane. The maximum strain due to twinning in tetragonal martensite is $\varepsilon_0 = |1 - c/a|$. For $c/a = 0.94$, $\varepsilon_0 = 6\%$ and this nearly rotates the c-axis 90° across the twin-boundary.

Detection of the symmetry change from austenite to martensite or vice versa is performed by measuring a discontinuous change of an anisotropic property (e.g. resistivity or susceptibility) as the temperature increases or decreases through the transition. These methods allow differentiation between austenite and martensite as well as determination of the temperature at which the transition takes place. Figure 1.2 plots the low magnetic field magnetization during heating and then cooling versus temperature. This magnetization measurement permits detection of the martensite start and finish

transformation temperatures as well as the Curie temperature, at which the alloy becomes ferromagnetic.

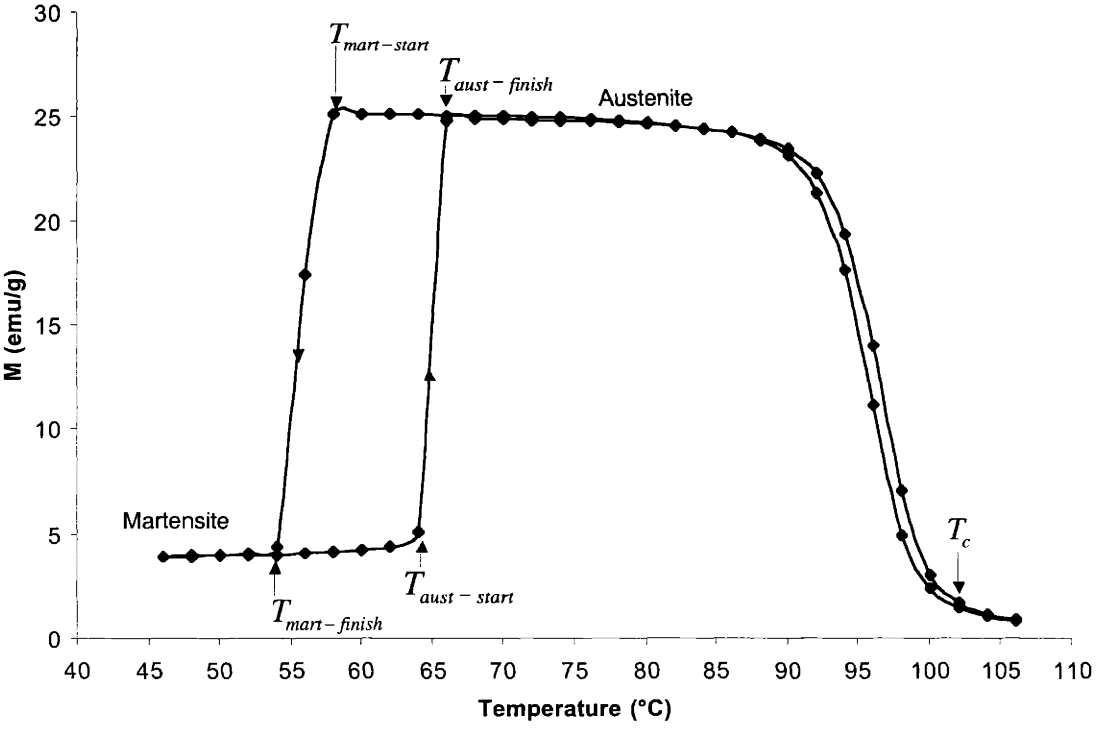

Figure 1.2: Small-field magnetization at an applied field of 100 Oe versus temperature for Ni–Mn–Ga on heating above the austenite finish temperature at 65°C and the Curie temperature at approximately 100°C, then cooling below the finish transformation temperature at approximately 55°C. Note the temperature hysteresis for the heating versus cooling transformation.

The second requirement is that twinning be the preferred mode of martensite deformation and that it be achievable at stresses low enough to permit a magnetic field to affect its motion. Figure 1.3 schematically shows the stress and temperature conditions under which different deformation mechanisms occur. These mechanisms are primarily

dislocation multiplication, slip and twinning. If the stress and temperature are low enough, twinning becomes a more favorable deformation mechanism than slip. The primary difference between slip and twinning is that shear deformation associated with slip can occur in positive or negative direction along a shear crystallographic direction with dislocations moving along it in an uncoordinated and independent way. While for twinning, shear is accomplished by a coordinated movement of non-annihilating partial dislocations and is, therefore, limited to one sense of the shear direction.

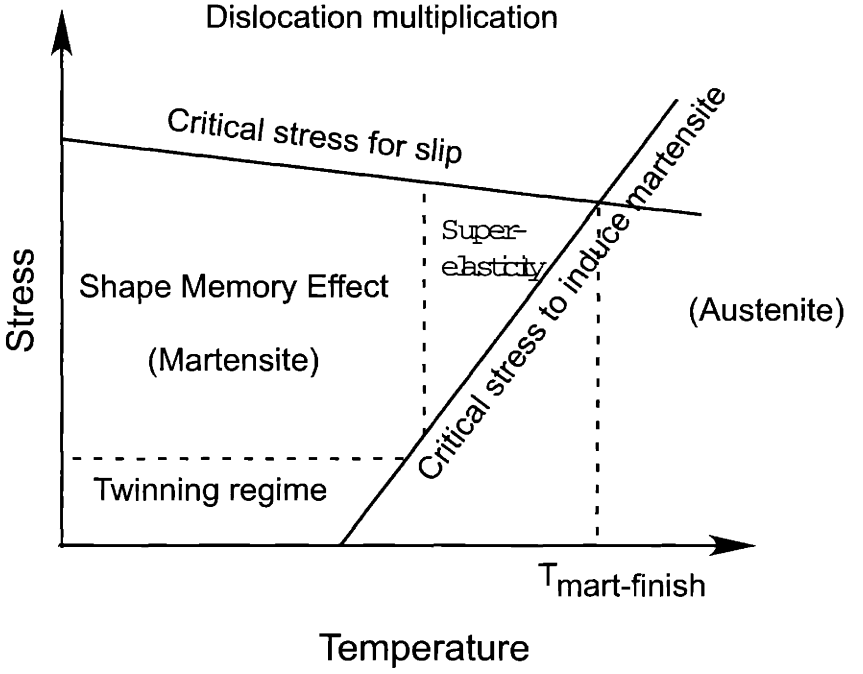

Figure 1.3: Map of the regimes of shape memory mechanical behavior (*from Otsuka and Wayman*). The slope of the "critical stress to induce martensite" is about 2.5 MPa / K for Ni–Mn–Ga according to [6].

For some tetragonal intermetallic compounds twinning is often the preferred mode of deformation possible at relatively "high" temperatures (i.e. up to 600K [7]). Not

only is this is true of Ni–Mn–Ga alloys, but twinning occurs at very low stresses. The "yield" stress at which twinning initiates (from here on, this is referred to as the twin-boundary yield stress) is so low that magnetic forces acting on a twin-boundary can exceed the yield stress.

The magnitude of the saturated magnetic moment is the third necessary ingredient because it, in part, determines the maximum possible magnetic energy storage in the FSMA available for actuation. The magnitude of the saturated magnetic moment is determined from a magnetization versus applied field plot measured with a vibrating sample magnetometer as illustrated in Figure 1.4. It shows magnetization from an applied field in two different directions 90° apart as seen in the figure inset. This measurement was performed on a disk with a composition of $Ni_{48.75}Mn_{31.75}Ga_{19.5}$ that contains a single variant with the *c*-axis oriented in the plane of the disk.

If the field is applied in the same direction as the easy axis, only a small amount of energy storage is possible. When the field is applied in the hard-axis direction, the magnetization rotates into the field direction gradually, storing much more energy than easy-axis magnetization. The origin of the anisotropic magnetization behavior results from the reduced symmetry of Ni–Mn–Ga martensite. The difference between the hard- and easy-axis magnetization is a measure of the strength of the magnetocrystalline

anisotropy. The difference in energy stored between the hard- and easy-axis curves in Figure 1.4 is the magnetocrystalline anisotropy energy, K_u.

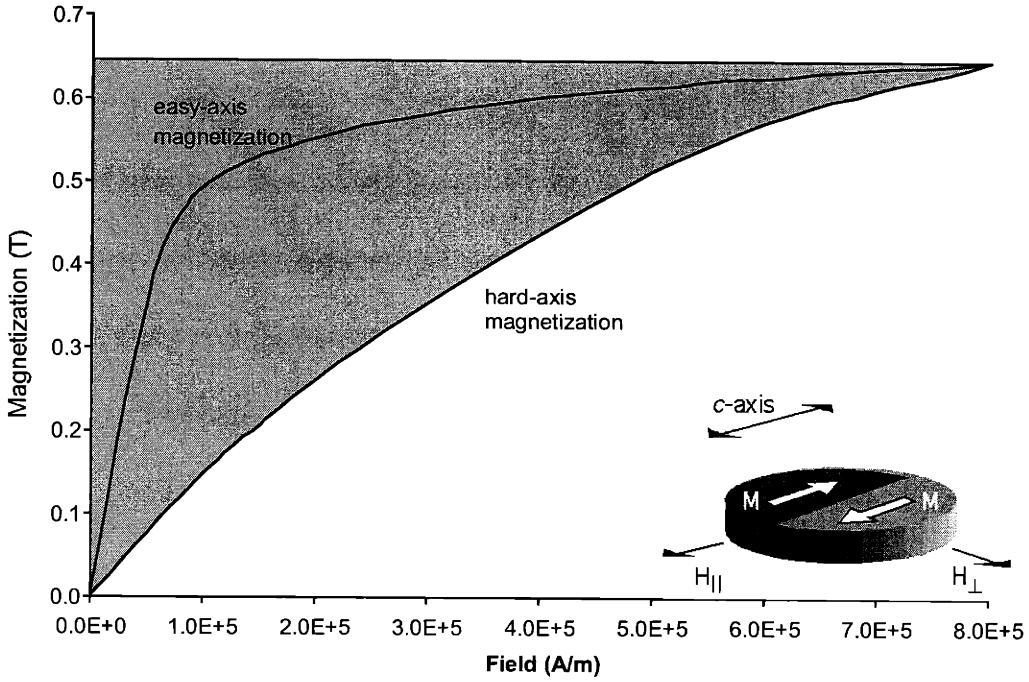

Figure 1.4: Magnetization (uncorrected for demagnetization effects) versus field plot at two different orientations: field parallel and perpendicular to the magnetization in a circular disk of $Ni_{48.75}Mn_{31.75}Ga_{19.5}$. The shaded area represents the magnetic energy density storage during hard-axis magnetization.

A strong magnetocrystalline anisotropy energy is the fourth and key ingredient enabling magnetic field energy to couple to the crystal structure. This permits mechanical deformation via twinning in Ni–Mn–Ga to relieve the storage of magnetic energy. The magnetocrystalline anisotropy was measured in single crystals of Ni-Mn-Ga by Ullakko *et al.*, Murray, and Tickle and James. Ullakko *et al.* determined the anisotropy to be 0.12

MJ/m^3 from magnetization curves at 265 K. Murray also calculated the magnetocrystalline anisotropy energy to be 0.16 MJ/m^3 from magnetization curves at room temperature. Tickle and James [23] used a mechanically constrained sample in a single-variant state to measure the anisotropy and found it to be 0.245 MJ/m^3 at a temperature of 256 K.

In the limit of a large magnetocrystalline anisotropy energy, calculations by Paul *et al.* [8] show that the equilibrium position of a twin-boundary coincides with the domain wall. Furthermore, observations by De Graef *et al.* [9] confirm magnetic domain walls to coincide with the twin-boundary through TEM studies. Thus, twin-boundary motion can be intimately connected to the direction and magnitude of the magnetization through the magnetocrystalline anisotropy energy. This correspondence between the twin-boundary and the domain wall may inform the mechanism of actuation and possibly point to sources of energy loss in the coupled motion of these microstructural boundaries.

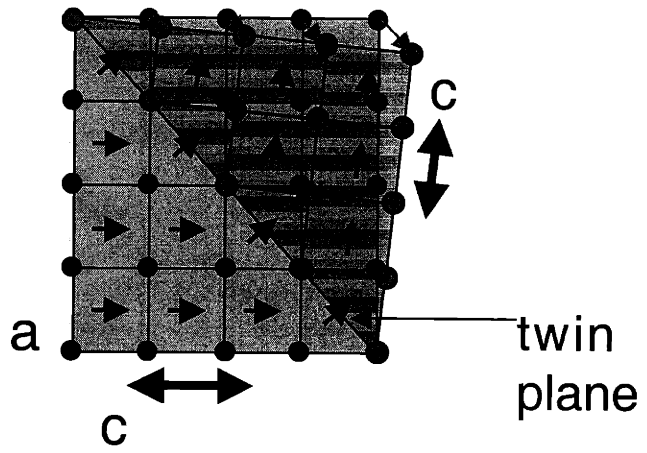

Figure 1.5: Large magnetocrystalline anisotropy energy causes magnetic moments to align with the *c*-axis on either side of the twin plane creating a 90° domain wall in martensitic Ni–Mn–Ga.

In the case of martensitic Ni–Mn–Ga, large magnetocrystalline anisotropy causes magnetic moment alignment with the *c*-axis on either side of the twin-boundary as illustrated in Figure 1.5. The stored magnetic energy due to hard-axis magnetization puts pressure on the twin-boundary until the twin-boundary yield stress is achieved. Once twin-boundary motion occurs, the stored energy is used for MFIS actuation. Further energy storage, and no actuation, occurs if twin boundaries are pinned on defects preventing the twin-boundary from sweeping through the entire material.

The importance of the above four requirements is clear:

- The proper microstructure permits crystallographic anisotropy ($c \neq a$) and magnetic anisotropy.

- The ease with which Ni–Mn–Ga alloys form twins is unusual and permits their movement via a magnetic field.
- The magnetization magnitude helps generate sufficient magnetic forces within the material.
- The magnetocrystalline anisotropy energy is a magnetic stiffness that aligns the magnetic moments with the crystal structure. It allows sufficient stress to be transmitted to the crystal structure to yield in shear along twinning planes.

1.2 Review of FSMAs and active materials in literature

Numerous authors have contributed their understanding to this unique alloy system, Ni–Mn–Ga. Their contributions are noted in a history of the development of MFIS. Though the development of advances and understanding of FSMAs has been dramatic thus far, a comprehensive review would be too voluminous. The reader is also referred to Murray [10] as he reviewed an extensive body of work contributing to the understanding of Ni–Mn–Ga. Other active materials are reviewed so the similarities and differences in the mechanisms of actuation can be noted and correlated with performance maps at the end of the section. In this way the results presented in Chapter 3 can be put into context with other active materials.

There is not a one-size-fits-all material for every application. Different applications require different performance characteristics and therefore utilization of

different materials technologies. Characterization of performance characteristics for different active materials illuminates their strengths and weaknesses. These strengths and weaknesses depend heavily upon the mechanisms of actuation. In classifying and understanding existing mechanisms causing actuation FSMAs can be put into the proper context among other active materials.

Three classes of materials that show similarities to FSMAs are magnetostrictive materials, shape memory alloys, and relaxor ferroelectrics. Magnetostrictive alloys, such as Terfenol-D, generate strains in reaction to a magnetic field stimulus via magnetostriction, a different mechanism than FSMAs. SMA mechanical response occurs via atomic shear displacements (driven by a transformation to martensite) while FSMAs also undergo shear displacements driven by a magnetic field. Relaxor ferroelectrics are close electric field analogs of FSMAs except that the actuation occurs via electrostriction. The differences from FSMAs are elucidated in the three sections following the history of Ni–Mn–Ga.

1.2.1 History of Ni–Mn–Ga

The history of FSMAs started in 1988 when V. A. Chernenko and V. V. Kokorin independently made samples of Ni–Mn–Ga alloys in the Ukraine based upon Webster's paper [11] in 1984. Chernenko sent some of his samples to Moscow to be tested and simultaneously, Kokorin sent his samples to K. Ullakko in Finland to be tested. Kokorin

and Martynov published their findings on thermally- and stress-induced martensite in single crystals in 1992 [12] and presented them jointly with Chernenko in the United States [13]. They continued to collaborate with Spanish researchers, E. Cesari, J. Pons, and C. Seguí in the late 1990's with much research focusing on characterization of premartensite and martensite structures and their temperature dependent properties [6, 14, 15, 16, 17, 18, 19]. Chernenko and Kokorin pursued further research on premartensite structures resulting from TA_2 phonon softening of Ni–Mn–Ga with other Spanish researchers Ll. Manosa, A. Gonzalez-Comas, E. Obrado, A. Planes [20]. Because of this extensive research on martensite, Ni–Mn–Ga is known to have unique softening characteristics that lend itself to readily twinning in a magnetic field.

R. D. James started investigating FSMAs in 1992 after Chernenko's presentation [21, 22, 23, 24]. James and Wuttig wrote about the possibility of inducing strain magnetically in a shape memory alloy if the alloy had sufficient magnetic moment and had high magnetocrystalline anisotropy. The excitement brought forth by high performance FSMAs has prompted research around the world.

Ullakko worked in R. C. O'Handley's group at M.I.T. in 1996 and made the first MFIS measurements of 0.2% in $Ni_{50}Mn_{25}Ga_{25}$ at a temperature of –8°C in a [001] oriented single crystal grown by Kokorin [25, 26]. Ullakko also wrote on FSMA's potential as an actuator material [27, 28]. Following the success of Ullakko *et al.*, James

and Wuttig [29] observed a 0.5% strain in $Fe_{70}Pd_{30}$ at –17°C in 1998 and subsequently Tickle and James [30] saw 1.3% in $Ni_{51.3}Mn_{24.0}Ga_{24.7}$ below 0°C. Later, James *et al.* reported 4% MFIS in $Ni_{50.3}Mn_{24}Ga_{24.7}$ measured at 12 kOe and was the first to report 0.5% MFIS with a magnetic field cycle [31]. Pasquale *et al.* also measured strain 1.2×10^{-4} connected to the presence of martensite twins for $Ni_{52.6}Mn_{24.5}Ga_{22.5}$ [32]. Murray *et al.* observed 0.2% MFIS at –8°C and 8 kOe in 1998 [33]. In 1999, Murray *et al.* achieved 5% shear strain at room temperature in a field of 4 kOe in a Ni–Mn–Ga single crystal sample [34]. Murray *et al.* observed MFIS of 2.2% and cycled a single crystal to 1.5% at 1.16 MPa in $Ni_{49.4}Mn_{29.7}Ga_{20.9}$ [35]. Murray *et al.* also reported 6% MFIS that is blocked by a compressive stress of 2 MPa in $Ni_{49.8}Mn_{28.5}Ga_{21.7}$[2]. Ullakko has also reported strain of 5.5% in $Ni_{49.3}Mn_{30.2}Ga_{20.4}$ [36] and 5% in $Ni_{48}Mn_{31}Ga_{21}$ at 26°C [37]. These strains are approaching the theoretical *c/a* limit and significant further increases in MFIS are not expected.

The magnitude of MFIS varies greatly because of high compositional sensitivity of structural, mechanical, and magnetic properties in the Ni–Mn–Ga system. It is important to notice that the compositions of these functioning alloys vary widely in Mn and Ga content, ranging from 25–32% and 25–19% respectively. The Ni content is confined to a tight range around 50%, with only about 3% variance in samples that show field-induced strain. K. Ullakko started Adaptamat Inc. in Finland to develop this

material and to integrate Ni–Mn–Ga FSMAs into actuator applications. He continues to address issues related to manufacturing and commercialization, the most significant being compositional control. At M.I.T. O'Handley, Murray, Marioni, and others have continued to explore the performance limits of Ni–Mn–Ga FSMAs in recent years.

1.2.2 MAGNETOSTRICTIVE MATERIALS

Magnetostriction usually implies an anisotropic magnetoelastic effect that associates a stress with the rotation of the magnetization vector, $\boldsymbol{M}$, causing an anisotropic mechanical strain by the relation 1.1:

$$e = \tfrac{3}{2}\lambda_s(\cos^2\theta - \tfrac{1}{3}) \qquad 1.1$$

where e is the magnetostrictive strain, λ_s is the saturation magnetostrictive strain, and θ is the angle between the magnetization, M, and the magnetic field, H. The stress developed as a result of the magnetostrictive strain is given by the magnetic stress tensor, B_{ij}. Also called the magnetoelastic coupling coefficient, it is related to the magnetostrictive strains by $B_{ij} \propto -c_{ijkl}\lambda_{kl}$. The microscopic origin of magnetostriction is due to anisotropic magnetic interactions with the atoms on the lattice. Because of this anisotropy, the crystal may be able to lower its energy by changing the equilibrium lengths of atomic bonds. Examples from O'Handley [38] of magnetostrictive parameters for BCC-iron are $\lambda_{111} = -21.5\times10^{-6}$ and $B_1 = -2.9\times10^{6}$ MPa, while for $TbFe_2$ $\lambda_{111} = 2600\times10^{-6}$ and $B_1 = 156\times10^{6}$ MPa.

It is understandable that subtle changes in atomic bond length might be responsible for only small strains while the strong interatomic forces can produce tremendous external stresses. Magnetostrictive materials require only modest magnetic fields to change the crystal energy (~100–800 kJ/mol) and cause changes in the magnitude of interatomic forces. If the bond energy only changes by a fraction of the total energy, the resulting forces are still quite large. This actuation mechanism differs dramatically from FSMAs and as a result, the magnitudes of the stresses and strains are much different.

Magnetostrictive alloys such as Terfenol-D are promising active materials for sonar and ultrasonics because of the mechanical work they can accomplish. The following are some of the properties most commonly reported for Terfenol-D actuators. The maximum strain is about 0.005 in single crystals at 20 K [39], though more typically 0.001 at room temperature. Bias stresses for actuator operation can range from nearly zero to 70 MPa with 40 MPa being typical and bias fields up to 100 kA/m (600 Oe) with AC fields of only 50 kA/m [40]. Modulus values at constant field range from 25–35 GPa [39]. Maximum coupling coefficients, d_{33}, are about 6×10^{-8} m/A and typically 1×10^{-8} m/A and energy transduction is about 75% to a maximum of 90% [41]. Actuation frequencies can range from nearly DC to 80 kHz [42] if measures are taken to mitigate

eddy currents, with 1 kHz being typical [40]. These properties help give a sense of the operating conditions within which Terfenol-D actuation can occur.

1.2.3 Shape Memory Alloys

In Nitinol (NiTi), the thermoelastic shape memory effect is exhibited when the material is plastically deformed and then heated to restore its original shape. The concepts related to the SMA actuation process are summarized in Figure 1.6. Austenite is represented on the right-hand side of the transition temperature boundary at T_m in Figure 1.6. Martensite is represented on the left-hand side of the T_m boundary when the SMA cools through the transition temperature. In process "1" in Figure 1.6, work is done when an externally applied stress reorients martensite variants atomic shear displacements resulting in plastic deformation. When martensite is heated to austenite, the phase transformation causes the Bain and variant reorientation strains to be recovered in process "2." The material is returned to its original state when the material is cooled from shown as "3."

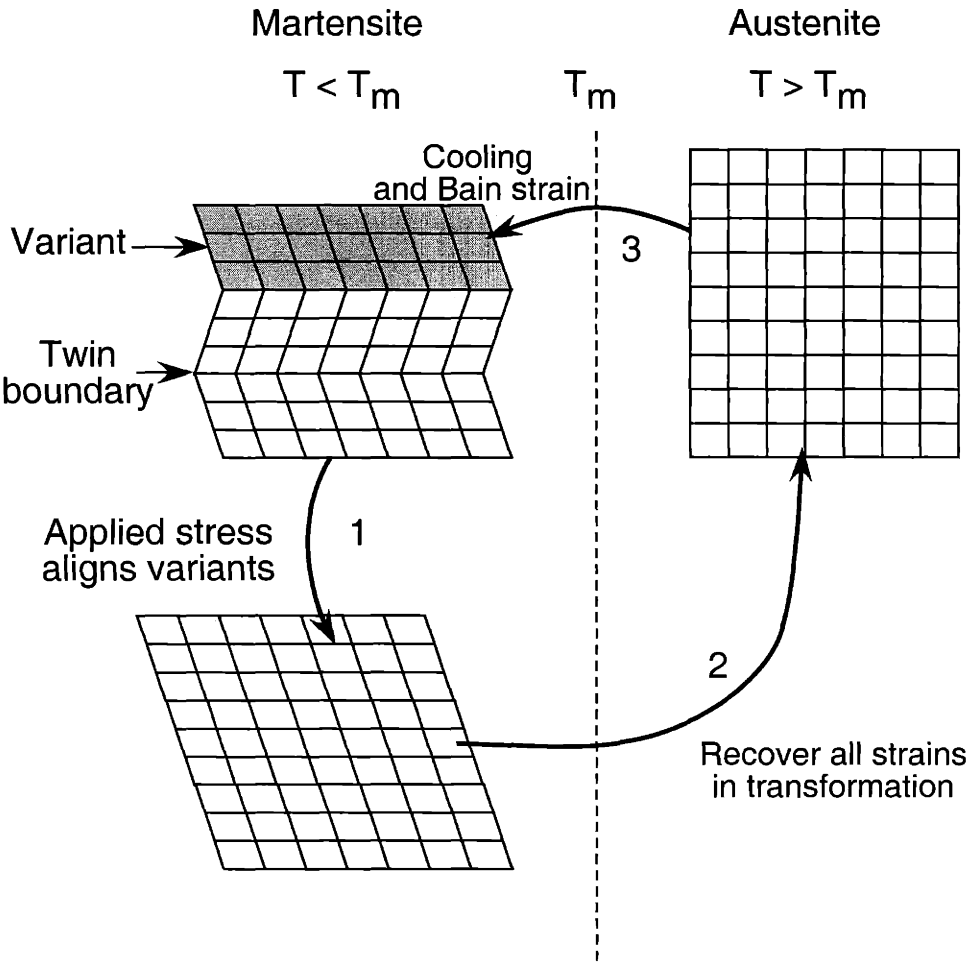

Figure 1.6: Commercial thermoelastic shape memory alloys exhibit reversible strains usually around 3–4%. SMAs deform via variant reorientation due to an applied stress in martensite, process 1. This strain is recovered when the material is heated into austenite, process 2, and then subsequently cooled back into martensite, process 3.

As a result of this mechanism, the actuation stress and strain magnitudes correspond to this transformation process. In SMAs, the transformation driving force (~100 kJ/mol) generates large stresses to deform the lattice. In comparison to FSMAs, the magnetocrystalline anisotropy forces (~1 J/mol ~100 kJ/m^3) caused by a magnetic field

are small. In thermoelastic SMAs, plastic strains can be up to 10%, but 4% is more typical after a significant number of actuation cycles.

Actuation frequencies in SMAs are limited by how quickly the transformation can occur, which is in turn limited by heat transport out of the SMA. From practical experience, the 0.01" thermoelastic SMAs wires can approach 10 Hz actuation frequencies. It is believed that the inherent hysteresis observed in stress vs. strain plots for SMAs can also apply to Ni–Mn–Ga alloys. Knowing the static and dynamic hysteretic mechanism of SMAs would inform the hysteretic loss in Ni–Mn–Ga FSMAs.

1.2.4 FERROELECTRICS

Ferroelectrics fall into three main categories: electrostrictive, piezoelectric and relaxor. Electrostrictive materials are electric-field analogs of magnetostrictive materials. Piezoelectric materials are similar to electrostrictive materials but require poling, are more stress- and orientation-dependent. Relaxor ferroelectric materials exhibit electrostriction or strain due to an electric field-induced ferroelastic domain rotation or phase transformation. Though differences exist in the actuation mechanism between these electroactive materials, they both exhibit a broad range actuation behavior.

The ranges of actuation behavior are much more dramatic for these electroactive materials. For example maximum strains of these materials can range from 0.0006 to 0.01 depending on the material and the operating conditions. Ceramic single crystals of

relaxor ferroelectrics and electrostrictors can achieve strains on the order of 1% with 1 MV/m electric fields [43]. Maximum coupling coefficients, d_{33}, are about 1.5×10^{-9} m/V and energy transduction is about 75% to a maximum of 90% However, these materials tend to have a much lower bandwidth and are much more temperature sensitive as compared to piezoelectrics, which can operate at frequencies up to 100's of kHz. The maximum stress that these materials can produce is about 150 MPa. In addition to advantages of high bandwidth, high stress and adequate strain, as insulators they are good materials to easily interface with low power electronics. Furthermore, the maturity of electroactive materials' use in applications is well ahead of any other active material mentioned here.

1.2.5 PERFORMANCE MAPS

Figure 1.7 shows the maximum strain versus maximum bandwidth for different classes of active materials. The maximum strain is related to the physical mechanism of actuation as described above. The bandwidth is the maximum frequency up to which actuation is thought to be possible. Materials that can produce higher strain rates are located in the upper right corner of this figure. Diagonal lines of constant strain rate indicate that Ni–Mn–Ga produces strain rates comparable to piezoelectrics and magnetostrictives but at strains as large as SMAs. The oval regions demarcate variations or uncertainty for these performance parameters within each class of material.

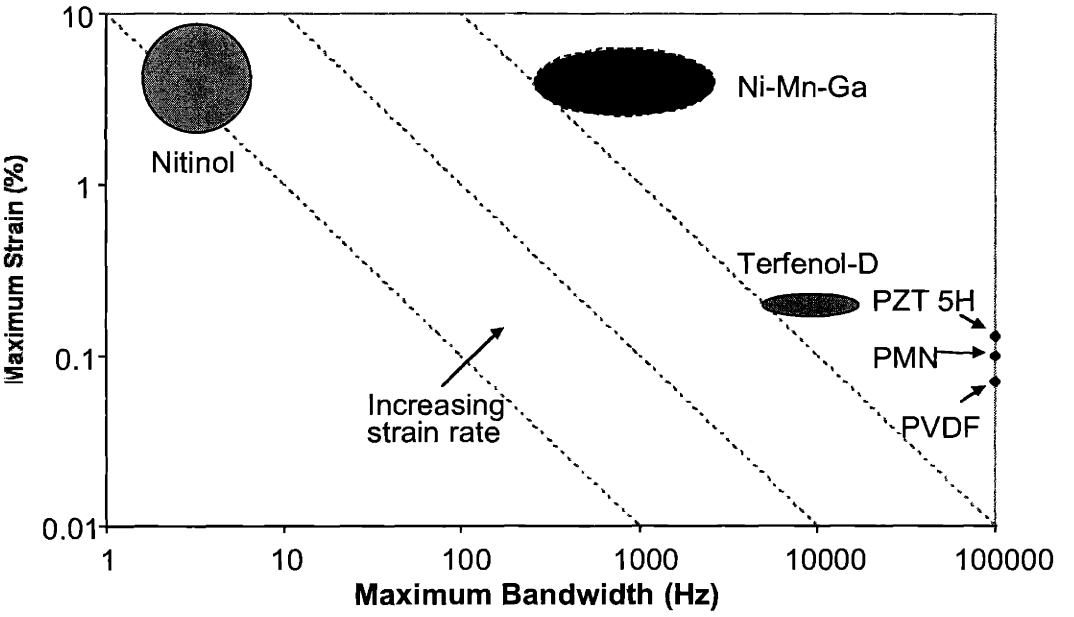

Figure 1.7: Maximum strain versus maximum bandwidth for different classes of active materials.

Figure 1.8 shows the specific energy versus the maximum bandwidth of these different classes of active materials. The energy density is equal to the mechanical work performed as the material actuates through a cycle. Diagonal lines of constant specific power indicate that Ni–Mn–Ga can provide the same specific power as SMAs, but deliver it at higher frequencies. Thus, FSMAs fill technological gap in active materials between SMAs such as Nitinol and magnetostrictives such as Terfenol-D. Application of FSMAs should be geared toward this niche with motors and valves.

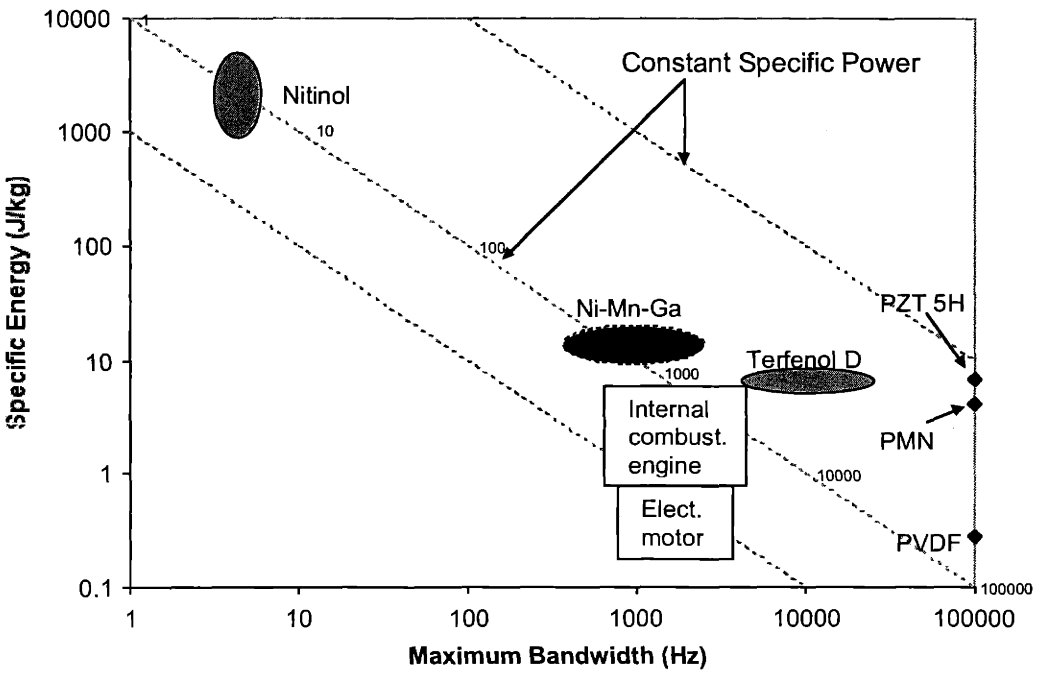

Figure 1.8: Specific energy (kJ/m^3) versus maximum bandwidth for different classes of active materials.

1.2.6 COMPOSITION PROPERTY DEPENDENCE

Though much work has been performed on martensite structures, as noted earlier, the interplay of composition with structure and properties is still an important thrust in the research of Ni–Mn–Ga. The structure of stoichiometric Ni_2MnGa as austenite is $Fm\bar{3}m$ with $L2_1$ ordering as shown in Figure 1.9. Nickel atoms occupy the sites on every other (002) plane, while the manganese and gallium atoms alternate positions on the other (002) planes in the stoichiometric structure. Below the rather composition independent Curie temperature of approximately 370K, it is well noted in literature that the Ni atoms do not carry the ferromagnetic moment, but rather the Mn atoms that are normally

antiferromagnetic carry the great majority of the magnetic moment [44]. For disproportionate amounts of Mn and Ga, this structure prefers to constrain disorder to the Mn-Ga sublattice. Increasing the Ga content will only diminish the magnetic moment density on the Mn-Ga sublattice. However, increasing the Mn concentration will force more Mn atoms to be adjacent, to couple antiferromagnetically, and therefore diminish the magnitude of the total magnetic moment. Wang *et al.* studied the effects slightly altering the stoichiometric Ni_2MnGa composition

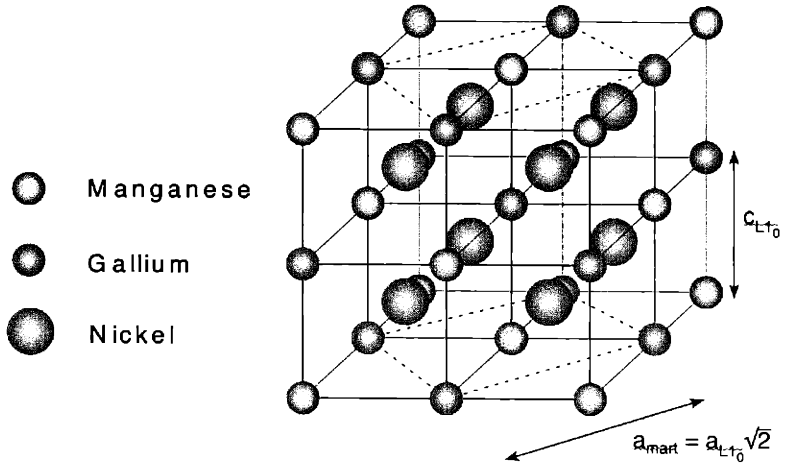

Figure 1.9: Austenitic structure of Ni_2MnGa, $Fm\bar{3}m$ symmetry with $L2_1$ ordering.

Wang *et al.* studied the effects of the composition on the magnetic and structural transitions [45]. In studying $Ni_{2+x}Mn_{1-x}Ga$ where $x = 0 - 0.2$, they found a monotonic decrease in both Curie temperature (385K down to 310K) and saturation magnetization ($4.1\mu_B$ to $3.7\ \mu_B$) with the decrease in Mn concentration. They report this is the result of not only a magnetic dilution effect by the substitution of Ni for Mn (not unlike Ga for

Mn), but also the weakening of the Mn-Mn exchange interaction caused by the increase in average Mn-Mn distance. Despite a constant Ga concentration of 25 at.%, the monotonic decrease in Curie temperature is dramatic. This implies an influence of Ni on the conduction electron concentration. Also, the martensite transition temperature monotonically increases from 200K to 320K over the same composition range.

In Wang *et al.* second alloy series, $Ni_{2-x}Mn_{1+x/2}Ga_{1+x/2}$ where $x = 0 - 0.12$, both Curie temperature (384K to 371K) and magnetic moment ($4.1\mu_B$ to $2.8\mu_B$) monotonically decrease with the simultaneous increase of Mn and Ga. They believe that this is the result of increased antiferromagnetic coupling because the average distance between Mn atoms decreases with Mn concentrations greater than 25 at.%. In addition, exchange interactions involve the polarization of conduction electrons between the disordered site occupation of Mn atoms and the concentration of Ga atoms. This indicates a strong correspondence between the atomic positions of this compound when the alloy is not at stoichiometry and its magnetic properties. Wang *et al.* give insight into why the exact composition of the Heusler structure is so important in determining macroscopic magnetic and structural properties.

Jin *et al.* [46] performed a review of Ni–Mn–Ga alloy compositions found in literature and their temperature dependent properties. Compiling and fitting the data, they found the martensite transition temperature can be evaluated as:

$$T_M(K) = 1960 - 21.1X_{Mn} - 49.2X_{Ga} \qquad 1.2$$

where X_{Mn} and X_{Ga} are mole percentages for the range of Mn: 20–35 and Ga: 18–27. In terms of the valance electron concentration, they fit the martensite transition temperature with $T_M(\mathrm{K}) = 702.5(e/a) - 5067$.

They show the saturation magnetization follows a linear dependence on the valence electron concentration as $M_S(\mu_B) = -130(e/a) + 1034$ for *e/a* ratios greater than 7.5 and $M_S(\mu_B) = 100(e/a) - 705$ for *e/a* ratios less than 7.5 in Figure 1.10.

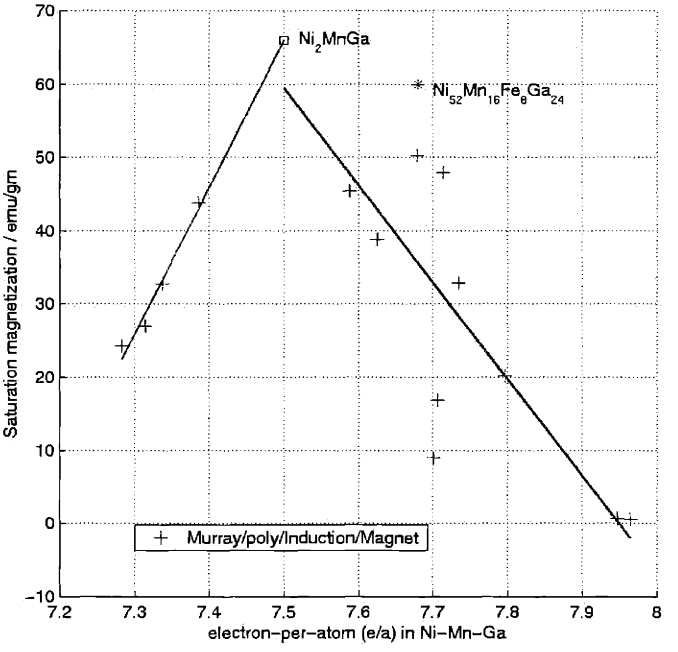

Figure 1.10: Saturation magnetization versus the electron per atom concentration for Ni–Mn–Ga alloys (*after X. Jin*).

Jin *et al.* also fit experimental Curie temperatures for different compositions to a Redlich-Kister expression. The superposition of these compositional dependencies is

plotted on an empirical composition map in Figure 1.11. The dark shaded area contains compositions where the combination of saturation magnetizations greater than 60 emu/g, Curie temperatures and martensite transition temperatures greater than 300K are all favorably high to promote MFIS actuation.

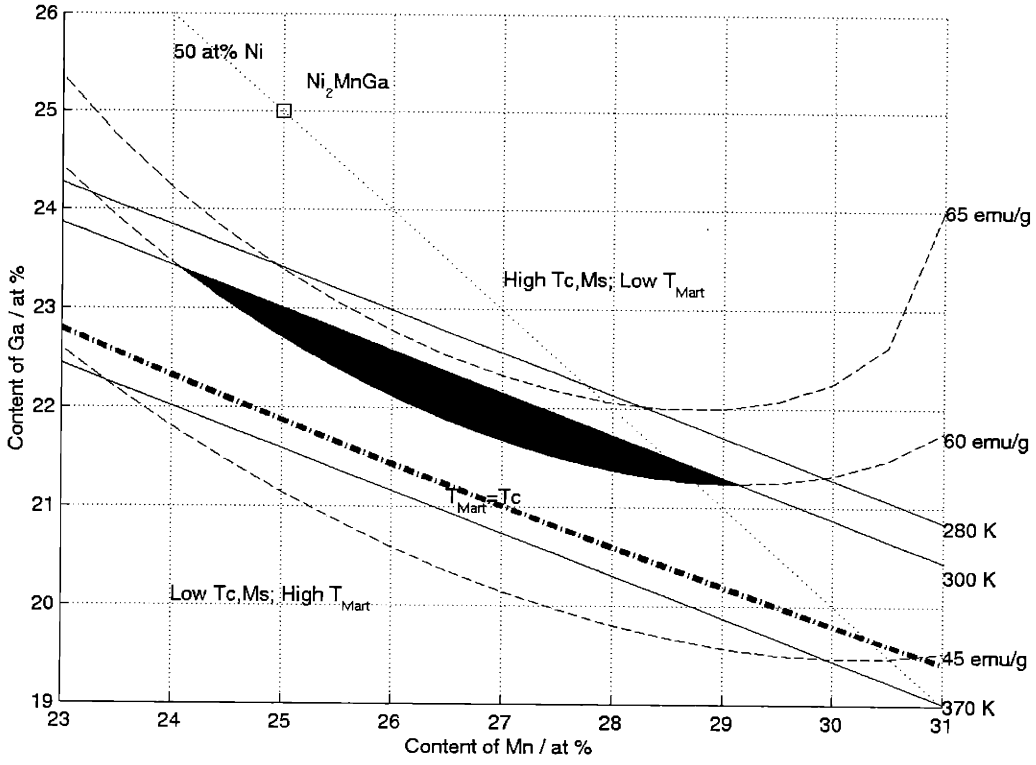

Figure 1.11: Composition map for Ni–Mn–Ga alloys of the Curie temperature, saturation magnetization, and martensite transformation temperature. (*after X. Jin*).

Mechanical properties are also drastically influenced by composition changes. Murray and Henry show in Figure 1.12 the variation of stress vs. strain behavior for

different compositions in a single crystal boule. Composition variation along the length of the boule is due to solubility limitations that reject highly diffusive elements in the alloy back into the melt during single crystal solidification, known as the Scheil effect. In this case, Mn content increases 6% at the expense of decreasing Ni 4% and Ga 2%. The net effect on the mechanical properties is the twinning strain decreases dramatically from ~6% to 0, and correspondingly, the twinning stiffness increases 15-fold from 6.25 MPa to 100 MPa. The complex role of composition in mechanical properties only adds to the compositional sensitivity of magnetic properties. Because of this fact, consistency and reliability are issues that should be resolved in commercializing this material.

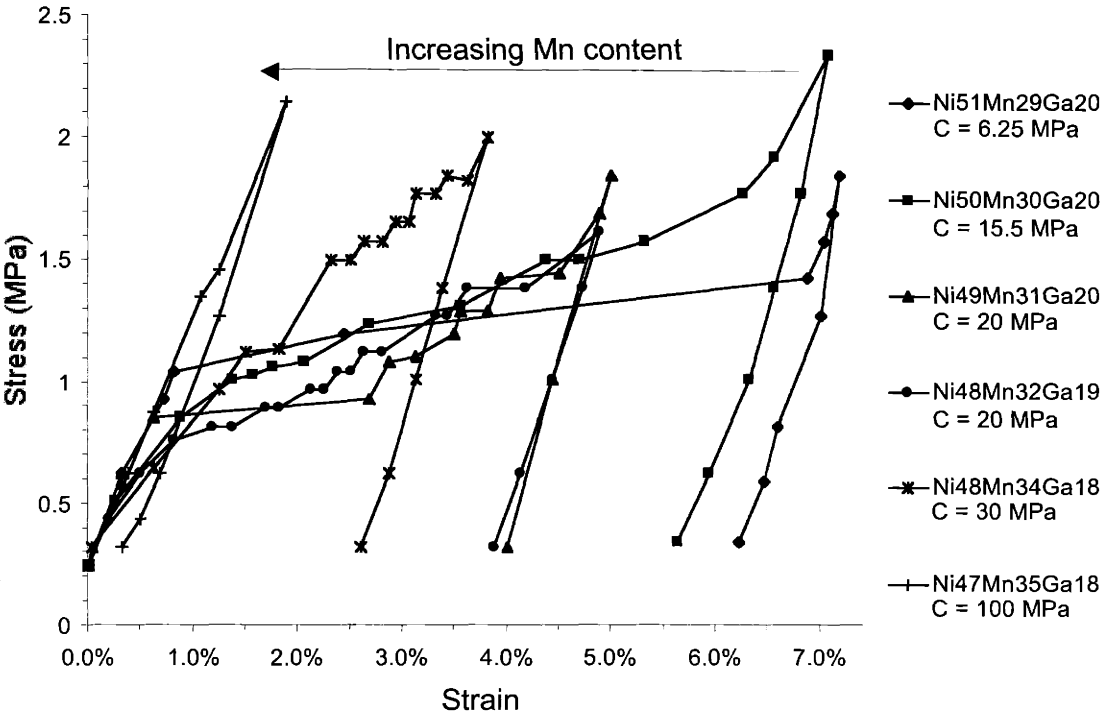

Figure 1.12: Stress vs. strain for single crystal samples of different Ni–Mn–Ga compositions (*from Murray and Henry* [47]).

1.2.7 Modeling

Thermodynamic equilibrium models by James and Wuttig[48], O'Handley[49], Likhachev and Ullakko[50], L'Vov *et al.*[51], and Murray *et al.*[2] have been proposed to describe MFIS in FSMAs. Soukhojak and Chiang [52] propose a kinetic relaxation towards equilibrium to explain static and dynamic hysteretic processes. Though they apply this model to electrostrictor materials, this approach is appealing in light of this attempt to categorize different dynamic FSMA behavior.

James and Wuttig's general micromagnetic model is based upon the minimization and compatibility of local Zeeman, magnetocrystalline anisotropy, magnetostatic, and mechanical energies. The formulation of this model is after James and Kinderlehrer [53] is particularly suited to numerical computation.

O'Handley's phenomenological model develops a free energy expression using Zeeman, anisotropy, elastic, and external stress energy to model the MFIS for a single crystal, bi-variant case. Though less generalized, this model is intuitive and accounts for magnetization remanence, nonlinear field dependence, and bias stress dependence of MFIS. O'Handley *et al.* discussed the phenomenology of this significant strain in [54].

Likhachev and Ullakko use experimental data to generate analytical solutions for MFIS and M versus H plots by differentiating Gibbs free energy expressions. These models account for magnetization, and strain in the presence of a field. With the exception of local stress accommodation in James' model, none of these models treat the development of the stress in the presence of a field. Chapter 5 presents an extension of O'Handley's model that qualitatively captures the stress as a function of the applied magnetic field and the bias stress.

Soukhojak and Chiang model non-equilibrium processes by allowing a relaxation process to occur to an equilibrium state according to a first order kinetic rate equation. They believe that quasi-static behavior can have static hysteresis due to potential barriers

between local free energy minima. Dynamic hysteresis is due to the time dependent relaxation towards the free energy equilibrium. In considering dynamic actuation response, one needs to consider a mixture of both static and dynamic hysteresis in analysis and modeling of active materials behavior.

This kinetic model takes electrostrictive constitutive relations and adds time dependent relaxation in the form of response times with an exponential dependence. Static hysteresis is added by the definition of a $tanh^3$ switching function that depends upon the applied stress and relaxes towards equilibrium values with a first order kinetic differential equation. Domain switching is relatively slow process, analogously like twin-boundary motion. Also included are the dielectric relaxation time constant and the elastic relaxation time constant. For example, the kinetic equation for the strain relaxation is:

$$\frac{d\varepsilon}{dt} = \frac{1}{\tau_{ela}}\left(\varepsilon_{equil} - \varepsilon\right) \qquad 1.3$$

where ε_{equil} is the equilibrium strain given by Hooke's law and τ_{ela} is the elastic time constant. A forcing electric field is applied to the material and each material property is allowed to relax at its own rate. The sum of these time constants adds a phase shift to each of the stress vs. strain, electric field versus polarization and strain vs. field plots, which contributes to dynamic hysteresis.

1.3 REVIEW OF STATIC ACTUATION BEHAVIOR

Murray [10] successfully carried out static measurements under a variety of different conditions for magnetization versus magnetic field, stress for strain, and strain versus magnetic field in Ni–Mn–Ga FSMAs. With these measurements Murray was able to establish a baseline for important values needed for further research of actuation properties and design of devices.

For example, Murray performed magnetization versus magnetic field measurements that physically constrain the sample and give properly defined thermodynamic low-field, fully-compressed, constant-strain susceptibility, χ_ε. In these tests, MFIS is not able to express itself and therefore stress builds up in the material. Though the stress would normally be able to move twin boundaries, the physical containment of the sample prevents such strains. Therefore, the only component of magnetization capable of expressing itself is due to the applied field. Because of crystal asymmetry along the *c*-axis, there are two values of the fully-compressed, constant-strain susceptibility in which the *c*-axis is parallel or perpendicular to the applied field. Murray reports these easy-axis and hard-axis permeability values as $(1+\chi_{\varepsilon,\|}) = \mu_{\varepsilon,\|} = 22$ and $(1+\chi_{\varepsilon,\perp}) = \mu_{\varepsilon,\perp} = 2.1$ respectively. These plots also give a measure of the magnetocrystalline anisotropy energy when the difference in stored magnetic energy is calculated between the easy- and hard-axes.

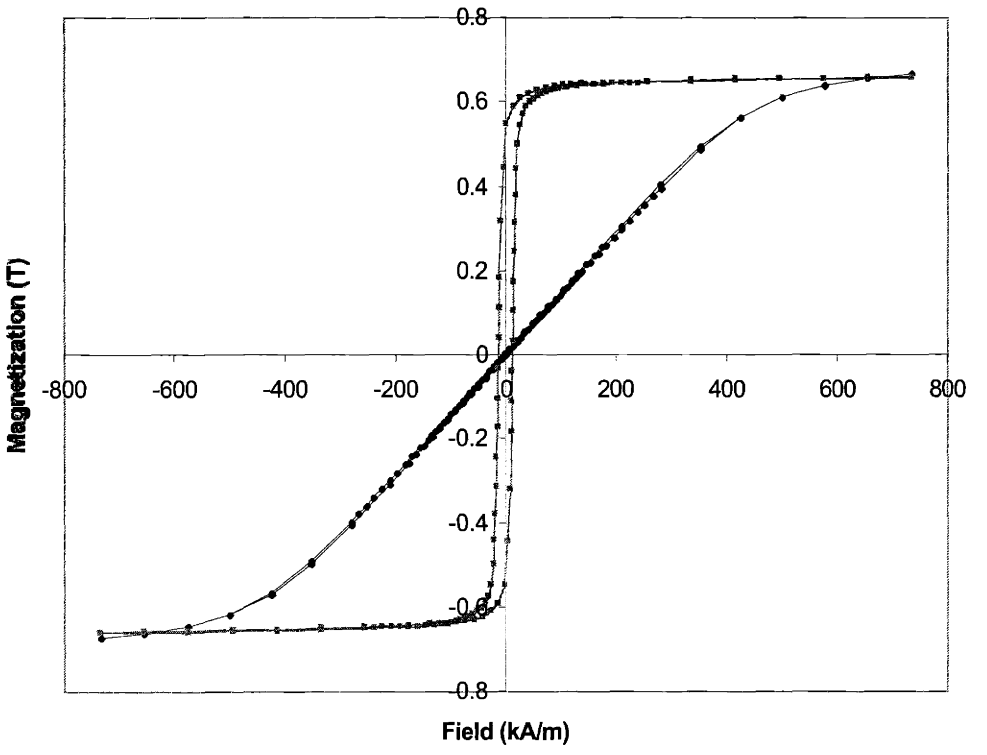

Figure 1.13: Constrained magnetization versus field loop for a cube of Ni–Mn–Ga in a single variant state resulting in an easy-axis relative permeability of 22 and a hard-axis relative permeability of 2.1. The magnetocrystalline anisotropy energy is calculated to be 0.16 MJ/m^3.

There are a couple of reasons why much useful property information can be gleaned from these two measurements. First, the sample was prepared with only a single variant, which ensured homogeneous magnetization throughout the sample. Second, the sample was mechanically forces to maintain a constant strain throughout the test. This prevented any variants from growing or moving and permitted the buildup of stress and the magnetocrystalline anisotropy energy in the material. Because of this preparation,

symmetry-differentiated permeabilities can be obtained without worrying about in abrupt change in magnetization during testing.

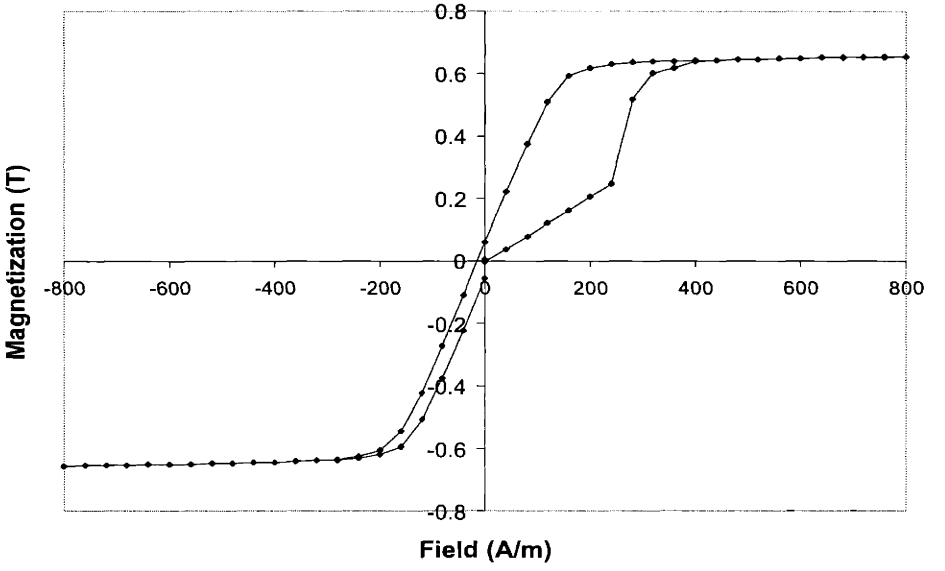

Figure 1.14: Unconstrained, magnetization versus field for a single crystal of Ni–Mn–Ga with one or more variants (uncorrected for demagnetization fields) (*from Murray*).

When precautions are not taken to ensure single variant orientation or mechanical constraint of the sample, there can be little certainty of the initial magnetization state. In this case, a twin-boundary may have introduced a 90° domain wall, creating an inhomogeneous initial magnetization state. Magnetocrystalline anisotropy and stress build up in the material until the yield stress of a twin-boundary is overcome and it propagates through the sample. Not only does this event cause an abrupt change in the magnetization, but also causes an abrupt change of the mechanical boundary conditions.

The decreasing, week-field susceptibility might be an acceptable thermodynamic property value if the specific stress or strain state of the sample could also be recorded. Thus, going through careful preparation of the sample, it becomes easier to document what the value of a thermodynamic property should be.

Further illustration of the importance of boundary conditions is in the quasi-static stress vs. strain plots of Figure 1.15. In these plots, an initially elongated sample ensured similar twinning strains between tests and a constant, homogeneous magnetic field was applied for the duration of the test. In this figure applied magnetic field has a dramatic effect on the twin-boundary yield stress, σ_{tby} increasing from 0.3 MPa to 2.2 MPa, as well as an effect on the twinning stiffness, c^H increasing from 7.5 MPa to 40 MPa. Once again, careful preparation of the initial state and the conditions under which the test is performed result in useful thermodynamic properties.

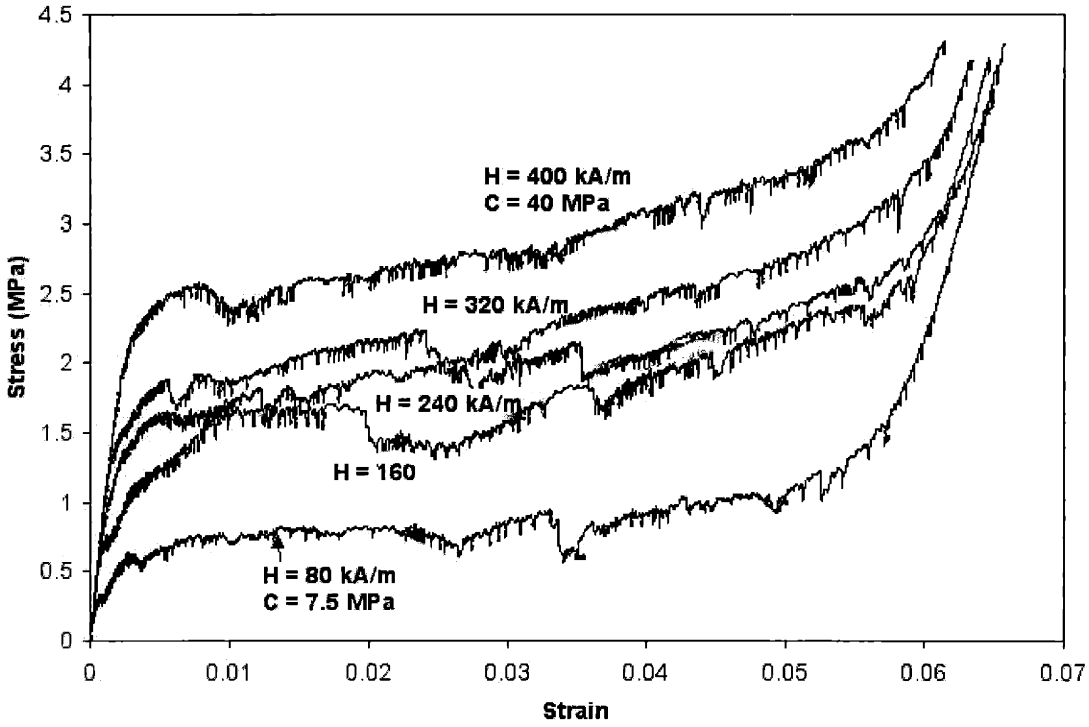

Figure 1.15: Quasi-static, uniaxial compression, stress vs. strain tests for a single crystal sample of Ni–Mn–Ga conducted at different constant magnetic fields. The twin-boundary yield stress increases from 0.3 MPa to 2.2 MPa and the twinning stiffness increases from 7.5 MPa to 40 MPa as the field between each test increases. (*from Henry* [55]).

The final example is from a family of strain versus magnetic field curves recorded at different constant stress values in Figure 1.16. In this sample, the increasing field strain follows a much different curve than the decreasing field strain on the same curve. At the lowest static stress, strain initiates at 320 KA/m (or 4 kOe) and increases abruptly to 6%. However, upon decrease of the field the strain does not decrease. At a constant stress of 1.62 MPa, strain initiates at a higher field, increases more gradually to only about 4.6%.

But the strain resets to its initial value. Upon application of the highest stress, 2.73 MPa, only 0.4% strain is not prevented, but only at the highest fields.

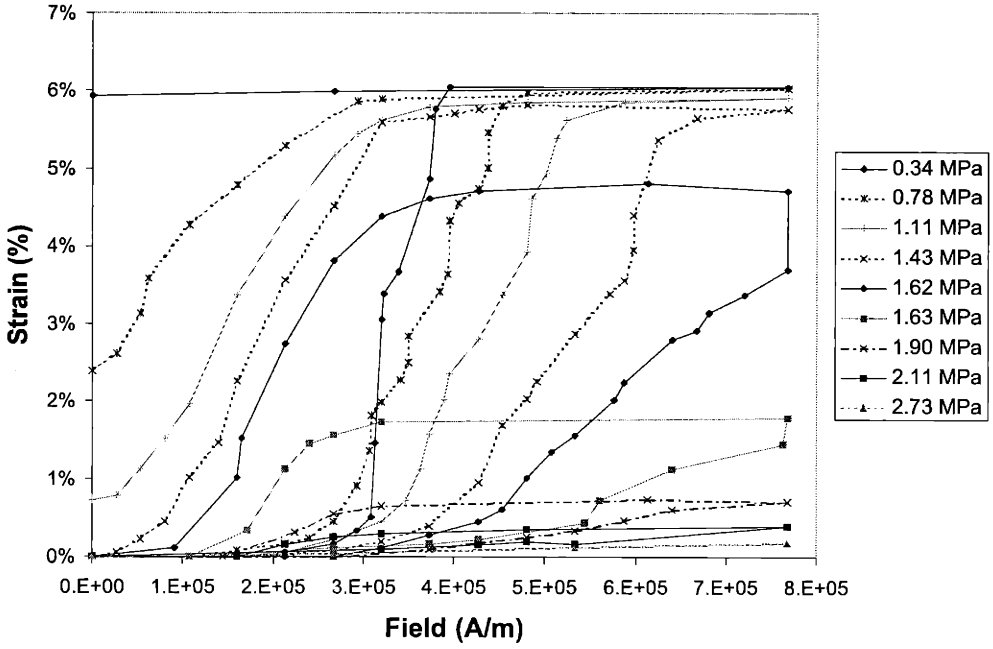

Figure 1.16: Quasi-static strain vs. field at different constant stresses for sample "C" in Murray [10].

The increasing field slope, $d_{31} = (d\varepsilon / dH)_\sigma$, of the family of curves in Figure 1.16 can be calculated at constant stress as the measurement was performed in that manner. A plot of these slopes versus stress in Figure 1.17 yields the proper static piezomagnetic constant of interest. This property completes those necessary to describe the linear, first-order magnetoelastic coupling in twinning Ni–Mn–Ga single crystals.

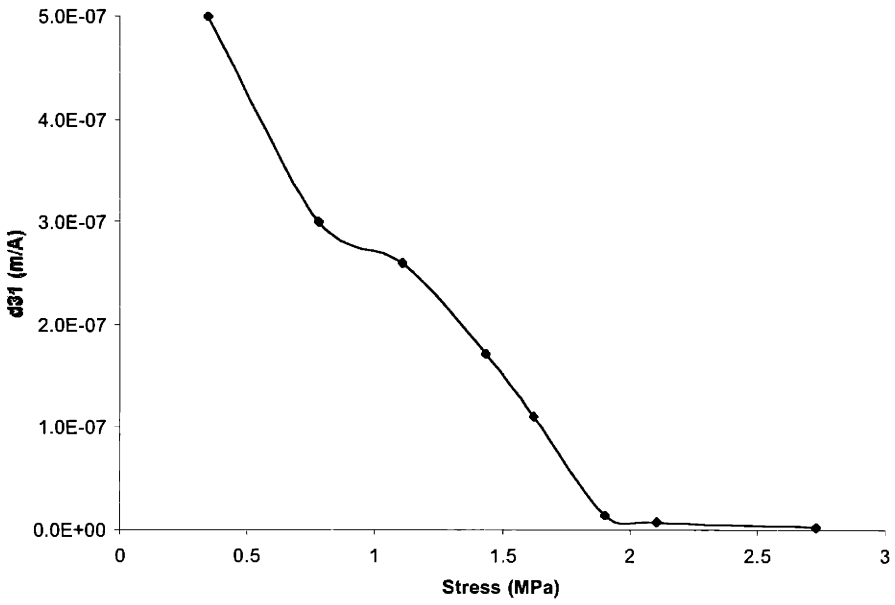

Figure 1.17: Maximum piezomagnetic coefficient versus different constant stresses calculated from the family of strain vs. field curves in Figure 1.16 (*after Murray*).

Murray made the first attempt to look at the strain response as a function of frequency in Figure 1.18. It is not clear if the rapid decline in strain with increased frequency is due to heating of the sample or electromagnet, inertia from a large static load, or if high inductive reactance prevented sufficient fields at higher frequencies.

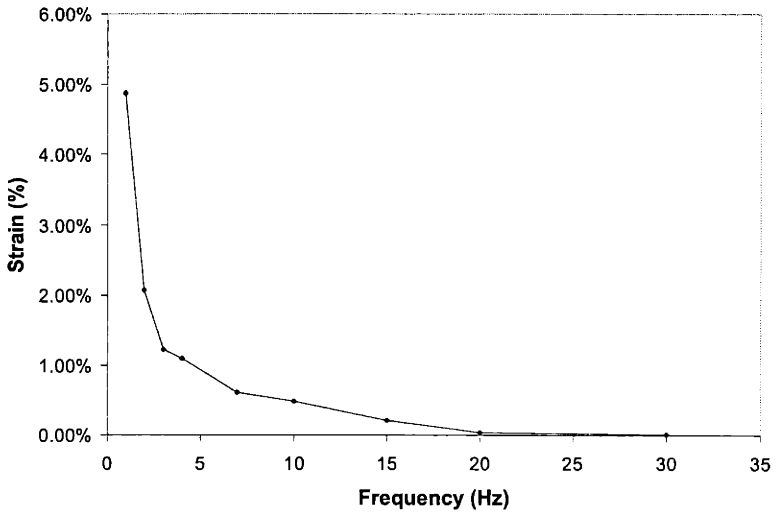

Figure 1.18: Maximum strain response versus frequency (*from Murray*).

Murray made the first quasi-static measurements of properties for Ni–Mn–Ga single crystals in the twinning regime. Because of the attention to the preparation of the samples and the experiments, these properties adhere (as practically possible) to the thermodynamic definitions derived in Appendix A. The static nature of these tests is great for obtaining values that may be compared by other researchers or utilized for preliminary device design. The practicality of operation in a device begs to characterize the properties under dynamic conditions.

1.4 DISTINCTIONS OF ACTIVE MATERIALS PROPERTIES

As illustrated in the previous section, measurement of meaningful properties can be an arduous task due to the initial conditions and maintenance of the appropriate conditions throughout a test. The task at hand is to characterize dynamic properties such

that they have utility not only from a practical standpoint, but also from a thermodynamic definition perspective. The constitutive equations derived in Appendix A, A.49 and A.50 (and below in 1.3 and 1.4), form the basis for an extension into describing dynamic properties. But there are major differences that need to be accounted for to make this extension. There are usually significant dissimilarities between the thermodynamics description and what is measured statically. Also, significant hysteresis is evident in stress vs. strain and strain vs. field that cannot be accounted for thermodynamically. Finally, there are substantial differences between dynamic measurements and static measurements. The purpose of this section is to explain how the paradigm of active materials reconciles these differences between thermodynamic descriptions and the measurement of dynamic properties.

The first law of thermodynamics provides a methodology with which to derive thermodynamic property definitions. An example of this methodology is carried out in Appendix A for a linear, first-order coupling of magnetic and mechanical variables. The resulting constitutive equations for the internal and Gibbs energy formulations are 1.3 and 1.4 respectively.

Internal

$$\begin{bmatrix} \sigma \\ \mathbf{H} \end{bmatrix} = \begin{bmatrix} \mathbf{c}^M & b \\ b^T & \left(\chi^{-1}\right)^{\varepsilon} \end{bmatrix} \begin{bmatrix} \varepsilon \\ \mathbf{M} \end{bmatrix} \tag{1.4}$$

Gibbs

$$\begin{bmatrix} \varepsilon \\ \mathbf{M} \end{bmatrix} = \begin{bmatrix} \mathbf{s}^H & -\mathbf{d} \\ -\mathbf{d}^T & \chi^{\sigma} \end{bmatrix} \begin{bmatrix} \sigma \\ \mathbf{H} \end{bmatrix}. \tag{1.5}$$

In the previous section, it is demonstrated that thermodynamic properties usually do not lend themselves easily to measurement because the initial state should be known as well as variables should be held constant. Furthermore, these thermodynamic properties are mathematically defined as a perturbation of an energy expression with respect to a variable from some equilibrium state. This implies a known equilibrium state from which property measurements are taken and the ability to keep the other variables constant.

Three further complications of static thermodynamic properties can be made to these simple thermodynamic definitions. These complications are: direction dependent properties, saturation behavior that is not describable with small perturbations. First, the inclusion of crystallographic symmetry adds direction-dependent properties as illustrated in appendix A in equation A.42. These multi-valued properties are represented as tensors, e.g. T_{ij}, where i is the direction index of the response and j is the direction index of the stimulus.

Examples of this are the easy-axis and hard-axis permeability values reported in the previous section by Murray. Active materials, exercise their anisotropic properties in order to exhibit their extreme behavior (such as huge strains). What is captured in a measurement differs: first, a material property could oscillate between two anisotropic limits (such as in a high loss material); second behavior seems to be an average of the

anisotropic limits (such a the modulus during twinning in FSMAs); and third, the resultant behavior of the anisotropic effects could accentuate each other resulting in a completely different behavior.

Second, the thermodynamic theory is usually good for properties at weak fields, but not good in describing saturation behavior. However, characterization of such extreme behavior in actuator materials is important for testing the limits of performance. "Minor loops" can be used to probe the material behavior around a biased state, even near saturation, and still adhere to the thermodynamic conditions. The problem with this approach to determine thermodynamic properties near saturation levels is because material behavior can be dependent on the path the free variables take to arrive at that level. (See glossary for "path-dependent properties.") However, in determination of energy loss and characterizing hysteretic behavior, the saturation characteristics are important.

Third, the thermodynamic energy expressions cannot account for the properties of non-equilibrium material configurations (such as domains or grains to lower the local free energy). One solution is to add a complex component to each property, thereby accounting for a phase lag of the material response and providing way to calculate the energy loss. Appendix B provides a background for this solution by deriving the relationships between the property, phase lag and hysteretic energy loss. It is important to

note that there can be static hysteresis as well as dynamic hysteresis. One aim of this academic work is to pursue a conceptual framework to categorize different sources of dynamic hysteresis.

1.5 Dynamic property classification

In actuation materials that are influenced by cyclic or dynamic stimuli, further clarification and classification of dynamic behavior is necessary if one still uses the thermodynamic methodology described above. Cyclic or dynamic properties are different from static properties in four ways. First, inherent modulation of the intensive stimuli makes it difficult to define an equilibrium response at a constant variable value; i.e. both magnetic field and stress vary during dynamic tests making it difficult to measure stiffness at constant field or susceptibility at constant stress. Second, if a material is reacting to an intensive stimulus, extensive variable response may be time dependent; i.e. micro-mechanism may energetically couple to provide or to rob the actuation behavior Third, the extensive response time may be a function of the frequency at which the cyclic test is being performed, such as in eddy currents and other meso-scale-mechanisms Fourth, over longer time scales, fatigue of the material response may occur in the material.

1.6 SCOPE OF THESIS

The research presented here focuses on partitioning the observed behavior to arrive at a clearer understanding of dynamic magnetic field induced strain actuation in single crystals of Ni Mn Ga FSMAs. A dynamic actuation testing apparatus was designed, built and used to carry out simultaneous measurement of four unconstrained variables. This system the enabled a complete picture of what is occurring during dynamic actuation. The goal of this research is to use this information to gain a richer and fuller understanding of the actuation mechanisms occurring in this material. To this end, a family of low frequency dynamic tests was conducted to probe the extent of possible variable behavior in this material. Figure 1.19 shows a data-rich three-dimensional representation of the extent of stress, strain and field behavior within this family of tests.

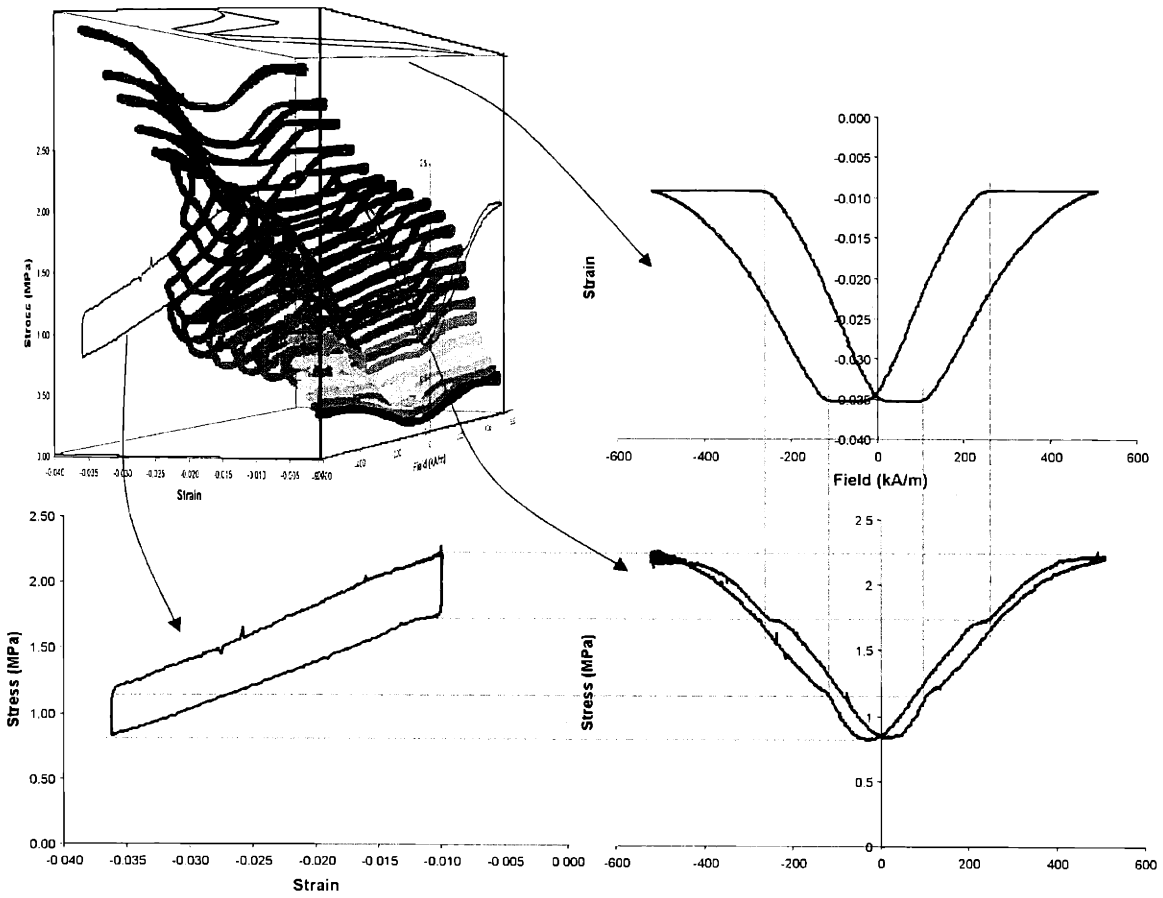

Figure 1.19: Upper left shows a 3-D representation of stress, strain and magnetic field behavior for a family of dynamic actuation tests occurring at 2 Hz. The 12th curve from the bottom is projected onto the σ vs. ε plane in the lower left, the ε vs. H plane in the upper right, and the σ vs. H in the lower right corner.

From this data, it is possible to artificially constrain variables of interest to calculate thermodynamic properties and to begin partitioning energy loss into the dynamic property categories presented in this chapter. For example, it is revealed that a magnetostriction-like process occurs as a likely mechanism for stress generation in an

increasing field. In Chapter 5, an expanded phenomenological model for FSMAs is introduced that approximates the observed stress behavior.

Chapter 2

2 EXPERIMENTAL SETUP AND SAMPLE PREPARATION

An experimental apparatus was built to explore 31-mode dynamic actuation of FSMAs. This chapter introduces the capabilities of the DATS and the procedures used to perform multivariable testing. Proper sample preparation for the DATS tests is important to prevent premature sample failure. Though both of the mechanical variables are uncontrolled (but measured), the mechanical boundary conditions remain important because they determine the maximum observed strain performance. Nevertheless, different sample geometries, compositions, and properties were able to exhibit reversible MFIS in the dynamic actuation test system (DATS).

2.1 DYNAMIC ACTUATION TEST SYSTEM

A schematic of the DATS is shown in Figure 2.1 and consists of two integrated parts: a structural frame to accommodate mechanical loading and an electromagnet to generate magnetic fields. The design of the structural frame is intended to provide flexibility in the measurement of MFIS in Ni–Mn–Ga alloys over relatively small loads and large displacements. The structural frame is used to support the mechanical loads generated during experiments and also to affix the electromagnet rigidly in place with respect to the frame. The X4 electromagnet used in this experiment can generate

saturating fields for Ni–Mn–Ga. It is the final result of design and fabrication efforts described in Appendix C.

The DATS utilizes four sensors that measure stress, strain, magnetic field, and dB/dt. A Hall probe measures the magnetic field generated and the magnetization is calculated in software from flux coil signals. Orthogonal to the applied field, the sample's displacement is measured as it strains against a spring and a load cell measures the resulting compressive forces. In the loading direction, lab-made load cell and strain sensing "modules" are attached at both sides of the frame. The micrometer is used to change the average force from test to test. Thus, the apparatus only measures the magnetic and mechanical variables in their respective single direction. This is the basic design of the DATS utilized for making dynamic actuation measurements.

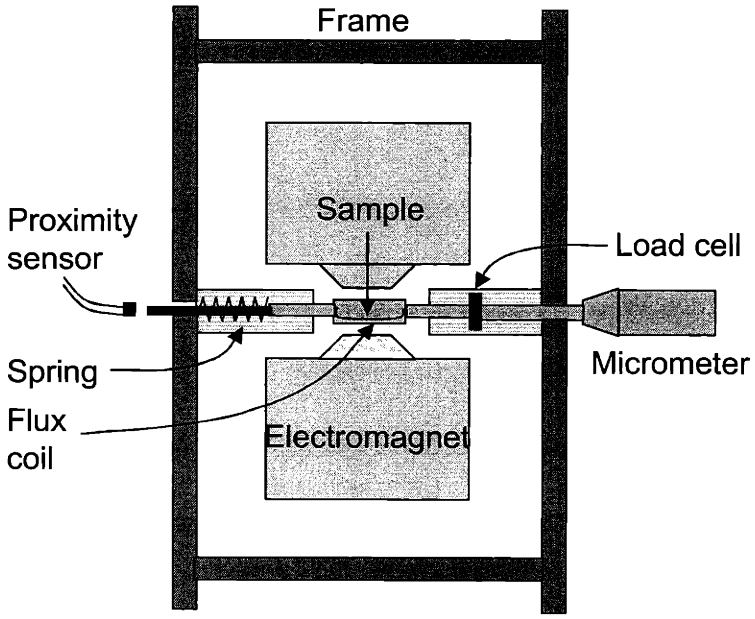

Figure 2.1: Schematic of the dynamic actuation test system. An electromagnet is attached inside a rigid frame. The magnetic field is measured by a Hall probe and the flux density is integrated from a flux coil signal. Orthogonal to the applied field, the sample's displacement is measured as it strains against a spring and a load cell measures the resulting compressive forces. The micrometer is used to change the average force from test to test.

A schematic of what occurs to the sample during a test in the DATS is in Figure 2.2. A sequence is shown how MFIS occurs when a sample works against a spring in an increasing magnetic field. The sample is divided into a simplified representation of two variant orientations: one parallel to the measured strain and one parallel to the applied magnetic field. Starting on the left, a compressed sample favors variant 2 (type 2 variant) and the suppression of variant 1 (type 1 variant, see glossary). The rectangle shows an exaggeration of the *c*- and *a*-axes in each variant and the arrows serve as a reminder of

the easy-axis directions. In the middle frame, variant 1 grows at the expense of variant 2 as the field increases. When the maximum field is obtained, the maximum dynamic MFIS and stress are measured. When the field decreases, this process reverses, completing one actuation cycle.

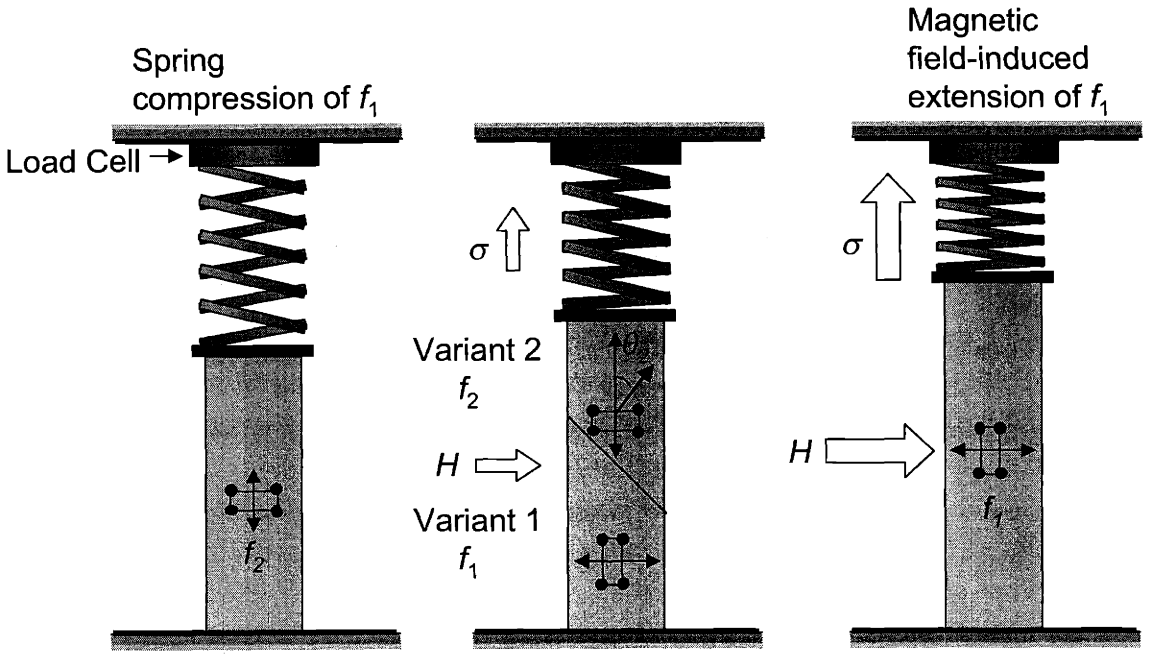

Figure 2.2: Schematic sequence of MFIS against a spring in an increasing magnetic-field from left to right. A compressed sample favors variant 2 and suppression of variant 1, but as the field increases variant 1 grows. When the maximum field is obtained, the measured stress is a maximum. As the field decreases, this process reverses, completing one actuation cycle.

A recent photograph of the DATS in Figure 2.3 shows several differences from the schematic in Figure 2.2. As seen on the outside of the structural frame in Figure 2.3, the DATS was designed to be modular such that it could be configured with an array of

different sensors and for a variety of different experimental conditions. Thus far it has made VSM-like magnetization vs. field measurements, uniaxial compression stress vs. strain measurements (Figure 1.12), static and dynamic 31-mode MFIS measurements. For dynamic actuation different modules are installed when different load cells, strain sensors, springs or samples are used in testing.

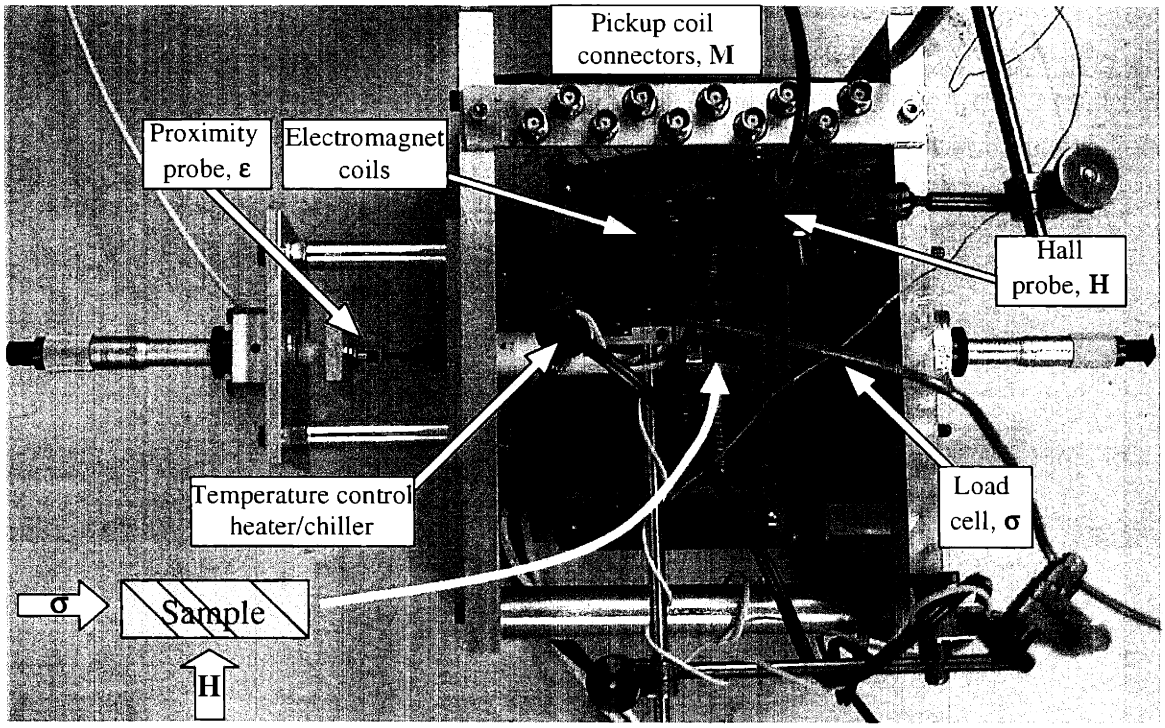

Figure 2.3: DATS X4. Second revision testing apparatus utilizing electromagnet X4 and outfitted for simultaneous measurement of magnetic field, flux density, strain, and stress. The temperature control capability was added only recently.

For the experimental results reported here, two different load cells were used: a 125 N compression/extension load cell and a 500 lb compression load cell. Position

sensors of two types were used: a lab-built capacitance sensor and an eddy current proximity sensor. Springs were used ranging from 2.9 kN/m to 36 kN/m. Different samples were tested that ranged in size from 0.4 cm to 2.5 cm long and as wide as 1 cm (electromagnet gap width). Sensitivities and accuracies of these sensors are tabulated below.

Table 2.1: Sensor sensitivities, accuracies and bandwidths.

Sensor	Sensitivity	Accuracy (% of FS)	Bandwidth
Capacitance sensor	62 μV / V *	0.01 %	100 Hz
Proximity sensor	0.25 mm / V	0.1 %	1 kHz
125 N load cell	11.1 N / V	0.01 %	50 Hz
500 lb. load cell	4.445 N / V	1 %	25 Hz
Gauss probe	1.000 kG / V	1 %	1kHz
Flux Coil	62 μV / V *	0.01 %	*

* Limited by digitization of signal.

The range of frequencies is dependent on the bandwidth of the sensors employed. The weak link in this regard is the stress measurement because the load cell's bandwidth only extends to 25 Hz. Each of the commercial sensors provides a signal-processing box that normalize the full scale signal to a 0 to 10 V output. The capacitance sensor utilizes a bandpass filter of the carrier frequency and the lock-in amplifier measures the voltage. The flux coils used range from 1 mm in diameter to the full perimeter of the sample. The coil voltages are amplified up to 1000× for 1 mm coils.

All voltage signals are digitized via a National Instruments 6052E data acquisition (DAQ) card that can handle 16, 16-bit input channels and 2,12-bit outputs at a total bandwidth of 333kHz or approximately 20 kHz per channel. Serial channel sampling of the signal required interchannel delay correction in post-processing. Digitization accuracy was not an issue as long as the signal was scaled to be a reasonable fraction of the DAQ card full scale (0 to ±10V unipolar or bipolar). However, cyclic averaging was sometimes utilized in post-processing to improve signal quality. Discrete sampling never caused aliasing issues because sampling frequencies were never less than 100× the Nyquist frequency (signal frequency /2), sampling frequencies were frequently 1000× to 2000× signal frequencies.

Measurement of MFIS in Ni–Mn–Ga alloys over different frequencies requires special considerations for the electromagnet and power supply, which are included in Appendix C. In early versions of the experiment, the X1 electromagnet used had a high inductance and high impedance and therefore was not well suited for higher-frequency testing. The AC magnetic field generated by the X1 revision electromagnet was accomplished with a 1 kW power amplifier with output impedance of 10 Ω. The X1 electromagnet bandwidth at 6 kOe was only 20 Hz, but increased bandwidth could be achieved using an L-C circuit with 1–10 μF capacitors at electronic resonance. This method boosted the maximum bandwidth for the X1 electromagnet at 6 kOe to about 70

Hz. The instability of the maximum magnetic field between 50 Hz and 70 Hz is due to different electric quality factors at the electronic resonant frequency. Higher frequencies were achieved with this electromagnet, but at reduced fields.

Subsequently, additional electromagnets were made and tested that exhibited better high frequency characteristics with an appropriate power supply. The AC magnetic field generated by the X4 electromagnet was accomplished using a 5 kW linear power amplifier with an output impedance of 1.75 Ω, with an inductance of approximately 2 mH/rad. (or 13 Ω/ Hz). Maximum bandwidth for the X4 electromagnet at 6 kOe was about 120 Hz and up to frequencies of 250 Hz for 3 kOe fields . Beyond the maximum bandwidth of either electromagnet, the field generated decays at –30 dB/decade. The electromagnet gap volume is $1.9 \times 1.9 \times 1.0$ cm and can accommodate samples up to 2.5 cm long with the electromagnet canted at 45° with respect to the mechanical load path. The frequency bandwidths of these electromagnets are limited mainly by the voltage and current specifications of the power supply.

There are several pieces of hardware that are swapped into the experimental apparatus depending on the particular geometry and size sample, including the spring, sample holders, and flux coil. Though the strain sensor and load cell need to be capable of measuring the full range of the dynamically changing variable, they need not be sample specific. A spring is chosen such that the spring is able to exert forces up to that

which blocks all dynamic actuation. The spring is inserted between a rigid standoff mount and a sample holder in the strain sensor module. Sample holders are made to closely, but not snugly, fit over the ends of the sample by approximately 0.75 mm (30 mils). The sample holders mount directly to the strain and load sensing parts of the module. A flux coil is made for each particular sample and is wound around the sample such that it would measure the flux density in the sample parallel to the applied field. Thus, a fair amount of hardware preparation is involved in order to start testing a FSMA sample. The following is the sample required to start making dynamic actuation measurements.

2.1 SAMPLE PREPARATION

Sample A is a thin slab of single crystal $Ni_{48.5}Mn_{29.5}Ga_{21}$ with dimensions $1 \times 5.6 \times 14$ *mm* that was cut such that each face is normal to $\langle 100 \rangle$ directions in the austenite. Below the martensite transformation, temperature of about 40°C, the sample forms macroscopic twins, i.e. larger that 0.25 mm and visible to the naked eye. The twins on the broad face are oriented at roughly 45° to the sample edges. This twin orientation is favorable for applied stresses or applied fields on either of the narrow faces. When only subjected to an applied field sufficient to magnetically saturate sample A, it shows 6% quasi-static MFIS. In order to maximize MFIS and minimize magnetic circuit reluctance, the sample is oriented in the electromagnet gap with the 6 mm dimension parallel to the

applied field, with the 14 mm dimension in the load path normal to the applied field direction.

In dynamic actuation testing, a spring with a known spring constant of 12 kN/m was used in series for sample A. With this, the equivalent modulus of the spring or the equivalent spring constant of the sample can be found with equation 2.1,

$$\frac{1}{2L}\sqrt{\frac{E}{\rho}} = \sqrt{\frac{k}{m}} \qquad 2.1$$

where L is the length, E is the uniaxial modulus, ρ is the density, k is the spring constant, and m the mass. From this, the effective spring constant is determined to be 4 kN/m from a measured system modulus of 40 MPa in dynamic stress vs. strain plots of this sample, so the effective stiffness of sample A is calculated to be 6 kN/m and the material modulus is 60 MPa. Nylon sample holders were machined with slits just greater than 1 mm wide and 0.75 mm deep and screwed into the strain and load modules. This sample was wrapped with a single turn (of 36 AWG insulated copper wire) flux coil about a 1×14 mm cross-section. This makes the normal of the coil loop parallel to the direction of the applied field.

Sample B is a $10 \times 10 \times 20$ mm Ni–Mn–Ga single crystal which was also cut with its surfaces normal to $\langle 100 \rangle$ directions in the austenite. Large, macroscopic twins are clearly visible below the martensite transformation temperature of about 40°C. The twins boundaries intersect the surface at roughly 45° to the sample edges and are observed on

opposing 10 × 20 mm faces. On the other two long faces and on the short ends, twin boundaries align with those that are at 45° on perpendicular faces. This twin orientation is favorable for axial compression along the 20 mm length with sample holders holding the small cross-section and applied fields on two of the long faces as shown in Figure 2.4. Sample B shows 4% quasi-static MFIS when not subjected to any loading. In dynamic actuation testing, a spring was used with a spring constant of 36kN/m for this sample. Two sample holders held 1 mm at each end of the sample and screwed into the strain and load modules. This sample was also wrapped with a single turn flux coil with a 10 × 20 mm cross-section.

In dynamic actuation testing of Sample B, a spring was used with a known spring constant of 36 kN/m for this sample. The effective stiffness of the system was calculated to be 18.2 kN/m from a measured modulus of 14 MPa. This corresponds to a sample stiffness of 36 kN/m and a material modulus of 28 MPa. Two sample holders held 1 mm at each end of the sample and screwed into the strain and load modules. This sample was also wrapped with a single turn flux coil with a 10 × 20 mm cross-section.

Before dynamic actuation testing occurs, these samples must exhibit static MFIS. The procedure to elicit MFIS from a virgin, [100] oriented single crystal is as follows.

1) Anneal single crystal at 900°C for 18 to 24hr.

In a study by Chu *et al.* [56] some benefits of post-annealing at stoichiometric compositions are revealed to be a increase of the transformation temperature for the structural phase transition of 25K from martensite to austenite and 4K from austenite to martensite; the ferromagnetic Curie temperature shifted down by 7K from its original value of (370K). This author is in agreement with the interpretation of the effect of the post-annealing treatment. It is believed that the annealing reduces dislocation density, compositional fluctuations, and second phase in the as-grown samples. The annealing treatment produces more homogeneous samples both in composition and in microstructure. Chu *et al.* suggest that a decrease of magnetic coercivity from ~250 Oe in the stoichiometric, as grown sample to 50 Oe in an annealed sample shows the elimination of a contamination phase that serves to pin domain walls and increase coercivity.

2) If twin variants are all aligned with the same orientation, then carefully testing for MFIS in an electromagnet can be attempted. Multiple variant orientations in a single crystal seem to greatly increase the likelihood of catastrophic fracture.
3) If no MFIS results, then careful mechanical training of the variants should be attempted to assist in promoting twin-boundary motion. This can be accomplished with a compression fixture.

4) If the above do not result in MFIS, then other properties, variant orientations, or other inhomogeneities at that composition prevent MFIS. Compositionally related problems cannot be solved readily.

5) However, different variant orientations can be coerced into a single orientation with reasonable success by heating above the martensitic transition temperature and cooling in a high magnetic field with one end of the sample against the cool electromagnet pole face.

6) Other ways of influencing variant orientation include applying compressive spring force during cooling.

2.2 Boundary conditions

Consideration of mechanical boundary conditions of the sample in the DATS helps clarify the discrepancy in maximum strain between the quasi-static and dynamic results. Twin boundaries that exit the sample surface create kinks, which are geometrically necessary to fulfill twinning compatibility criteria. The geometrically necessary kinks are prevented from forming on the loaded surfaces. In samples that exhibit readily movable parallel twin boundaries along its entire length and are subjected to mechanical clamping in the DATS, a prism-shaped region is developed at each end in which twin-boundary motion cannot occur. These "dead" areas of the sample do not exhibit twin-boundary motion and do not contribute MFIS during testing.

In sample A with a twin variant structure like that described in the previous section and actuated under 1.7 MPa, a prism shaped region at each end remains inactive. The affect this has on the overall actuation strain is determined primarily by the aspect ratio of the sample's width to length. In sample A the aspect ratio is 0.4, with active regions occupying the other 60% of the total volume and resulting in maximum possible strains of 3.6%.

In sample B the aspect ratio is 0.5, with the inactive prisms occupying 50% of the total volume as shown on the left side of Figure 2.4. The maximum DC strain in sample B (4%) should be reduced to 2%. Because the measured maximum dynamic strain is 2.6%, the mechanical constraint is not strictly adhered to. The "dead" regions due to this aspect ratio effect are well adhered to if the width to height ratio is large (>4) as it is in sample A.

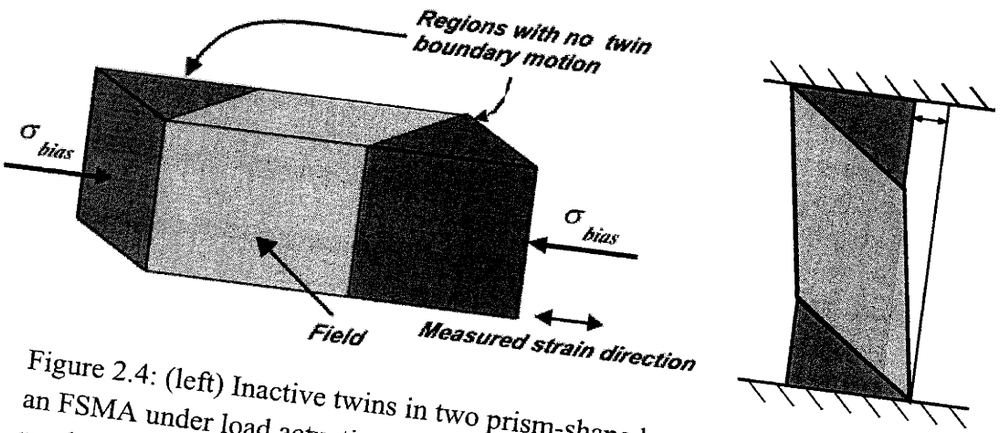

Figure 2.4: (left) Inactive twins in two prism-shaped regions at each end in an FSMA under load actuation. (right) Lateral motion of the sample due to mechanical constraints and the geometry of twinning in Ni–Mn–Ga.

Because of the mechanical constraints at either end of the sample and the kinks that form due to twinning geometry, one end of the sample becomes laterally displaced from the other as illustrated on the right hand side of Figure 2.4. This is important in consideration of the lateral stresses and strains placed on the measurement hardware. The sample holders deflect laterally on the order of 0.1 mm (1 mm * *tan*4°) in the worst case. This would be on the order of 10% of the greatest possible strain measurement. A feature of the DATS design is that lateral displacement is isolated from the longitudinal strain measurement by a long linear bearing that cannot transmit the lateral motion. Therefore, the measured strain is good measurement of the longitudinal strain in the sample.

2.3 VARIABLE CONVENTIONS

When the samples are placed into the hardware sample holders, the sample is initially elongated. As a bias load is applied, the sample is placed into a compressive state. Compressive stress causes a compressive strain, both of which are negative, while tensile stresses cause extensional strains. To do work active materials are usually placed under compressive loads for better reliability and longevity. It is also usual that in the large applied field state, the material elongates as to increase the compressive stress along the load path, or vice versa.

The reference state for strain will be the fully elongated state with the strain being negative as the sample is compressed in the longitudinal direction. For some strain data

presented here, the reference state of strain sensor was not maintained and therefore it is impossible to position the strain is any absolute sense. For these strain data only the relative displacement could be determined and they are plotted referenced to zero. The traditional sign convention would require the stress to also be negatively valued for compression.

2.4 AC MEASUREMENTS

High frequency dynamic actuation tests were conducted in a manner no different than tests conducted at low frequency. At low frequencies ($f < 50$ Hz) testing time was mainly limited by the heating of the electromagnet. As the test frequency increased, the inductive reactance increased, reducing the real power dissipated in the electromagnet. So the electromagnet actually runs cooler at high frequencies. The sample on the other hand, quickly showed a decreased strain response after a period of about one minute at 100 Hz. After this time, strain response would cease because the sample would heat and transform into austenite. Though the hysteretic mechanism causing heat production cannot be pinpointed, it is clear that a significant amount of heat builds up as the material cycles.

According to Bozorth [58], an energy loss of 1 kJ/m^3 per cycle in annealed iron resulted in a temperature rise of 0.0003°C per cycle. Given that the mechanical loss is 20 kJ/m^3 at maximum strain response (as shall be shown later), the single crystal sample of Ni–Mn–Ga heats 0.006°C per cycle. At 100 cycles per second, the sample heats

approximately 25°C to the transition temperature in 41 seconds. This corresponds well with the above observation. At 500 Hz, the sample heats 25°C in about 8 seconds, which also corresponds well to the time frame available for collecting data. In order to present strain actuation results at room temperature, only the first couple actuation cycles are used to report the strain vs. field behavior. Thus, frequency measurements imposed an additional limitation for collection of the data. This is also an important design consideration for a practical device that might be designed.

2.5 Experiment procedure summary

Experiment hardware dubbed DATS was designed, built and used to collect simultaneous multi-variable dynamic actuation measurements of single crystal Ni–Mn–Ga. Upgrades made from X1 revision to X4 included incorporating stress and flux coil measurements in addition to strain and field, modularity of the strain and stress sensors, improved bandwidth of the electromagnet and power supply, and temperature control. The DATS system also includes assembly and construction of the necessary electronics as well as computer control and processing of all signals.

Preparation of Ni–Mn–Ga single crystals required close attention because the variant structure and orientation are crucial for successful actuation. Two specific samples are used for results in this study: sample A has a composition of $Ni_{48.5}Mn_{29.5}Ga_{21}$ within ±0.5%, sample B, from Adaptamat, was much larger but with a

similar composition. Statically, sample A achieves 6% strain while sample B achieves 4%. These samples only realize a portion of this value because of the mechanical constraints imposed by loading.

Experimentally favorable thermodynamic properties are defined from a Gibbs free energy expression. Achievement of these property definitions, complete with variable constraints, is difficult in practice. Additionally, crystal symmetry places constraints on the possible properties and therefore physical mechanisms occurring within a material, and vice versa. Dynamic actuation response measurements are not optimal for measuring thermodynamic properties with the whole host of constraints. But these measurements are of great importance to transducer design engineers who make devices that operate under circumstances similar to test conditions.

Chapter 3

3 DYNAMIC ACTUATION MEASUREMENTS

Usually, active materials researchers report clamped ($\varepsilon = 0$) or unclamped ($\sigma = 0$) properties, short-circuit ($V = 0 \rightarrow \dot{B} = 0$) or open circuit properties ($I = 0 \rightarrow H = 0$) that correspond to thermodynamic definitions for electromechanical materials. Murray [10] collected magnetomechanical properties at constant stress for Ni–Mn–Ga FSMAs. The power of making simultaneous measurements of mechanical and magnetic variables allows a researcher to probe how the properties vary from condition to another. In this chapter, measurements of the free actuation behavior (see glossary) over the envelope of uncontrolled mechanical and magnetic variables actuation behavior allows for extraction of constrained thermodynamic behavior (see glossary) and the resulting thermodynamic properties not possible in an experiment. Partitioning the data in this way permits a distinction between behavior and properties occurring in the operation of a device and those reported as thermodynamic properties. Analysis of these partitions is the subject of the next chapter.

The three-dimensional representation of the multi-variable measurements in Figure 3.1 is a good way of visualizing the difference between the unconstrained path through variable space and a constrained path for proper thermodynamic consideration. Figure 3.1 shows a family of curves from sample A at an actuation frequency of 2 Hz.

Each color reflects a test at a different bias stress and shows how stress and strain vary as a function of the applied magnetic field. Each orthogonal slice shows how data can be extracted at a particular value of one variable to represent the locus of thermodynamically defined behavior of the other two ($\varepsilon(H)$ at constant σ, $\sigma(H)$ at constant ε, or $\sigma(\varepsilon)$ at constant H for example). Furthermore, comparison of the behavior and properties reveals the differences between practical operation and thermodynamics.

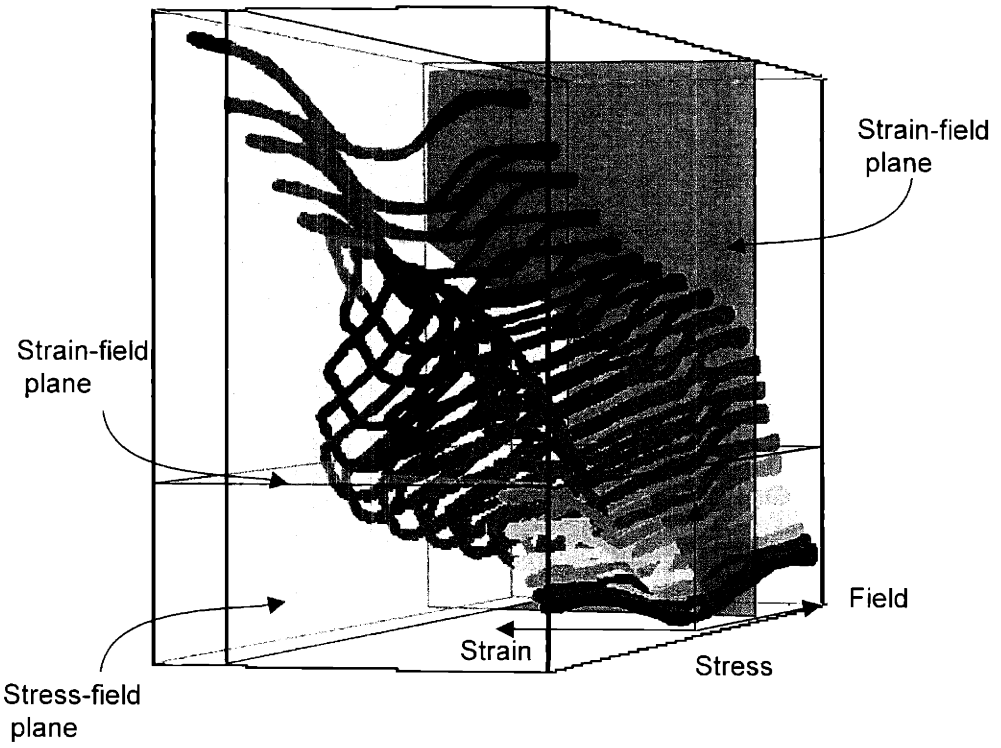

Figure 3.1: Three-dimensional stress, strain and field behavior for a family of curves from sample A actuated at 2 Hz. Compressive stress in the vertical axis increases from 0 to -4 MPa. Compressive strain in the horizontal axis varies from 0 to -3.6%. Applied magnetic field in the depth axis varies from —500 to +500 kA/m. The data lying on each slice represent the locus of thermodynamic behavior at a constant variable value.

The DATS was used to collect steady-state simultaneous measurements at 2 Hz of field, strain, stress, and magnetization on sample A. Many results are plotted together as a family of curves to more easily facilitate comparisons and to characterize trends within a family. Periodic slices taken from the 3-D variable space represent the spectrum of boundary conditions of thermodynamic behavior. The most effective way to step through the 3-D envelope is to watch an animation as the thermodynamic behavior proceeds from one variable extreme to the other.

A second set of experiments measures MFIS as a function of frequency at a constant bias stress of 1.7 MPa in sample B. The measurement frequencies span 2.5 decades, from 1 Hz to 500 Hz. Sample heating and electromagnet bandwidth limitations prevented testing at higher frequencies. Results of frequency-dependent magnetization-versus-field tests are compiled also in Appendix D.

3.1 Strain vs. field behavior

Figure 3.2 shows 2 Hz steady-state strain vs. field response for a range of applied compressive stresses after $N \approx 100{,}000$ cycles. These stresses increase from 0.2 MPa to 3.8 MPa with the left side labeled with bias stress values for which maximum MFIS increases with bias stress and with the right side labeled with larger bias stress values for which maximum MFIS is increasingly blocked. The strain vs. field data sets show full, symmetric strain-magnetic field loops for positive and negative fields as shown in Figure

3.2 as well as in Appendix D. They are rainbow color-coded in order of increasing bias stress, which will be used in other figures throughout this chapter. The strain axis is a measure of compressive strain such that 3.6% is the fully elongated state and zero strain is the fully compressed state. The curves are displaced along the strain axis to indicate the absolute displacement of the steady-state strain compared to the fully compressed or fully elongated condition.

At the smallest bias stress in Figure 3.2, 0.2 MPa, the field is capable of fully extending the sample. But the load (and displacement) generated in the spring can only compress field-actuated variants in the sample 0.1%. As the applied stress increases to 0.85 MPa, a greater proportion of field-actuated variants are compressed in response to the greater spring load, increasing the total actuation strain to 1.0%. Figure 3.5 shows that this trend continues up to bias stresses of 1.85 MPa, at which point the maximum reversible steady-state MFIS is 2.6%.

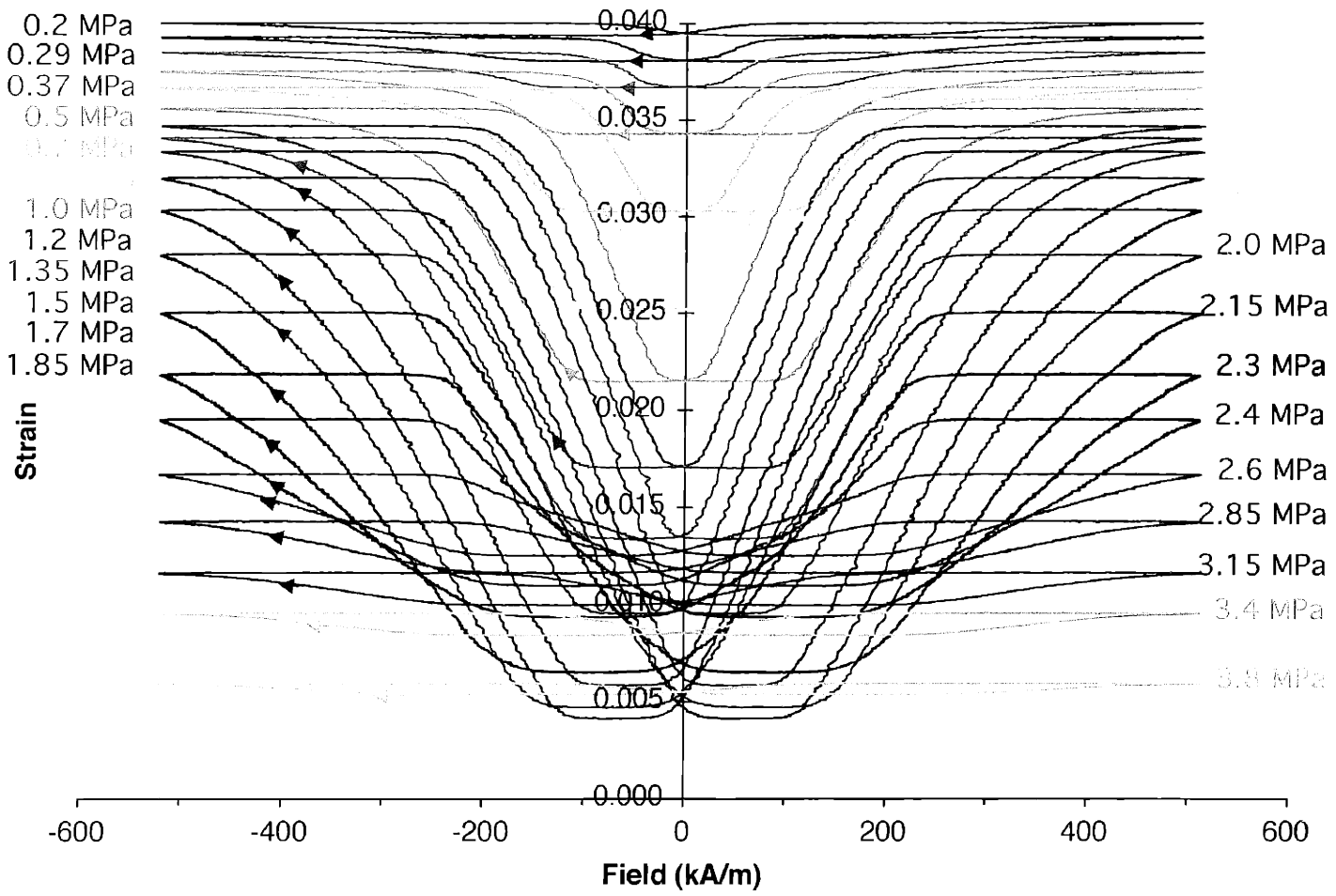

Figure 3.2: Sample A on revision X4, N~100,000 cycles. Steady-state strain versus magnetic field at 2 Hz response for the spectrum of applied stresses that give magnetic-field-induced strain.

At a bias stress of 2.0 MPa the maximum strain drops to 2.25% because larger spring loads start to prevent field-actuated variants from responding to the field. As one increases the bias stress from 2.0 to 2.6 MPa, the maximum field-extending strain continues to decrease. One expects that as the bias stress increases, the minimum spring-compressing strain would continue to decrease. However, within this 2.0 to 2.6 MPa stress range, the minimum strain increases, surprisingly. The sharp decrease in MFIS in this stress range means less dynamic spring compression occurs, thereby reducing the dynamic spring-load pushing back on the sample. This effect is illustrated on the spring-compression branch of the stress vs. strain plot in Figure 3.3.

Above 2.6 MPa, the steady-state strain continues to diminish monotonically as well as moving the position of the strain closer to full compression. The MFIS becomes increasingly blocked by the bias stress until the strain is limited to 0.1% at 3.8 MPa. Note that from zero to 4 MPa, the strain spans a total of 3.6%, the amount predicted in section 2.2 for this sample given the boundary conditions.

The maximum field-induced extension strain and the minimum spring compression strain for each of the curves in Figure 3.2 is shown versus bias stress in Figure 3.3. The upper curve (square symbols) is the maximum strain to which the field was capable of extending the sample. The bottom curve (diamond symbols) is the minimum strain to which the spring was capable of compressing the sample. The net

strain is also plotted and shows a maximum MFIS of 2.6% at 1.85 MPa mean bias stress. As mentioned above, it is evident in Figure 3.2 that the spring compression does not remain at 3.6% despite increased compressive load in the 2.0 to 2.6 MPa bias stress range. This is the result of a smaller volume fraction of variants producing MFIS reducing the stress on the spring and therefore the equilibrium position of the spring. The stress behavior will be discussed in greater detail in Chapters 4 and 5, but the decrease in dynamic stress can be observed in the 2.0 to 2.6 MPa stress range in Figure 4.7.

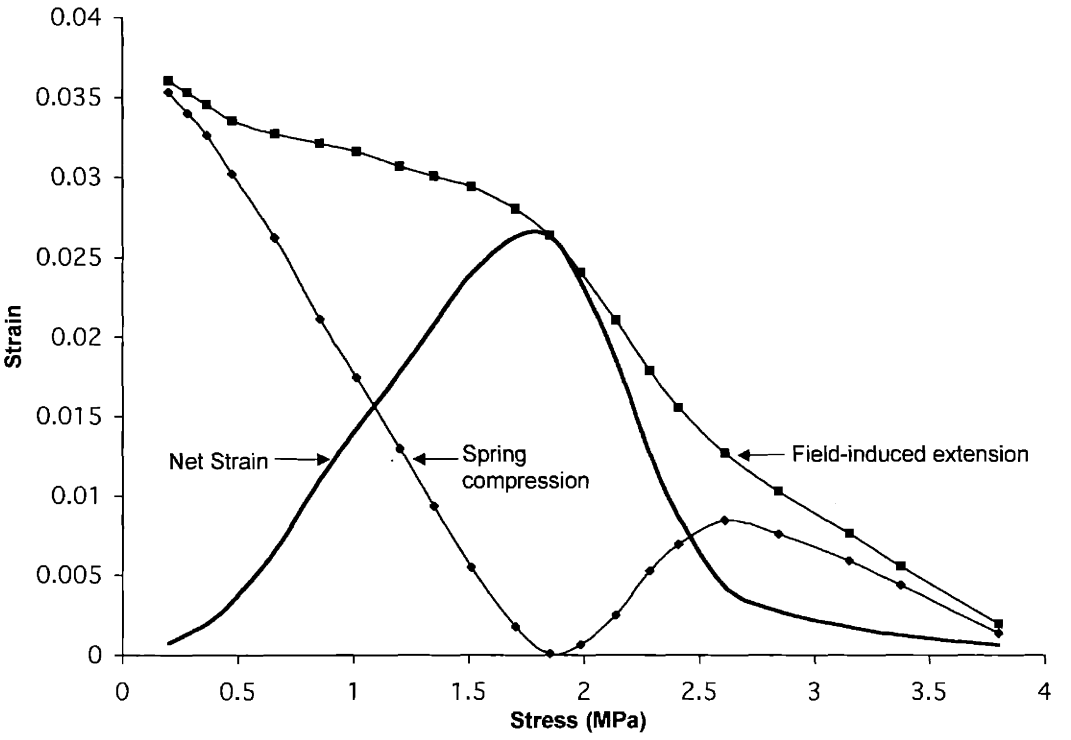

Figure 3.3: Square symbols represent the field-induced extension strain. Diamond symbols represent spring compression strain. The unmarked curve is the net strain between extension and compression. Both are plotted versus bias stress in MPa.

Figure 3.4 shows selected thermodynamic behavior for strain vs. field slices at constant stresses for the range of 0 to 4 MPa in Figure 3.1. Notice that each plot is comprised of different segments of several curves in Figure 3.2. The constant stress constraint alters the strain vs. field behavior in several ways. First, the threshold field needed to initiate twin-boundary motion is smaller than in Figure 3.2. Second, the coercive field, and therefore hysteresis, appears to be noticeably narrower than the coercive fields in Figure 3.2. Third, the maximum MFIS is larger for constant stress thermodynamic behavior as compared to similar stresses for the free behavior. Lastly, the constant-stress saturation strain is reached at much lower fields because the slope, $d_{31} = \partial\varepsilon_{11} / \partial H_3\big|_{\sigma}$, is greater than calculated directly from the experiment.

This last difference has to do with limitations of working against a changing spring stress as MFIS occurs. Although it is difficult to compare absolute strains between the free actuation behavior and the constant stress behavior, experience would indicate that strain actuation under a constant stress would result in a greater actuation than if the stress increases. Thus, the increase in stress within an actuation cycle acts as to block additional MFIS as the strain increases. The down side of working against a constant stress is that the inertia of the load dampens performance of the material, unless the material is excited at resonance.

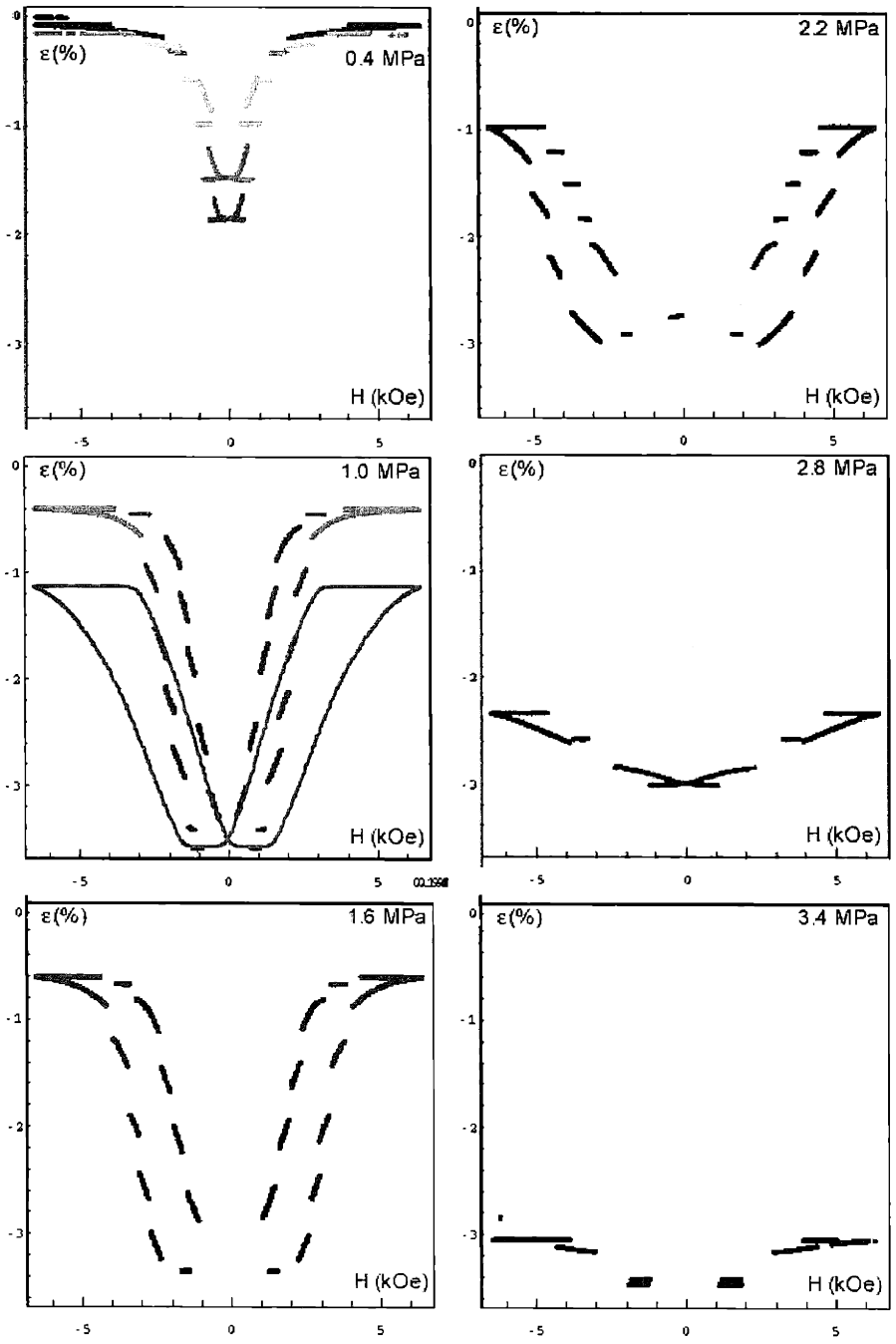

Figure 3.4: A selection of strain vs. field slices is shown at different constant stress values from the 3-D data from Figure 3.1. For the $\sigma = 1.0$ MPa slice, an unconstrained actuation curve is overlaid to illustrate the difference with constrained thermodynamically defined behavior.

Now, we turn to a property of magnetomechanical actuation: the piezomagnetic coefficient. As mentioned in appendix A, the crystal symmetry of Ni–Mn–Ga precludes the existence of a piezomagnetic coefficient. With the data presented by Murray earlier in Figure 1.16, one can calculate the strain per unit field with $d_{31} = \partial\varepsilon_{11} / \partial H_3\big|_{\sigma}$ as it is a common measure of active material response. This calculation is shown for Murray's data as short, dashed, blue lines in Figure 3.5.

The definition of the piezomagnetic coefficient is $d_{31} = \partial\varepsilon_{11} / \partial H_3$ when calculating the slopes of Figure 3.2 and Figure D.1. These values of d_{31} are determined under changing stress conditions and are therefore not thermodynamic properties. The long, dashed, red lines in Figure 3.5 show the d_{31} coefficient versus compressive bias stress at $N \approx 1{,}000$ measured at the steepest parts on the increasing and decreasing field segments of each strain vs. field curves in Figure D.1. The solid, green lines show the d_{31} coefficient versus compressive bias stress at $N \approx 100{,}000$ measured at the steepest parts on the increasing and decreasing field segments of each strain vs. field curves in Figure 3.2. For the same sample, the d_{31} coefficient is approximately two times higher for $N \approx 1{,}000$ than corresponding values at $N \approx 100{,}000$. This is evidence of how the piezomagnetic coefficient diminishes as the materials subjected to additional actuation cycles.

The diamond symbols in Figure 3.5 show the thermodynamic $d_{31}|_{\sigma}$ from the $N \approx 100{,}000$ data set in Figure 3.2. The heavy lines over the diamond symbols show a linear fit over two ranges of stresses. Thus, when accounting for the difference in the field necessary to generate the same strain is lower than in Figure 3.2.

It is believed that the difference between increasing and decreasing field d_{31} values is the result of different mechanisms that generate stress to extension versus those required for compression. In all of the calculations of the dynamic piezomagnetic coefficient, one can see values close to bias stresses of 1.0 MPa represent the greatest efficiency for converting field into strain.

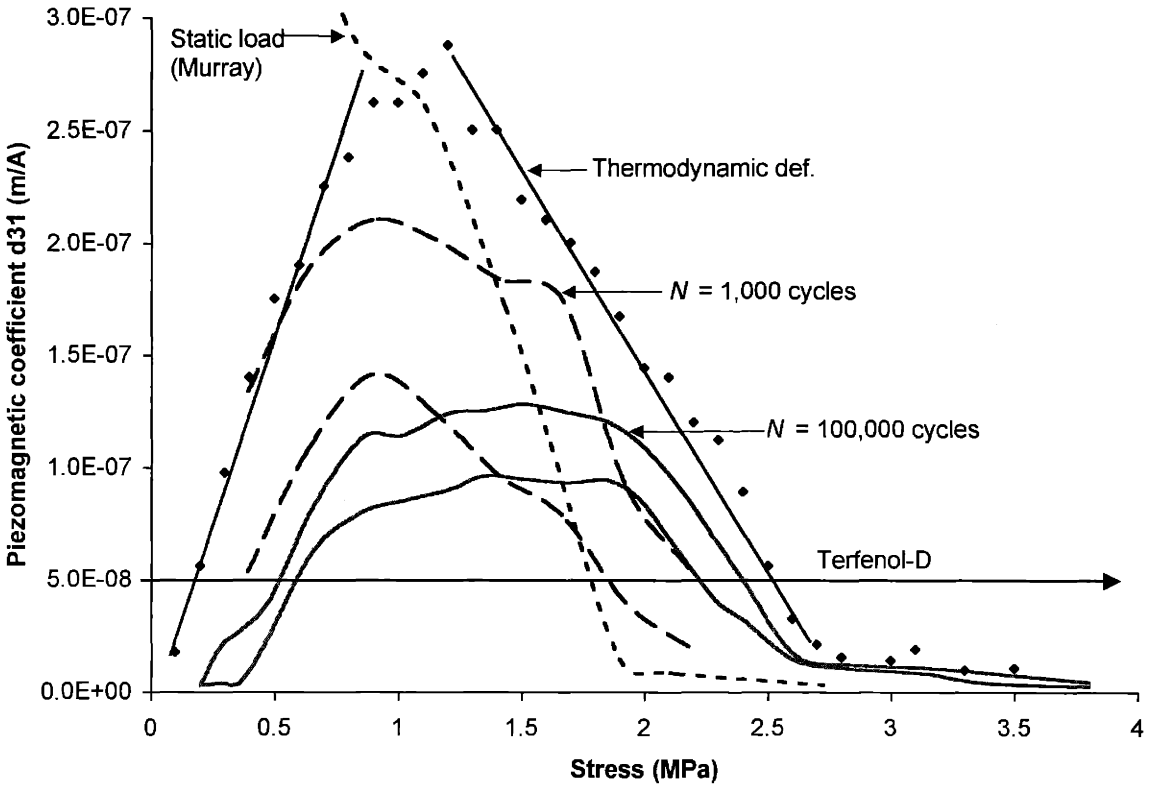

Figure 3.5: Maximum d_{31} coefficient versus compressive bias stress under different conditions: (short dashed lines) quasi-static actuation under a dead load by Murray [10] (long dashed lines) $N \approx 1000$ cycles, lower curve is measured in an increasing field and upper curve is in decreasing fields; (thin lines) $N \approx 100{,}000$ cycles, respective magnitudes are down for the lower and upper curves for same sample. (diamond symbols) proper thermodynamic d_{31} from the $N \approx 100{,}000$ curve. (heavy lines) linear fit to thermodynamic piezomagnetic coefficient.

A maximum value for free actuation behavior is about d_{31} of 2.5×10^{-7} m/A at 1.0 MPa in a decreasing field, which is approximately five times that of Terfenol-D [57]. With an FSMA piezomagnetic coefficient approximately five times that of Terfenol-D, Ni–Mn–Ga at 1.2 x 10^6 MPa also converts magnetic energy at an efficiency 5 times greater than that of Terfenol-D at 1.2 x 10^6 MPa. Using a value of

$d_{31} = 2.8 \times 10^{-7}\,\mathrm{m/A}$ for Ni–Mn–Ga and $d_{33} = 5 \times 10^{-8}\,\mathrm{m/A}$ for Terfenol-D, magnetic energy density per unit field, $\Delta E / \Delta H = d \times \sigma$, is 37.5 × 10^{-2} (J/m^3)/(A/m) for Ni–Mn–Ga versus 7.5 × 10^{-2} for Terfenol-D.

3.2 STRESS VS. FIELD BEHAVIOR

Figure 3.6 shows steady-state stress and strain response versus applied magnetic field from a particular test labeled 1.5 MPa. The dashed lines between the strain and stress plots show the correspondence of the initiation of twin-boundary strain at a threshold field and the start of the "plateau" on the stress curve. Why a plateau appears rather than just a discontinuity in the slope is unclear, however it visibly shows the connection with strain initiation. Correspondence of strain initiation to the stress plateau is evident in most of the stress vs. field curves in Figure 3.7.

Figure 3.11 shows 2 Hz, steady-state, compressive stress in the load path versus magnetic field for a range of applied bias stresses. In similar fashion to that of the strain vs. field plot, bias stresses are labeled from 0.2 MPa to 3.8 MPa. Full, symmetric loops for positive and negative fields were recorded, but for clarity only half of each loop is shown on alternating sides. The stress axis is a measure of compressive stress such that zero stress is the fully elongated state. The displacement of each curve along the stress axis indicates the absolute compressive stress within sample A.

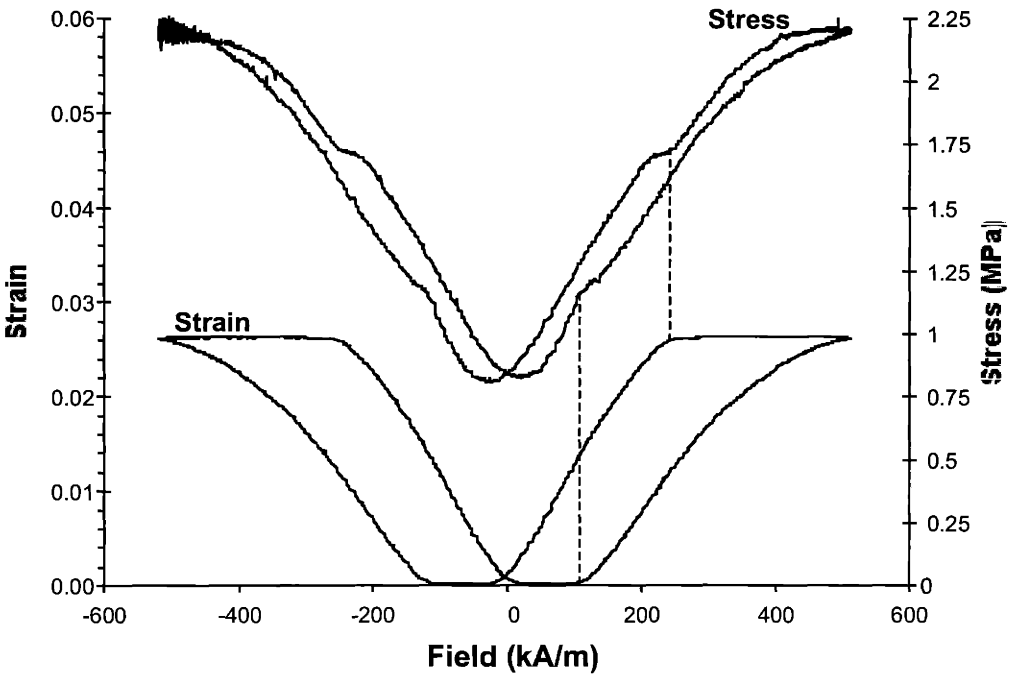

Figure 3.6: Strain and stress versus magnetic field for sample A at bias stress of 1.5 MPa.

Four different behaviors are observed in Figure 3.11 as sample A is compressively stressed in cyclic field at 2 Hz. In all of these regimes, the plateaus coincide with the initiation of the twin-boundary motion. First, from 0.2 MPa to 0.5 MPa the stress increases in a parabolic fashion to a saturation value in fields of under 175 kA/m. This threshold field tends to decrease as the bias stress increases within this range. When the field reverses, there is a small stress rise on the order of 50kPa. The stress gradually decreases as the field is removed. At these low average applied stresses the stress on the increasing-field part of the cycle is greater than that on the decreasing part.

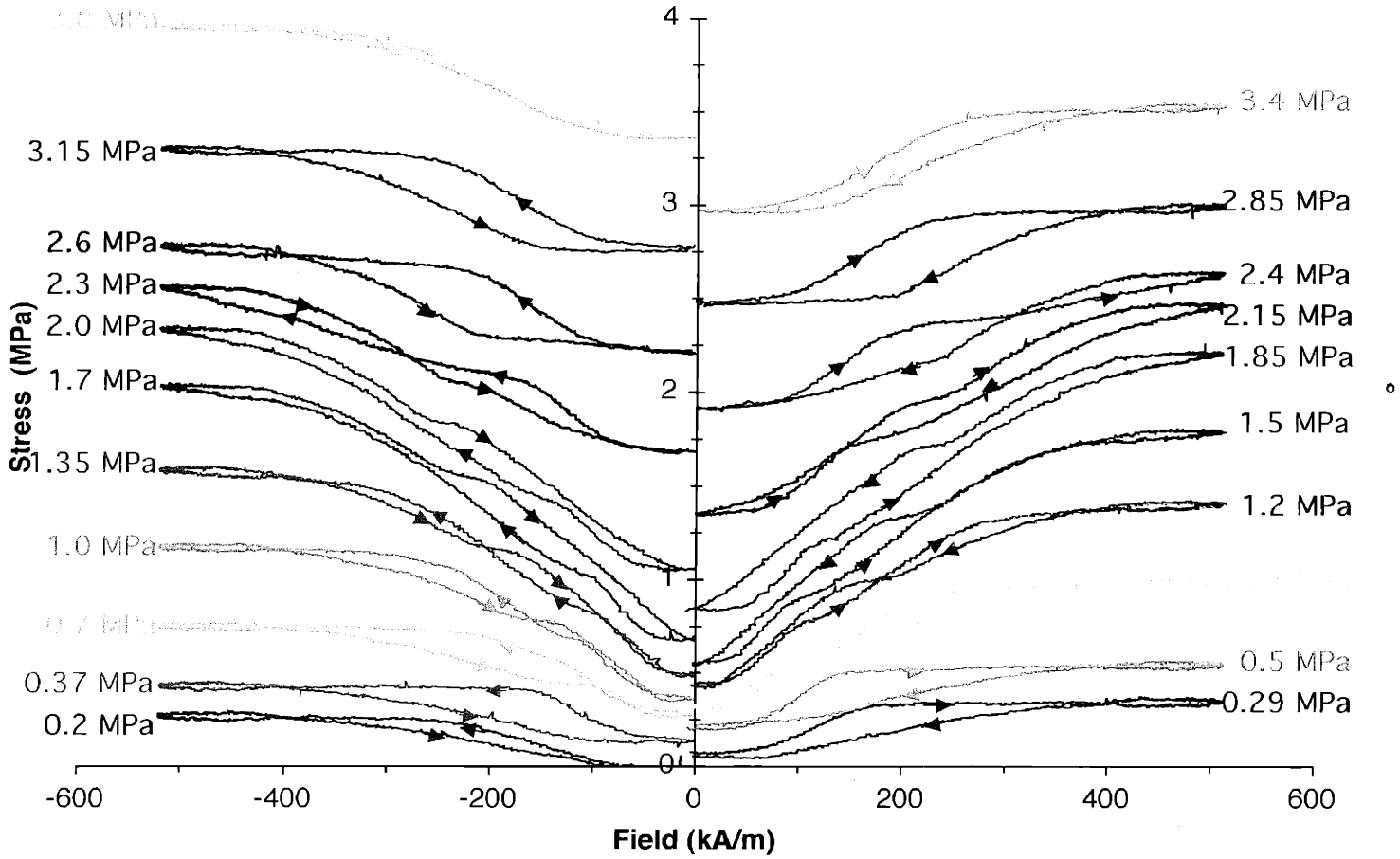

Figure 3.7:Family of steady-state stress vs. field curves at 2 Hz response. The mean bias stress is labeled to coorelate it to the strain vs. field curves. Shading is to help distinguish different curves while the arrows indicate the direction of the loop.

In the second regime between 0.7 and 1.5 MPa, the stress behavior changes in three ways. First, the field at which twin-boundary motion starts to occur in Figure 3.8 is also the field at which the stress shows a plateau at an intermediate stress before continuing to increase. The plateau field remains relatively constant at about ±100 kA/m regardless of average bias stress. Second, the field at which the stress saturates increases from about 250 kA/m at 0.7 MPa to about 400 kA/m at 1.5 MPa. Third, an intermediate stress plateau on decreasing field indicates the field at which twin compression is initiated. The decreasing field, at which this plateau occurs, increases from 150 kA/m to about 200 kA/m. These plateaus cause a crossover such that the stress needed to expand the sample is less than the stress required for sample contraction.

The third regime of bias stresses between 1.7 MPa and 2.15 MPa shows that the increasing stress branch of the curve never crosses the decreasing stress branch as the field cycles from zero to 520 kA/m and back down. Here the path around the stress vs. field loop is in the opposite sense of that in the first (low average stress) regime. The stress increment up to the plateau with increasing field and the stress increment down to the plateau with decreasing field remains constant within this bias stress range. Furthermore, the stress only saturates when the field is at a maximum.

In the fourth bias stress regime from 2.3 MPa to 3.8 MPa, the sense of the stress vs. field loop is the same as that at the first (lowest average stress) regime. At 3.8 MPa

bias stress, the field hysteresis nearly vanishes. This bias stress dependency of the plateaus (at which twin-boundary motion is initiated) is shown later in Figure 4.7. The discussion in the next chapter will indicate how a stress can develop through magnetization rotation in the material without twin-boundary motion.

3.3 Stress vs. strain behavior

The 2 Hz family of stress vs. strain curves in Figure 3.8 is from the same steady-state free actuation behavior under 2 Hz magnetic field-induced actuation as in Figure 3.1. The strain axis is a measure of compressive strain such that zero strain is the fully elongated state.

Each of the stress vs. strain loops can be thought of as a pair of static stress vs. strain plots with the second one inverted during sample recompression, like those in Figure 1.15. Above the twin-boundary yield stress, twin-boundary motion causes strain along the relatively flat portion of the curve. At maximum field, the sample achieves an equilibrium volume fraction of variants oriented with the field. In order for this stable state to be unbalanced as the field decreases, the twin-boundary yield stress must again be exceeded to initiate compressive strain. The balance between the competing stress in the sample and the applied magnetic field determines relative strain the equilibrium state at maximum twinning in the static stress vs. strain.

During steady-state cyclic actuation under the smallest applied mean bias stress, 0.2 MPa, the sample remains almost completely extended near zero strain. But the stress generated by the spring is not sufficient to fully reset the sample by reorienting the field-elongated variants, resulting in a total strain of only 0.1%. As the compressive bias stress increases, the maximum cyclic MFIS grows non-linearly as the magnetic-field-induced stress approaches the compressive spring stress. For average bias stresses above about 1.5 MPa, the cyclic strain reaches a maximum strain of 2.6% and approaches the maximum compressive displacement for this sample at a strain of 3.6%. Above 1.5 MPa, the bias stress starts to prevent field-favored variants from responding to the field. For the stress vs. strain loop at 3.8 MPa, field-induced strain is almost completely blocked due to the high stress counteracting twin-boundary motion.

Figure 3.9 shows a selection of thermodynamic stress vs. strain plots obtained by sectioning the stress-strain-field envelope of Figure 3.1 at constant field. At both extreme high and low stresses, elastic behavior is evident. At intermediate stresses twinning is prevalent as evidenced by a lower stiffness and hysteretic loss. Only in this intermediate stress range, where the magnetomechanical coupling is large, is hysteretic energy loss evident. The meaning of the negative slope in highly coupled region of the stress vs. strain behavior is possibly due to magnetomechanical coupling of strain energy being given back and dissipated. In the stress range of 2.0 to 2.6 MPa, the material cannot

accept any more strain energy and so it must give it back to the system as heat, coupling, and/ or magnetic loss. Though the shapes of the hysteretic portions of Figure 3.8 and Figure 3.9 look substantially different, the mechanical energy losses calculate in each case has the same magnitude, 20 kJ/m^3.

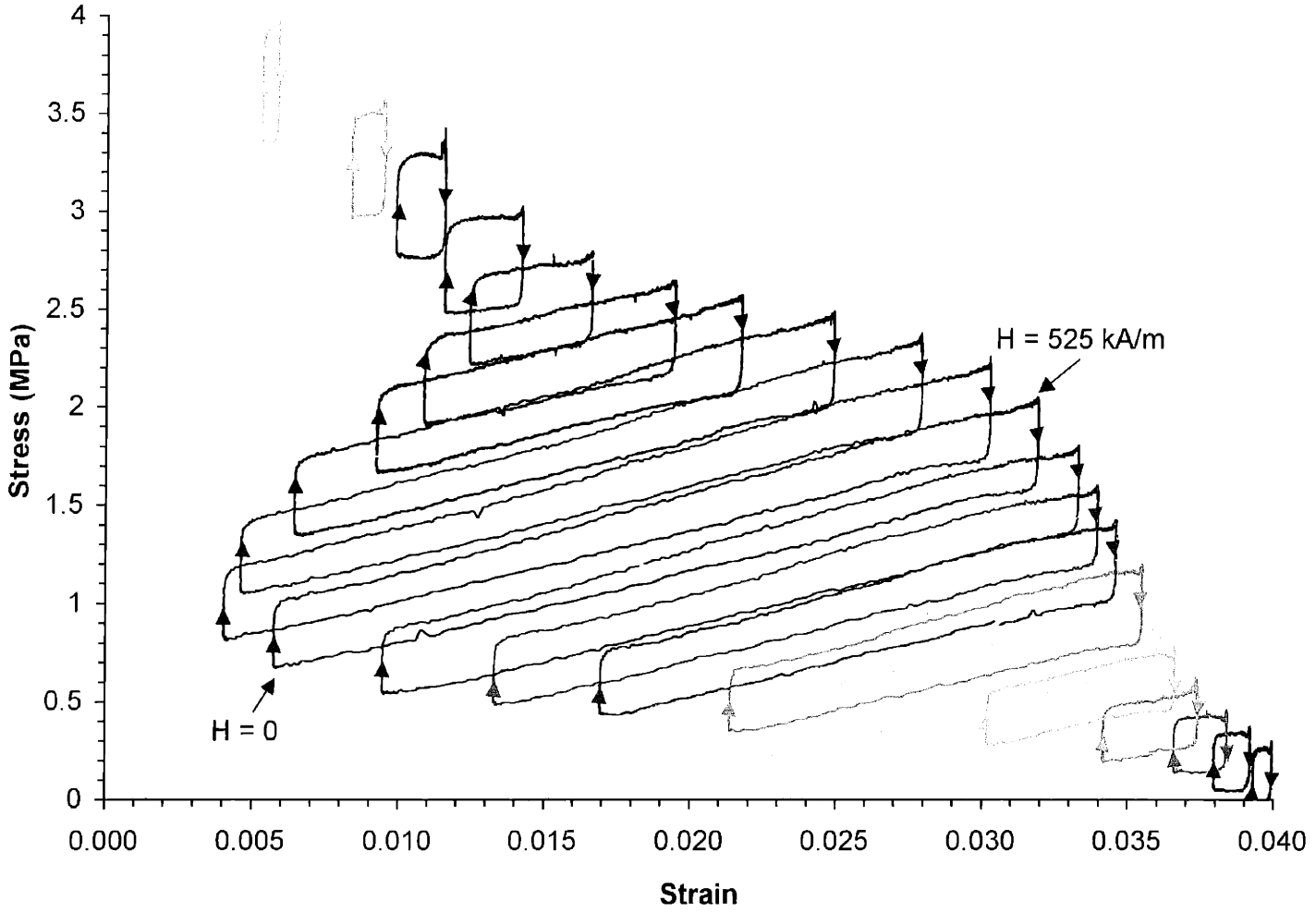

Figure 3.8: Family of steady-state stress vs. strain loops at 2 Hz with increasing bias stresses from the lower right to the upper left. The stress difference (or coercive stress) between increasing and decreasing strains is a major source of loss for MFIS tests.

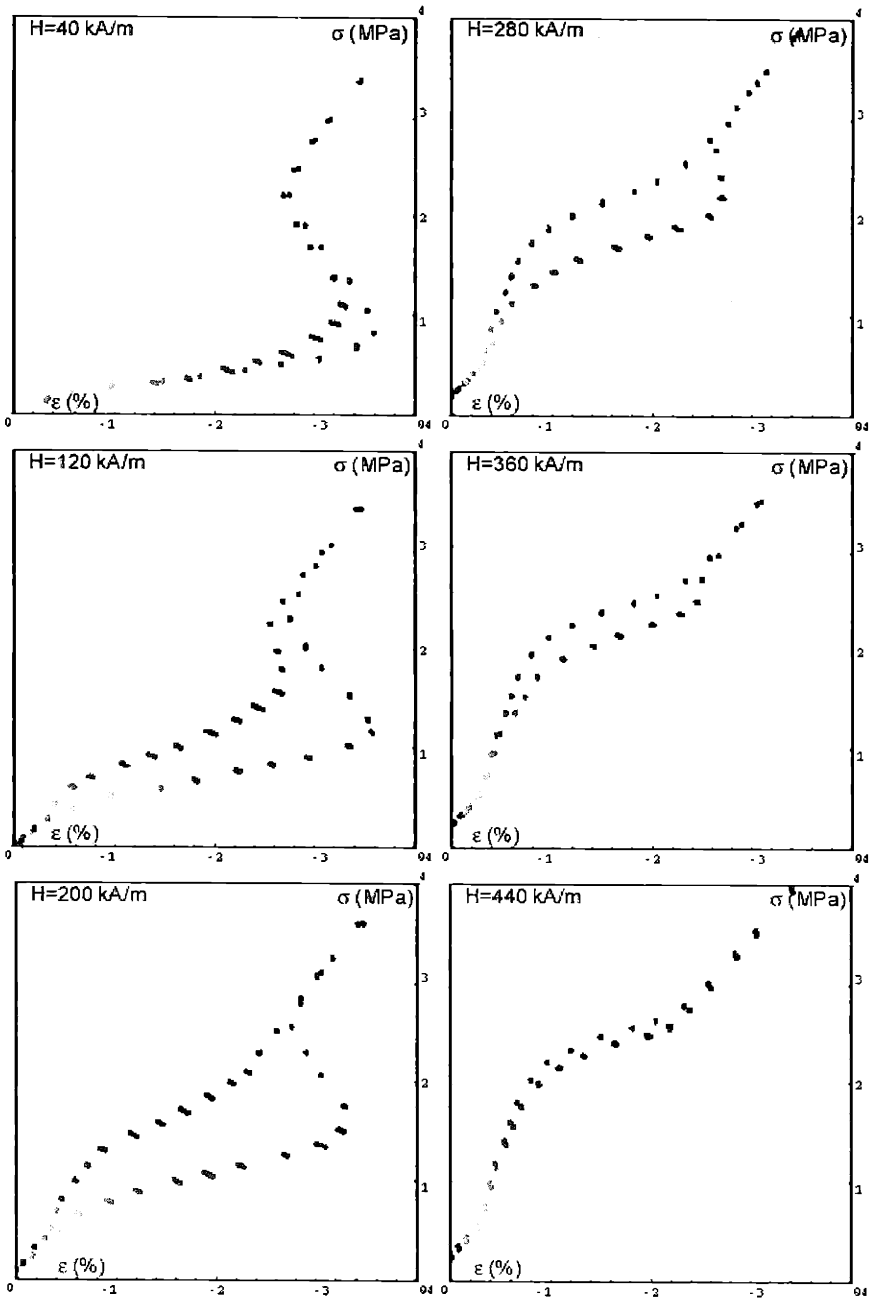

Figure 3.9: A selection of thermodynamic stress vs. strain behavior from the 3-D data shown in Figure 3.1 at different constant magnetic fields. At low and high stresses and strains, elastic behavior is shown. At intermediate stresses twinning is prevalent evidenced by a lower stiffness and hysteretic loss.

The stiffness of the 2 Hz cyclic stress vs. strain loops at different bias stresses is shown in Figure 3.10. Initially, the stiffness is higher at lower bias stresses because the twin-boundary yield stress has not been overcome. But MFIS due to twin-boundary motion, in the presence of a magnetic field occurs at bias stresses between 0.3 MPa and 2.7 MPa. In this stress range, stiffnesses approach 40 MPa. The constant-field twinning stiffness is relatively constant between 30 and 35 MPa in Figure 3.9. When the bias stress is sufficiently high, twin-boundary motion is prevented from occurring and the stiffness approaches the compressive Young's modulus. Likewise at high stresses and also at low stresses, the apparent elastic stiffness remains relatively constant between 120 and 130 MPa.

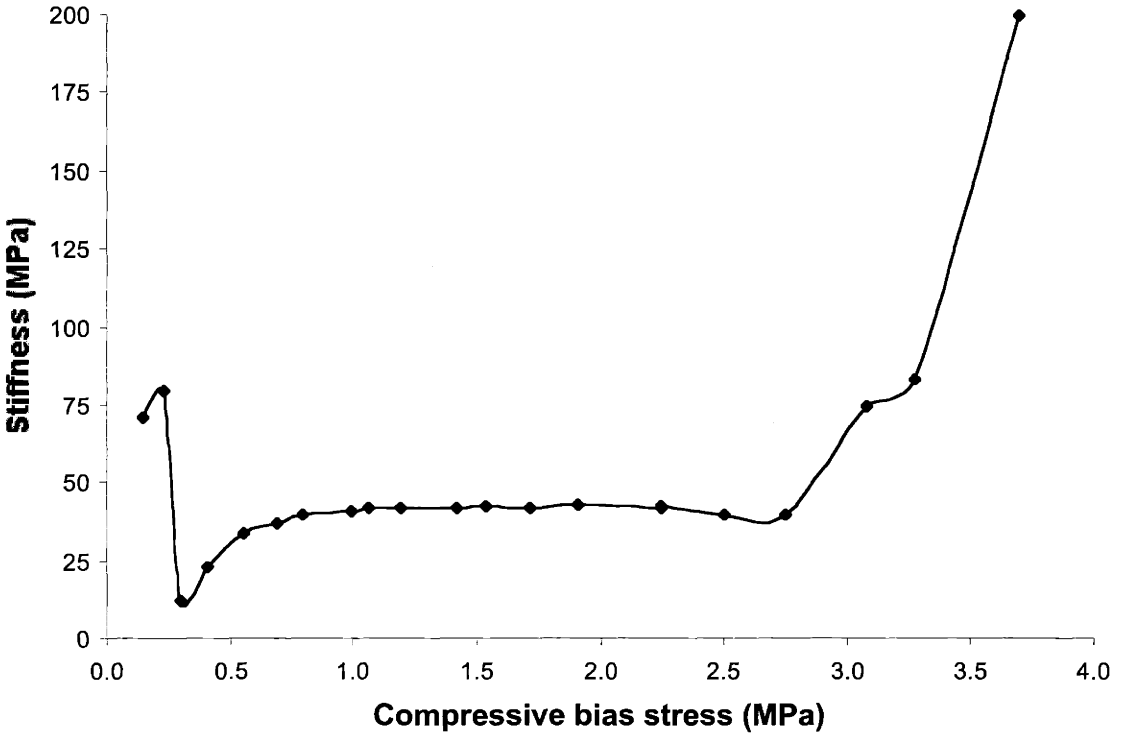

Figure 3.10: Twinning stiffness for 2 Hz stress vs. strain loops versus bias stress. These values compare favorably with the stiffness at constant field: twinning stiffnesses are between 30 and 40 MPa, and the apparent elastic stiffness is between 100 and 130 MPa.

3.4 Magnetization versus field

Figure 3.11 shows the flux density versus applied magnetic field as measured by a single-turn flux coil around sample B at 2 Hz actuation under different bias stresses. The negative field portion of these loops is symmetric with the exception of high, negative-field noise. The cause of the noise could be the result of electrical instability of the power supply at high negative drive levels. It should be noted that these loops are not corrected

for the demagnetizing field. The demagnetizing field is smaller than the main contribution of the anisotropy energy.

There are three general regimes of behavior at occur in Figure 3.11: easy-axis magnetization at low bias stresses, hard-axis magnetization, a magnetization jump to saturation at intermediate stresses, and at high bias stresses hard-axis magnetization occurs. In the intermediate bias stresses regime, the dynamic magnetization vs. field curves are similar to the VSM measurement in Figure 1.14. The behavior of hard-magnetic materials that is noticeably missing: Ni–Mn–Ga does not demonstrate a coercive field or a remanent magnetization.

Magnetic-domain wall motion usually occurs during the initial magnetization of the sample. As shown in Figure 3.11, this process is complete at fields of approximately 50 kA/m, regardless of bias stress. As the field increases to about 100 kA/man, hard-axis magnetization in type 2 variants occur at intermediate bias stresses (see glossary). Above the inflection at 100 kA/m, a jump in magnetization occurs as twin boundary motion starts. Confirmation of twin boundary motion at this field is observed in Figure D.2. (It is noteworthy that the coercive field at which twin boundary motion starts is relatively insensitive to bias stress for sample B. However, for sample A, the coercive field in Figure 3.2 plotted in Figure 4.4 is highly dependent on the bias stress.) Following the jump in magnetization, saturation is attained.

Upon field reversal, two different characteristics are evident. For low and intermediate bias stresses, the magnetization follows the easy, initial magnetization path. No sudden magnetization drop occurs as the field decreases to 100 kA/m, confirming that the magnetization is not reversible by itself. For the high bias stresses, the decreasing magnetization follows itself closely resulting in nearly reversible hard-axis magnetization.

Further increases in bias stress above 2.05 MPa neither suppress the magnetization moment nor do they lack hard-axis magnetization. These loops could be superimposed on the increasing field, hard magnetization process for 2.05 MPa. However, the return demagnetization of these higher bias stresses closely follows the increasing-field, hard-axis magnetization. The result is that there is virtually no hysteresis for these fully clamped magnetization loops.

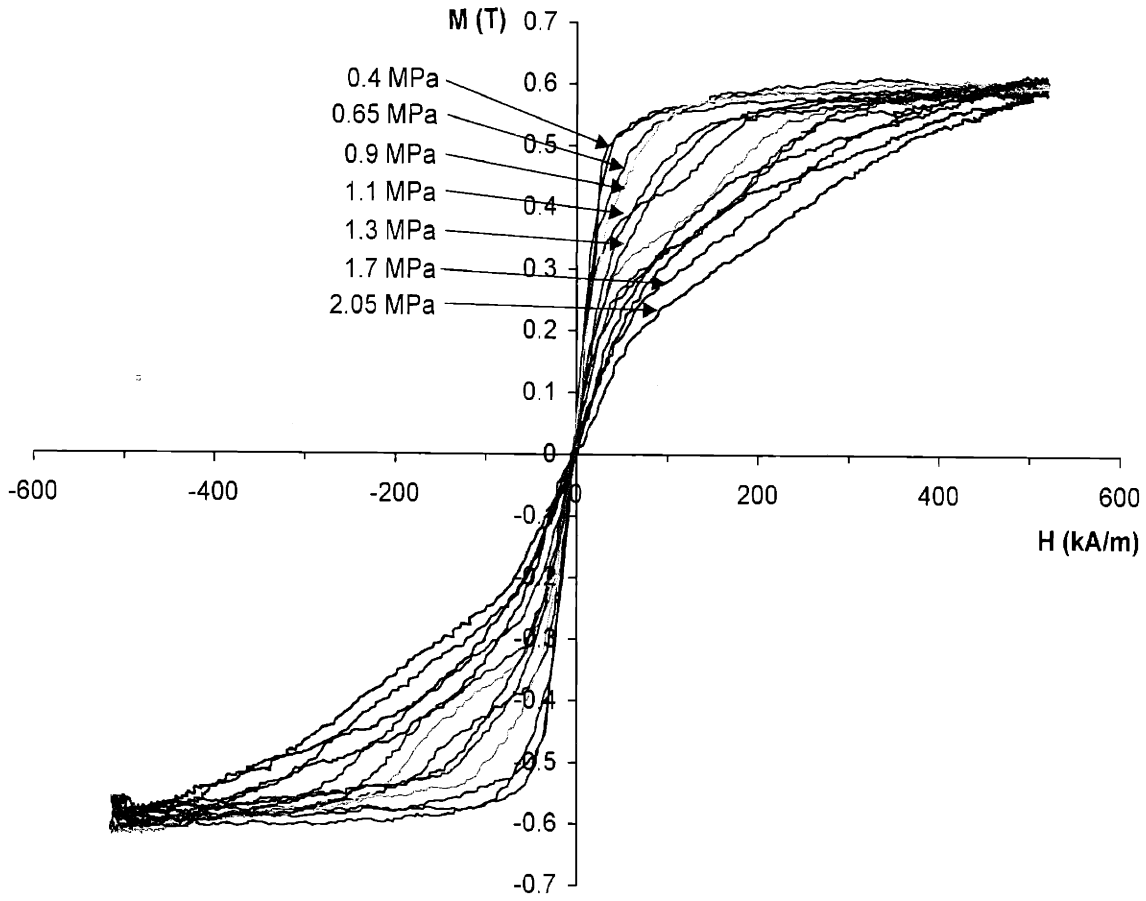

Figure 3.11: Magnetization versus applied magnetic field by flux coil measurements at 2 Hz actuation under different bias stresses.

The low-field susceptibility and saturation magnetization are plotted as a function of bias stress in Figure 3.12. On the left, the low-field susceptibility decreases in a quadratic fashion with bias stress: $\chi = 5\sigma^2 - 20.1\sigma + 23$ where σ is in MPa. The unclamped susceptibility approaches 11 at low bias stresses and 3 at high bias stresses. At stresses below 0.8 MPa, the susceptibility changes little as the magnetization vs. field

curve shows easy-axis magnetization behavior. At the highest stresses primarily hard-axis magnetization is evident, reducing the susceptibility to about 3..

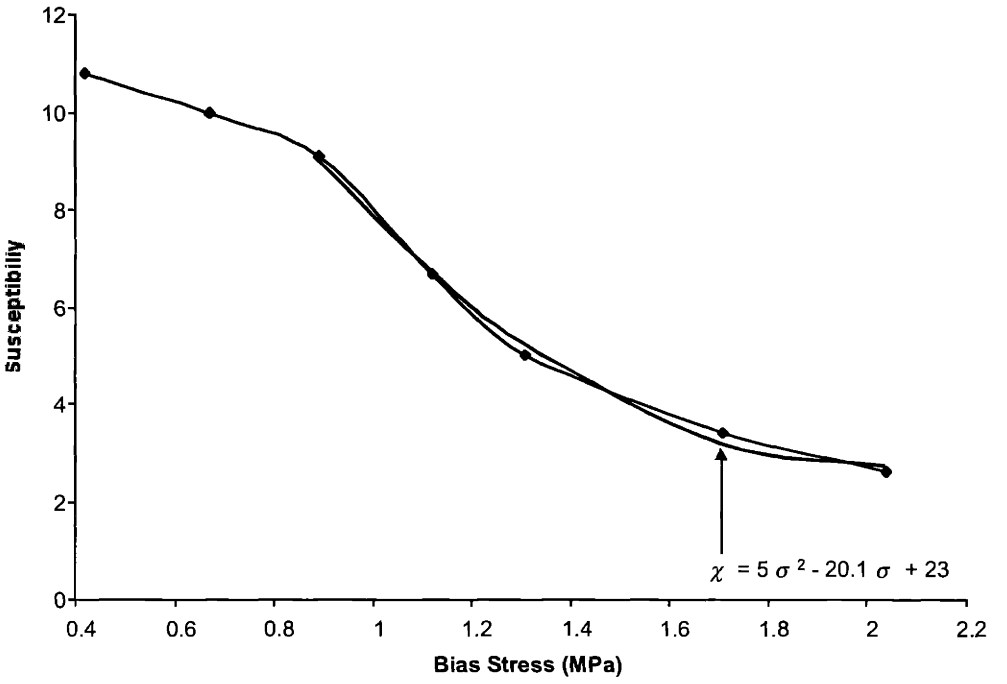

Figure 3.12: Low-field susceptibility follows a decreasing quadratic trend as given by the formula, $\chi = 5\sigma^2 - 20.1\sigma + 23$ where σ is in MPa.

3.5 FREQUENCY-DEPENDENT MEASUREMENTS

Results of frequency-dependent simultaneous measurement of field, strain, stress, and magnetization at an average bias stress of 1.7 MPa were carried out with the X4 revision of DATS. However, due to bandwidth limitations (specifications from Table 2.1) only strain versus magnetic field could be reported for sample A. Frequency-dependent magnetization versus field curves are also reported for sample B at an average bias stress of 1.1 MPa and are shown and described in Appendix D. These results are plotted as

families of curves, in which the frequency of the test varies, while keeping the average stress relatively constant. Interpretations of these results are given in Section 4.2.

3.5.1 Strain vs. field

Results of dynamic strain actuation versus applied magnetic field are shown in Figure 3.13 for actuation frequencies of 2 Hz to 100 Hz and Figure 3.14 for 100 Hz to 500 Hz for bias stress of 1.5 MPa. At higher frequencies, data needed to be gathered within a couple of seconds after the power supply was turned on. Because the sample's martensite transition temperature is relatively close to room temperature, at high frequencies, sample heating caused the actuation response to rapidly decay. The effects of the sample heating were a serious concern and were minimized in Figure 3.13, Figure 3.14, and Figure 3.15 by only reporting the first strain vs. field cycle. This is discussed in more detail in Chapter 4.

There are several prominent changes of the dynamic strain response as the frequency increases from 2 Hz to 100 Hz. First, a slight decrease of the strain response could be due to the inability of slower twin boundaries to keep up the increasing frequency. It could also be due to operating closer to the resonant frequency. Second, the increase in apparent coercive field with frequency, and what it means for loss in the material, is discussed in the following chapter. Finally, the phase between the strain and

the field (as measured by the field at which maximum strain occurs) increases with frequency in Figure 3.16.

Because of increased inductive reactance in the electromagnet the peak field starts to decrease at actuation frequencies above 300 Hz (see also Figure C.3). The rounded corners of the 350 Hz measurement indicate that it could be close to magnetomechanical resonance. At the highest frequency, 500 Hz, the presence of asymmetric strains for positive and negative field is apparent as well as anti-resonance.

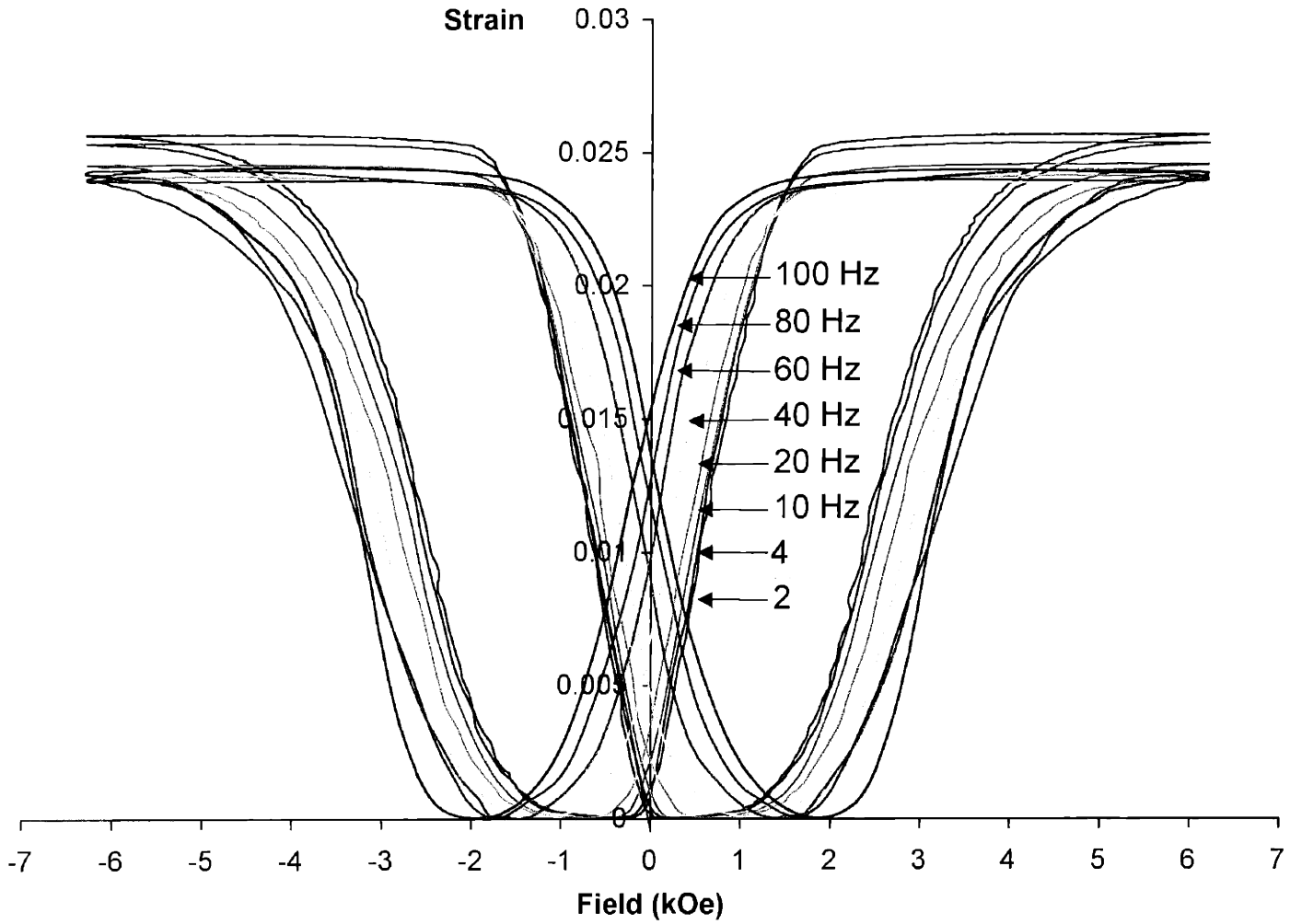

Figure 3.13: Dynamic MFIS actuation from 2 Hz through 100 Hz for a bias stress of 1.7 MPa.

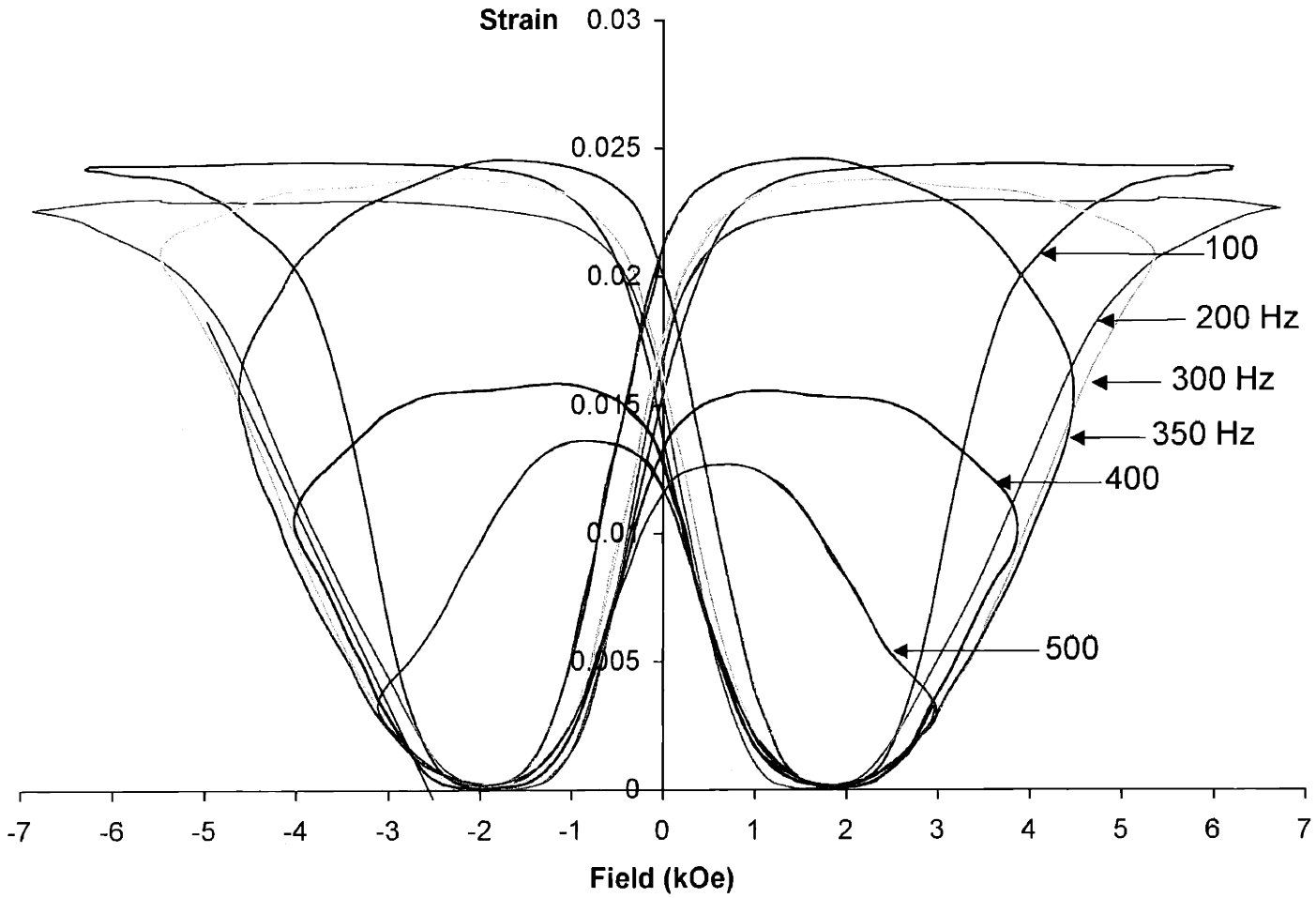

Figure 3.14: Dynamic MFIS actuation from 100 Hz through 500 Hz for a bias stress of 1.7 MPa.

Figure 3.15 shows the maximum magnetic field induced strain for two different experimental apparatus: the X1 and X4 electromagnet and their corresponding hardware. The top portion of the figure shows the magnetic field as a function of field drive frequency (which is half of the actuation frequency) applied to the sample from X1 and X4 electromagnets. The frequency bandwidths of these electromagnets are limited by the voltage and current specifications of the power supply. Discussion of the frequency bandwidths of the electromagnets may be found in Appendix C.

The bottom portion of Figure 3.15 shows the maximum magnetic field induced strain versus actuation frequency for both of these electromagnets. For the X1 curve, the maximum strain remains relatively constant at about 2.6% up to the maximum bandwidth at 140 Hz. Above the maximum bandwidth for the X1 electromagnet, the maximum strain decays at -0.5% / $(\text{kOe Hz})^{-1}$. For the X4 curve, the maximum strain is about 2.6% up to 100 Hz, then increases to about 3% at the mechanical resonance (120 Hz) and dips to 2.3% at an anti-resonance (220 Hz). The rolloff of maximum strain occurs at about 350 Hz and a strain of 1.3% is observed at an actuation frequency of 500 Hz. The maximum strain only starts to decrease at a maximum magnetic field less than 4.5 kOe and the strain decays at a rate similar to that of the X1 electromagnet of -0.5% / $(\text{kOe Hz})^{-1}$.

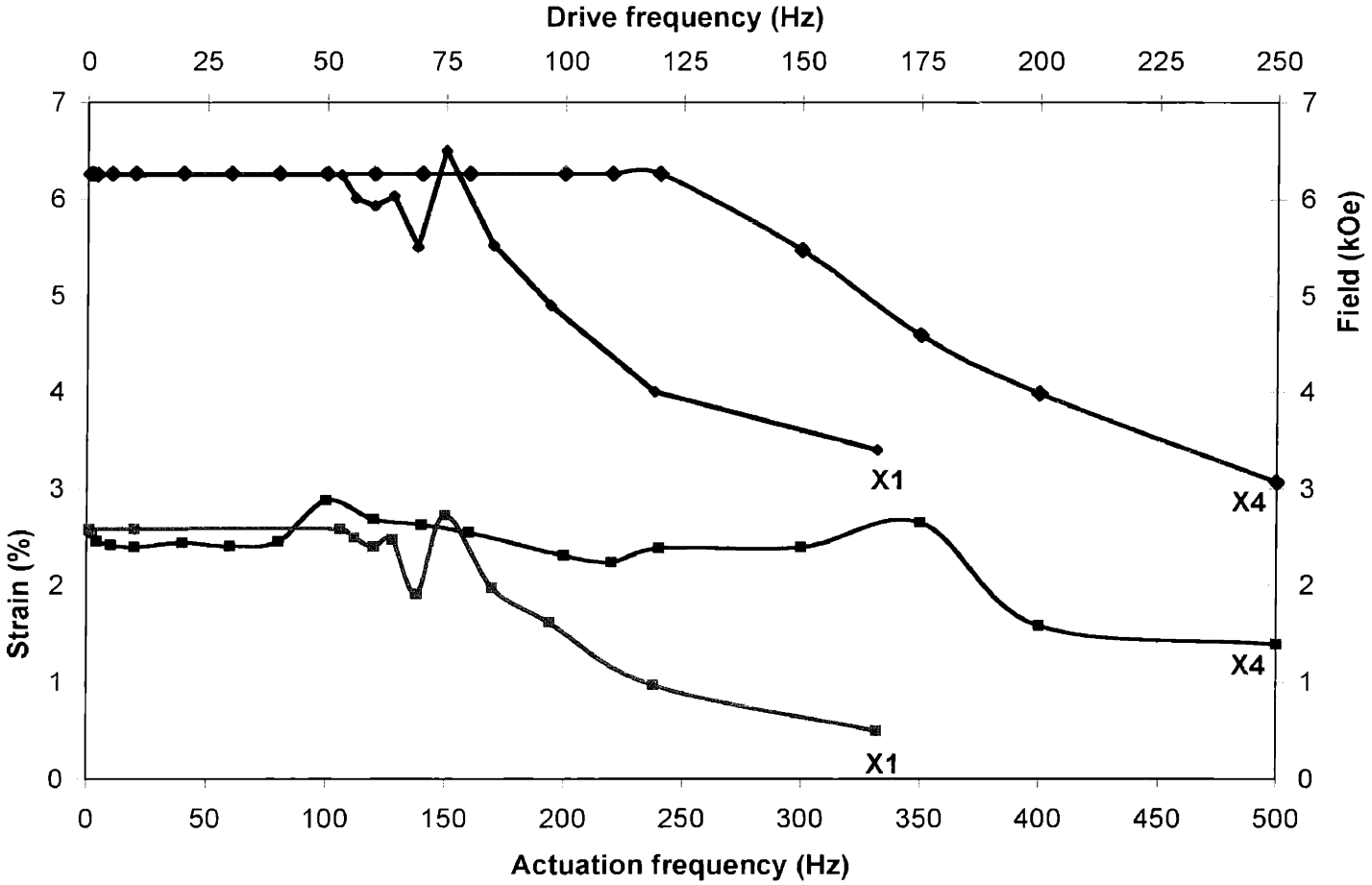

Figure 3.15: Above is the applied magnetic field at each drive frequency. Below is the saturation strain versus actuation frequency. These results indicate the saturation MFIS measured is dependent upon the mechanical system and electromagnet used, X1 or X4.

From the frequency-dependent strain vs. field data, the phase lag between the two variables can determined. Figure 3.16 shows the phase lag as a function of the actuation frequency. From 2 Hz to 100 Hz the phase lag is less than 10°. However, from 100 Hz to 400 Hz the phase lag increases in an almost linear fashion. The resonant frequency is determined to be 275 Hz by picking the frequency at which the phase lag passes through 90 degrees. A discussion of how the phase lag indicates the degree of damping of the system is follows in the next chapter.

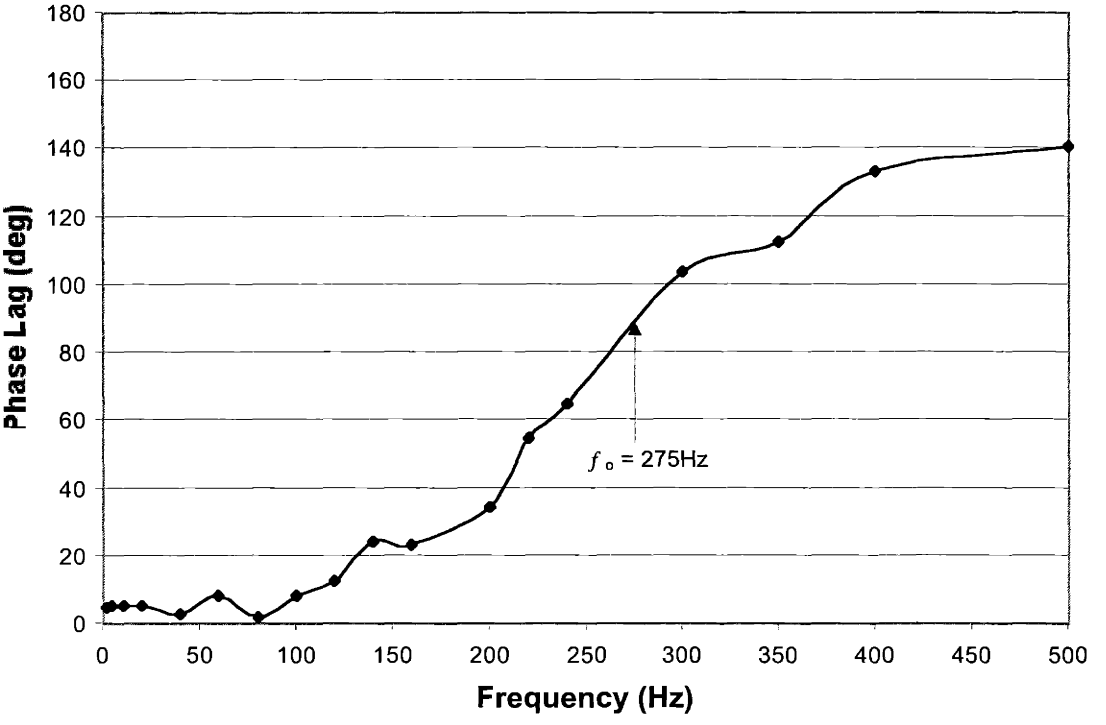

Figure 3.16: Phase lag of strain with respect to the applied field. The apparent system resonant frequency is 275 Hz.

3.6 RESULTS SUMMARY

Simultaneous measurement of both mechanical and magnetic variables yields a rich set of data. With this data, new connections may be formed about the physics of actuation behavior, the reporting of thermodynamic properties and implications for technological use of Ni–Mn–Ga FMSAs. The data presented followed from two experiments: bias stress dependent MFIS actuation at 2 Hz; and frequency-dependent MFIS actuation at 1.7 MPa bias stress. A correlation between the stress and other variables at high frequencies would have proved valuable, but was not possible because DATS X1 limitations of capabilities. On the other hand, 2.6% dynamic strain actuation, MFIS strains up to 500 Hz, and bias stresses up to 3.8 MPa exhibiting twin-boundary motion are accomplishments that have not yet been achieved elsewhere.

Chapter 4

4 DISCUSSION AND ANALYSIS

Observations of cyclic deformation behavior over a range of mechanical constraints are important because they distinguish properties that transducer designers can use from more fundamental properties of the material. In this chapter, observations of cyclic deformation are used also to characterize macroscopic behavior and hypothesize microscopic mechanisms applicable to cyclic actuation of FSMAs. These behaviors include energy loss, hysteresis and fatigue. Characterization of these macroscopic behaviors in FSMAs would be crucial information for an engineer designing a transducer device. Also, understanding the microscopic mechanisms that result in these undesired behaviors helps guide a materials scientist toward ways of controlling and manipulating these behaviors possibly through alloying, heat treatment, or processing.

In the previously unobserved stress vs. field behavior shown in Chapter 3, magnetization rotation results in magnetostriction stresses and this stress may play a role in initiating twin boundary motion. This explanation is compared here with other possible microscopic mechanisms. A phenomenological model is presented in Chapter 5 that incorporates the effect of the magnetization rotation on the observed stress as the field increases and twin boundaries move.

Macroscopic models and microscopic mechanisms are also proposed for describing frequency-dependent strain response and energy loss. Phonon softening may play roles in both easing the stress at which actuation occurs, and providing a mechanism to transfer energy loss out as heat. Eddy currents heat magnetic materials by inducing electric currents in a changing magnetic flux density. The faster the magnetic flux density changes, the greater the current to heat the material. Macroscopically, the saturation strain response versus frequency can be modeled by a forced damped harmonic oscillator and by response function theory.

The goal of this discussion and analysis is to suggest connections between these observations and different microscopic mechanisms in order to gain a better understanding micro-mechanisms of FMSA dynamic actuation. Multi-variable data gives an opportunity to investigate not only dynamic properties and their dependencies, but also probe the sources of inefficiencies in the material.

4.1 Hysteretic energy loss, loss tangents, and coercivity

This section focuses on establishing possible connections between hysteretic energy loss and coercivity and their effects on coupling coefficient estimations. To do this, the causes of energy loss is partitioned into magnetic, mechanical, and magnetomechanical (coupling) sources. The energy loss is manifested in two measurements presented here: loss tangent and coercive field as functions of the bias

stress. Contributions to these measurements may be attributed to sources in which certain microscopic or meso-scale mechanisms are important. These sources of energy loss are explained in the following section.

4.1.1 HYSTERETIC ENERGY LOSS

Possible sources of hysteretic energy loss in FSMAs can be separated into magnetic, mechanical and coupling components. Mechanical energy loss occurs each actuation cycle primarily by irreversible yielding when twin boundary motion occurs and over many actuation cycles by fatigue, as the result of defect damage accumulation. Magnetic energy loss at low frequencies comes from primarily domain wall motion and domain wall pinning on defects. The involvement of magnetization rotation to produce magnetostrictive stresses and its importance in actuation will be explored in more depth here.

4.1.2 LOSS TANGENTS

The magnetic loss tangent is calculated from the relative areas within a cycle (the energy density loss) in a magnetization versus field plot compared to the input energy density. For example, the magnetic loss tangent is given by:

$$\tan\delta = \frac{1}{2\pi}\frac{\Delta W_M}{W_M} \qquad 4.1$$

where ΔW_M is the magnetic energy loss per cycle and W_M is the magnetic energy put into the material during half a cycle. See Appendix B for further explanation of loss tangent

calculation and derivation. Analogous equations for mechanical, $\tan\phi$, and magnetomechanical, $\tan\theta$, loss tangents are also given. Figure 4.1 shows the experimental magnetomechanical and mechanical loss tangents and the calculated magnetic loss tangent versus bias stress as calculated from equation 4.1.

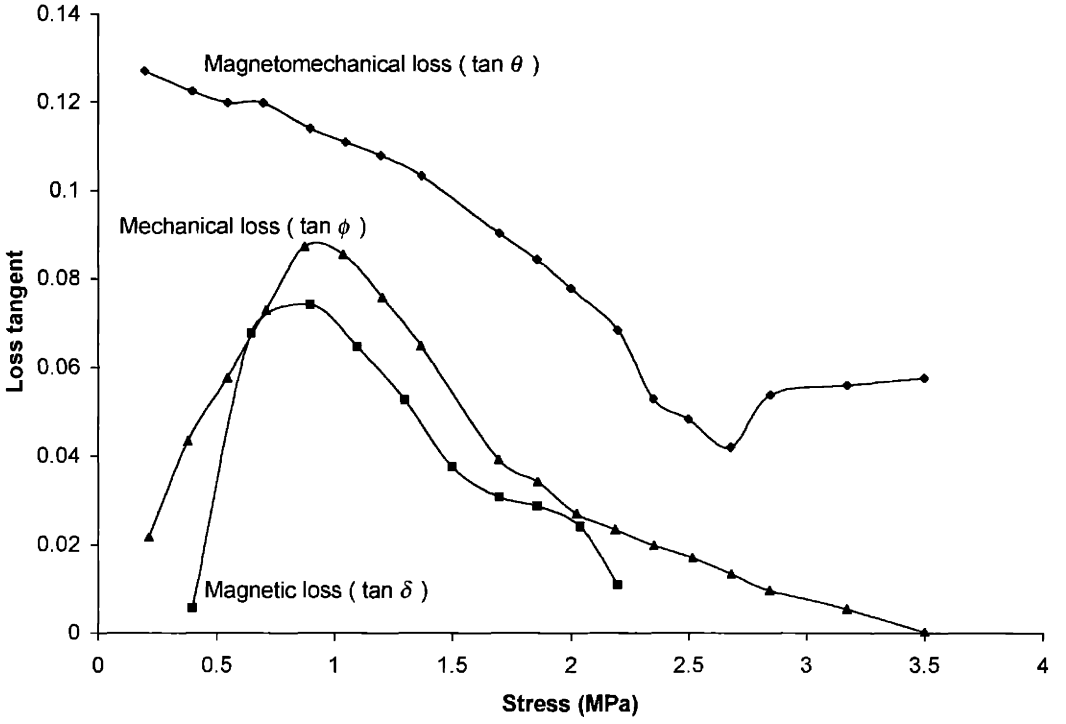

Figure 4.1: The magnetomechanical, mechanical and magnetic loss tangent calculated from equation 4.1 using experimental results as a function of the bias stress.

The variation of the mechanical loss tangent with bias stress can be explained more clearly if it is thought of as a scaled ratio of the loss over the work. Figure 4.2 shows the elastic energy density stored by the FSMA, which increases linearly with field. The mechanical loss peaks at 150–175 kA/m where cyclic MFIS actuation is greatest.

Mechanical loss at the extremes is small because only a small proportion of twins yield to provide cyclic MFIS. Conversely, for static tests, ϕ would approach 90° as nearly all energy put into the FSMA would result in irreversible twinning strain. Only for small stresses ($\sigma < \sigma_{tby}$) is the input energy recoverable. A slight increase in the magneto-strictive stress in Figure 4.7, may account for the more gradual decrease of the mechanical energy loss as the bias stress increases above 2.0 MPa in Figure 4.1. It is believed that the mechanical energy loss generates heat in the FSMA. At low frequencies, it is likely that the heat can be adequately conducted away. However, at higher frequencies, this may not be the case. Frequency-dependent loss and subsequent sample heating is explored in more detail in Section 4.2.

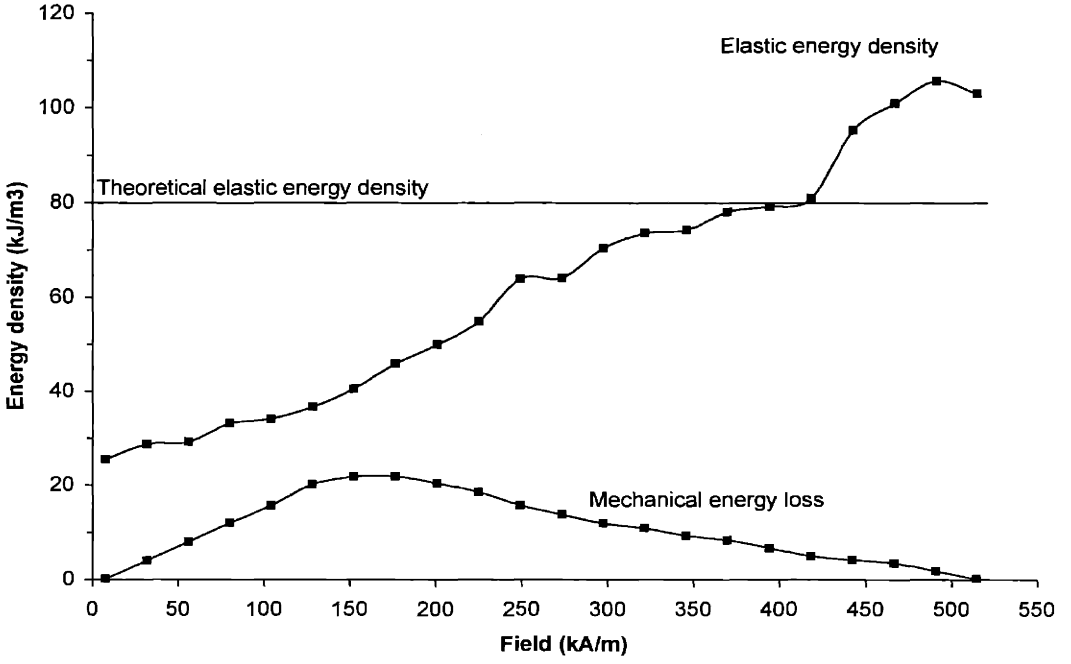

Figure 4.2: The elastic energy density stored by the FSMA increases in a linear fashion. The mechanical loss peaks in the middle where reversible actuation is greatest. Mechanical loss at the extremes is small because only a small proportion of twins yield to provide reversible strains. It can be compared to the theoretical energy density provided by the first order linear constitutive equations.

The magnetic loss tangent shown in Figure 4.1 The result for magnetic loss in Figure 4.1 is from evaluation of the stored energy and loss of sample B in Figure 3.11 though M vs. H data was not collected for sample A. Through observation of the area to the left of the increasing magnetization in Figure 3.11, the stored magnetic energy increases as bias stress increases. At intermediate bias stresses the difference between the hard-axis magnetization and the easy-axis demagnetization results a maximum area within the magnetization loop maximum magnetic loss. At the bias stress extremes, the

loss is small because of easy-axis magnetization at low bias stresses and hard-axis magnetization at high bias stresses. The magnetic loss tangent could be calculated using the final result in equation B.30: $\tan\delta = \tan\phi - \tan\theta$.

The magnetomechanical loss tangent shown in Figure 4.1 can be partly interpreted using the explanations of the coupling loss described in the following sections section. The magnetomechanical loss can be thought of as the difference of the magnetocrystalline anisotropy energy from infinite magnetocrystalline coupling. Therefore, the finite magnitude of the magnetocrystalline anisotropy energy essentially limits the amount of energy that can be transferred from the magnetic field to the crystal structure. This allows the type 2 variant magnetization to rotate in a field. Thus the magnetomechanical loss tangent should decrease in an increasing field as the difference between infinite coupling and the magnetocrystalline anisotropy decreases, as shown in Figure 4.3.

The contributions to the magnetomechanical loss tangent in Figure 4.1 could involve the two other sources of inefficiencies. First, the coupled 90° domain walls can "slosh" from one edge of the twin boundary to the other in response to field, though many twin boundaries remain stationary at low and high bias stresses. Twin boundaries that yield and are dragged by domain walls may maintain a relatively constant displacement, or "slack" between the boundaries. Thus, the expectation based upon this

assessment is that magnetomechanical loss tangent would be of some finite value at low and high bias stresses and would be greater at intermediate stresses. The expected loss tangents based upon the rationalizations above might have the form illustrated in Figure 4.3.

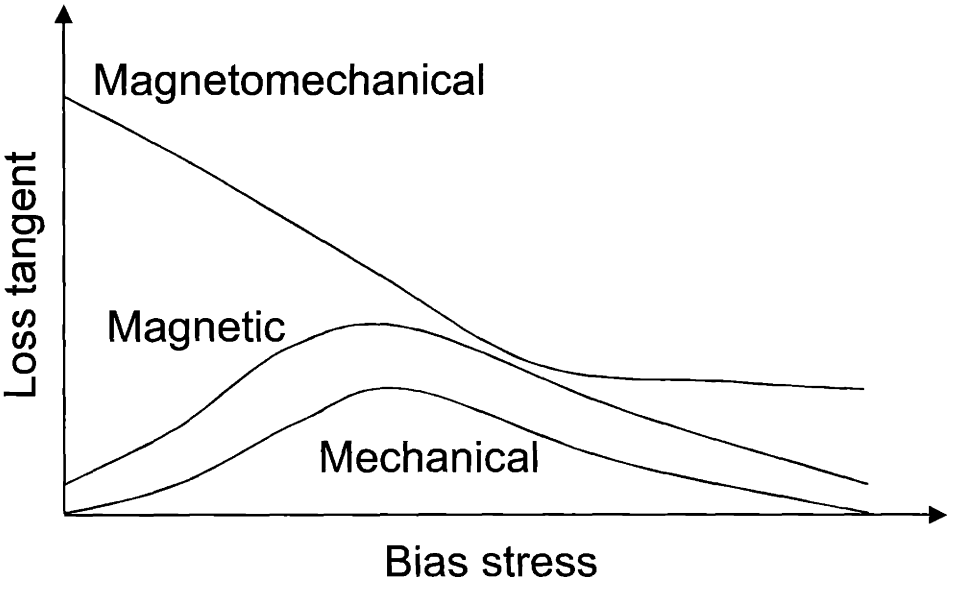

Figure 4.3: Expected mechanical, magnetic, and magnetomechanical loss tangents as a function of bias stress.

4.1.3 COERCIVE FIELD

Figure 4.4 shows the coercive field measured at zero strain, one-half strain, and maximum strain from Figure 3.2 plotted as a function of the average bias stress in sample A after $N \approx 100{,}000$ cycles. The zero-strain coercive field is the field at which twin boundary motion starts (or in terms of the stress $\sigma_{threshold} \geq \sigma_{tby} + \sigma_{ext}$) and it also corresponds to the stress plateau for the increasing field branch in Figure 3.6, as

demonstrated earlier. The maximum-strain coercive field (or in terms of the stress $\sigma_{ext} \geq \sigma_{tby} + \sigma_{threshold}$) corresponds to the change in field required to initiate sample compression from the spring. (The one-half strain coercive field appears to have the character of the zero-strain coercivity at lower bias stresses. At higher bias stresses, the one-half strain coercive field approaches the maximum-strain coercivity.) The general U-shaped bias-stress dependence of these two curves is similar to coercive-field versus bias-stress plots observed by Bozorth [58] for crystalline NiFe and O'Handley [59] for Ni–Fe glassy alloys.

Figure 4.4 is a plot of the coercive field vs. bias stress after approximately $N \approx 100{,}000$ cycles. A corresponding plot of the coercive field vs. bias stress at $N \approx 1{,}000$ cycles in Figure D.3 reveals a difference in magnitude between the coercive fields in the two figures. An interpretation of this cycle-number-dependent difference is that there is accumulation of defect damage in the FSMA with increasing actuation cycles. Specifically, a cellular dislocation structure might develop gradually as a result of cyclic deformations, which would hinder the movements of domain walls and twin boundaries that produce MFIS. Therefore a greater coercive field is necessary to initiate MFIS with increasing cycle number. If the cyclic increase of coercivity is subtracted, the results are the lower of the zero-strain and maximum strain curves in Figure 4.4.

The zero-strain coercive-field vs. bias stress curve is the most straightforward to explain because the coercivity source cannot involve any processes that produce in MFIS. One well-known source of coercivity in magnetic materials is pinning of the motion of 180° magnetic-domain walls [60]. Magnetic-domain wall motion usually results in growth of magnetic domains during the initial magnetization that favor a reduction in the Zeeman energy, $-M \cdot H$. As shown in Figure 3.11 for sample B, this process is complete at fields of approximately 50 kA/m, regardless of bias stress. MFIS starts at about 100 kA/m for all bias stresses and is shown more clearly in Figure D.2. In addition to pinning of 180° domain walls, 90° domain wall "sloshing" and magnetization rotation are also responsible for the zero-strain coercive field, prior to MFIS.

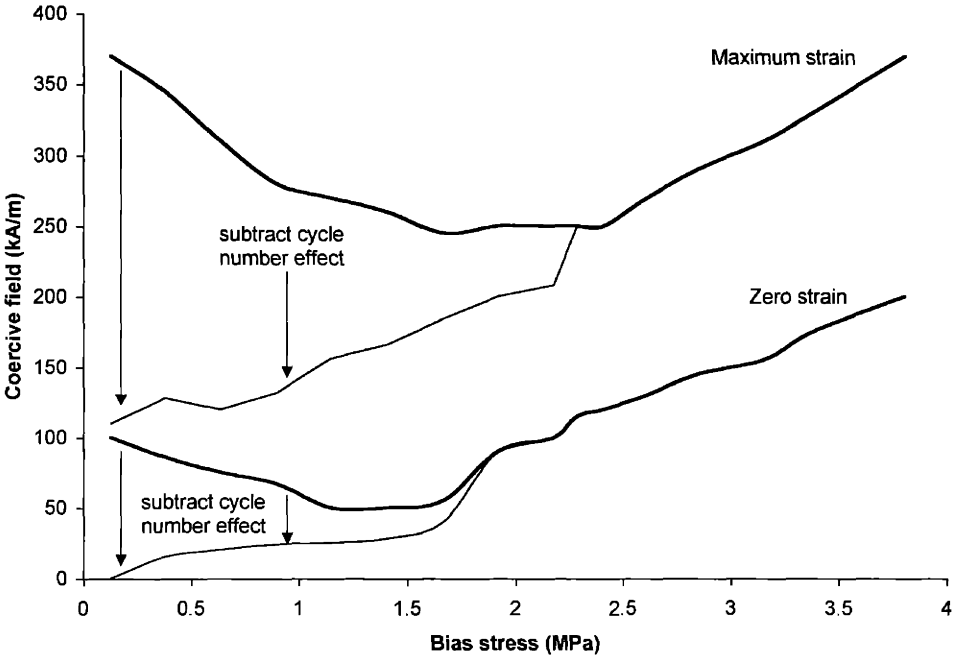

Figure 4.4: For sample A after $N \approx 100{,}000$ cycles, strain vs. field coercive field at the maximum field-induced strain, at the minimum spring compression strain (bold lines). When the coercive field at $N \approx 1000$ cycles (Figure D.3) is used as a baseline, the difference is thought to be due to the increased number of cycles. (thin lines)

The maximum-field coercive field may have additional contributions, which account for its greater magnitude. If the assumption is true that domain wall pinning and "sloshing" still occur at maximum-strain, then this component of magnetic coercivity can be subtracted from the maximum-strain coercive field. The lowest curve in Figure 4.5 shows the resulting coercivity with the zero-field coercive field subtracted out. The maximum strain coercive field after these corrections shows near linearity over this range of bias stresses.

An additional contribution to the coercive field is the twin boundary yield stress, which demonstrates the bias stress linearity. Even at the maximum magnetic field, the twin boundary yield stress needs to be overcome. An approximation can be made of the twin boundary yield stress that is equivalent to the remaining coercive field (by using a value of 5.5×10^{-6} MPa / (A/m) from the linear slope of the thermodynamic stress vs. field behavior). The calculated twin boundary yield stress is 0.55 MPa at the lowest bias stress and 0.83 MPa at the highest bias stress. These stresses are about twice the apparent yield stress (magnetostrictive stress) in Figure 4.7. But after reviewing how dramatically the yield stress changes with field in Figure 1.15, this could account for the remaining coercivity. Thus, the contributions of the maximum-strain coercive field can be accounted for by the increase in cycle number, a correction for the zero-field coercive field and the magnitude of the twin boundary yield stress.

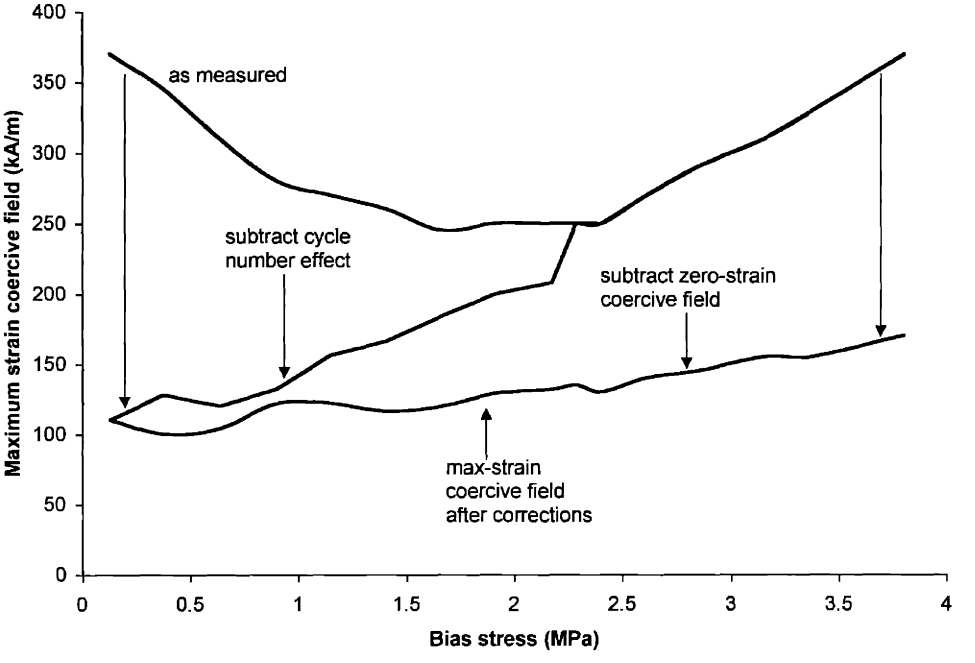

Figure 4.5: Maximum-strain coercive field corrected for cycle number. minus the zero-strain coercive field versus bias stress. This should represent the coercive field not due to domain wall motion or magnetization rotation.

4.1.4 MAGNETOMECHANICAL ENERGY LOSS SOURCES

Possible sources of magnetomechanical energy loss are explored here. A source of magnetomechanical coupling energy loss is the result of magnetocrystalline anisotropy energy's finite magnitude. Another magnetomechanical coupling energy loss source is the imperfect binding of 90° domain walls to the twin boundary. There are two distinctions for imperfect binding due to the difference of the twin-boundary width (~5 Å) as compared to the domain wall width (~200 Å). Even if the twin boundaries are stationary, the magnetization rotates 90° smoothly over this entire length due to the

magnetic exchange energy. The exchange energy counteracts the desire of the magnetocrystalline anisotropy energy to point the magnetization towards the martensite *c*-axis. In effect, the exchange energy distributes the magnetocrystalline anisotropy energy over the width of the boundary. Thus, the magnetization rotates away from the *c*-axis within the domain wall region, which results in a loss of coupling energy.

The second distinction is when the domain wall or twin boundary moves in response to a field or stress, respectively, there is some "slack" before the other boundary starts to move with it, i.e. some displacement between the boundary centers. The twin boundary is a relatively sharp boundary, but requires a minimum twin boundary yield stress to start moving with the domain wall following easily. Though the domain wall moves relatively easily, its diffuse nature necessitates that its center move away from the twin a distance before hard-axis magnetization develops sufficient magnetostrictive stress yielding the twin boundary. Thus, the above are three inefficiencies that give rise to coupling the magnetization rotation to the crystal axis "rotation."

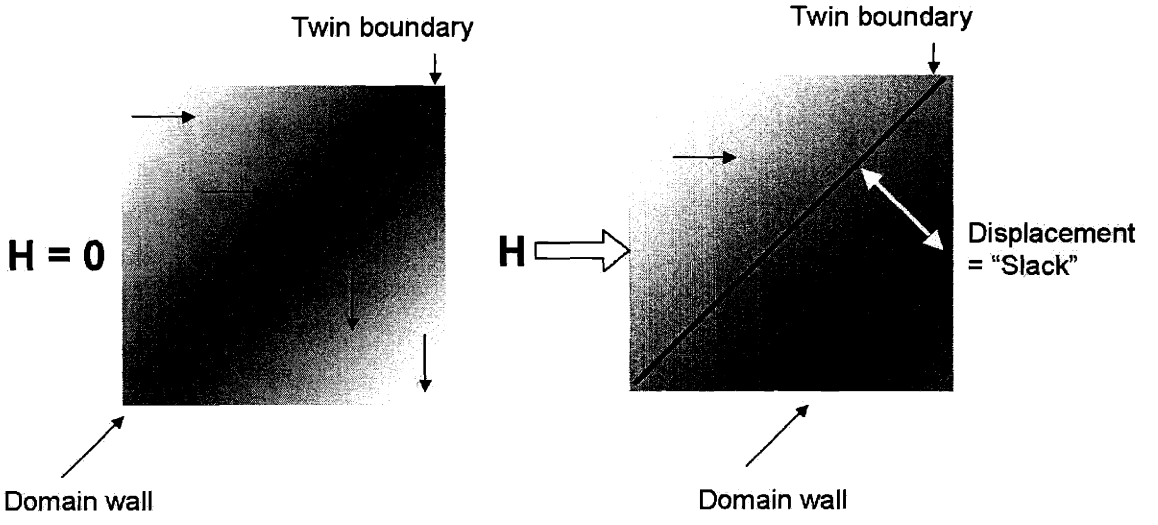

Figure 4.6: Illustration of how a wide 90° domain wall is offset from a twin boundary by some displacement. This "slack" can develop in response to an applied magnetic field.

Two ways energy loss can be quantified are by measuring the coercive field and also by measuring the energy loss and describing it in terms of loss tangents. These expressions of FSMA inefficiency are interpreted in the following sections.

4.1.4.1 Magnetization rotation process

In order to determine the stress contribution due to magnetization rotation, it must be measured before twin-boundary motion starts. Figure 3.6 showed strain vs. field and stress vs. field plots for sample A at an average bias stress of 1.5 MPa. In this figure, the stress initially increases quadratically due to a magnetoelastic process as the magnetization rotates. This stress is sensed at the load cell when the magnetization in type 2 variants is rotated into the field direction. When the plateau is reached

magnetization rotation does not continue without the crystal structure rotating also. From the perspective of the magnetic moment, the magnetization will rotate in an increasing magnetic field until a twin boundary sweeps past it. Then the magnetic moment returns to its easy, *c*-axis alignment, but in a new orientation. Thus, the magnetoelastic process that generates stress is separated from the stress developed by the sample straining against the spring. When the magnetic field starts to decrease, the stress is quadatrically related to the field ($\sigma \propto 1-h^2$) until reverse twin boundary motion starts. For reverse twin boundary motion to be possible, the spring must be able to overcome the twin boundary yield stress and the decreasing field.

The magnetoelastic stress at the coercive field in Figure 3.2 corresponds to the onset of twin-boundary motion in Figure 3.8. From these curves, the stress contributions from magnetostriction and MFIS are tabulated versus the average bias stress of the test in Figure 4.7. At the lowest and highest bias stresses, the magnetostrictive stress is the predominant mechanism for creating stress before MFIS. Though strain on the order of only 100 ppm is associated with the magnetostriction stress, magnetostriction may play an important role in generating the stress needed to initiate twin-boundary motion. Once MFIS starts, twinning plays a significant role in generating useful work.

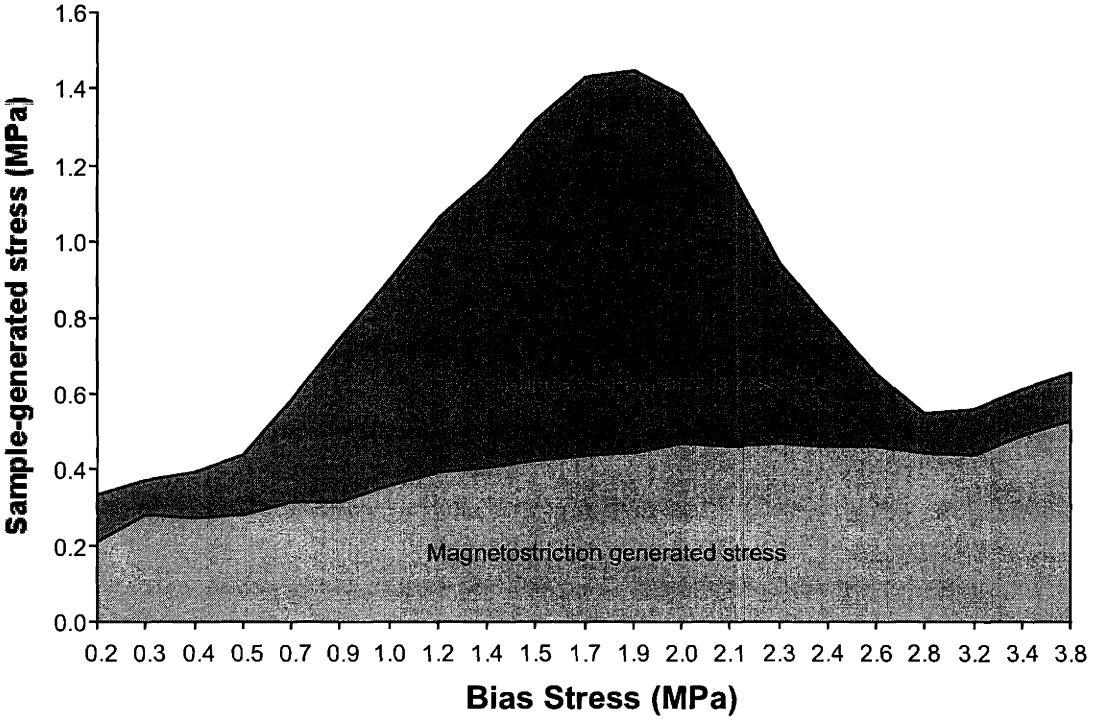

Figure 4.7:Magnetostriction-generated stress before the onset of twin-boundary motion and the total stress developed within the material in sample *A*.

4.1.5 HYSTERETIC ENERGY LOSS SUMMARY

In this section, possible explanations are explored for energy loss in Ni–Mn–Ga FSMAs. Two ways in which energy loss is apparent is through the calculation of the loss tangent and the coercive field. Using the micro-mechanisms that are thought to exist in materials like Ni–Mn–Ga FSMAs, the loss tangent and coercive field contributions can start to be understood. An important role of magnetization rotation is the generation of the magnetostrictive stress necessary for twin boundary yielding. Magnetomechanical coupling loss is explained by finite strength of the magnetocrystalline anisotropy.

Furthermore, magnetomechanical coupling loss can also be explained by the strength of the exchange energy, which promotes a gradual magnetization transition across a domain wall in contrast to the sharp, narrow structural discontinuity of a twin boundary. This results in the domain wall "sloshing" around, relative to a moving or stationary twin boundary. The mechanical losses are thought to be the source of sample heating and are highly frequency dependent. Exploration of the frequency-dependent actuation response and the associated losses follow in the next section.

4.2 Frequency response and loss

This section explains possible sources of frequency-dependent loss in Ni–Mn–Ga FSMAs. In the 1 to 500 Hz frequency range, fundamental energy loss mechanisms significantly affect the dynamic actuation response. There may be other mechanisms that contribute significantly to actuation response in other frequency ranges. However, the mechanisms that provide heat to the material are prevalent at the lowest frequencies and they limit the dynamic actuation bandwidth of the FSMA. Two mechanisms, eddy currents and soft-mode coupling, that are thought to occur in Ni–Mn–Ga are considered in this section.

As temperature is uncontrolled in the frequency-dependent experiments, heat generation is a primary concern limiting the continuous dynamic actuation in Ni–Mn–Ga. A probable source of heat is from eddy currents that generate heat locally around domain

walls. One mechanism for FSMAs to dissipate this energy is through long-range transport of atom displacements called "soft" mode phonon vibration coupling. Also macroscopic mathematical models can be used to describe the resonant frequency of the experimental system with the forced damped harmonic oscillator, and the resonant frequency of the FSMA can be calculated with the response function theory. Estimations of the temperature-induced and power-supply-induced decay of the frequency response can be interpreted with mathematical models of the resonant frequency to achieve an understanding of the observed-actuation frequency response of Ni–Mn–Ga in Figure 3.15.

4.2.1 Magnetic field to lattice vibration coupling near the transformation temperature

One mechanism for transfer of mechanical energy loss to heat is by operating at a temperature and frequency that will allow phonons to readily absorb and transport over large distances energy stored (mechanical or magnetic for example) in the material. This occurs at the transition temperature and $f = 0$ Hz for static atomic displacements on the transition from one phase to another lower symmetry phase.

Upon transition to a lower symmetry phase, from austenite to martensite for example, certain resonant lattice vibration modes remain as static atomic displacements because the phonon is "frozen-in." These atomic displacements can remain "soft" so long

as the lattice-vibration resonant frequency is close to zero. This can be done by exciting the appropriate electrons optically, acoustically, electronically, or magnetically. As the material temperature deviated more from the transition temperature, the lattice-vibration resonant frequency increases. (This excitation at the right frequency and temperature can maintain the soft phonon.) The characteristics of how the resonance changes with temperature varies from material to material, but a schematic representing the generic temperature dependence of the resonant frequency is in Figure 4.8.

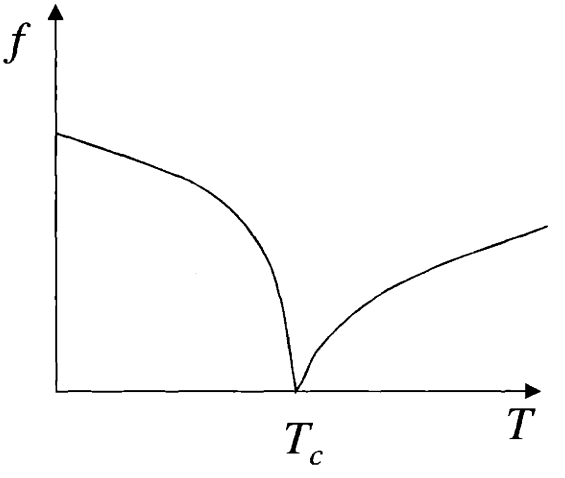

Figure 4.8: A qualitative representation of the temperature dependence of the soft-mode frequency near a second-order displacive phase transition (such as from austenite to martensite). (*after Lines and Glass*[61]).

If the material is pumped or driven close to the soft phonon frequency, strong resonance (induced phase transition) or dissipation (heat generation) can occur. Thus, as atoms are excited at temperatures closer to the transition temperature, the addition of energy from another source can induce the phase transition. If the source cannot provide

sufficient energy, an easing of the material's response may occur. In Ni–Mn–Ga, a magnetic field can induce a phase transition, or at least facilitate atomic shear displacements for twinning. If the material is driven too hard at the excitation frequency, the lattice vibrations could increase in magnitude, raising the temperature.

For many dielectric materials, dielectric dispersion occurs near the paraelectric to ferroelectric phase transition. Blinc and Zeks tabulate these frequencies for different materials [62]; for $AgNa(NO_2)$, dielectric dispersion can occur at frequencies down to 200 Hz, while for $Na(NO_2)$ the minimum frequency is 32 MHz, for example.

In Ni–Mn–Ga, if a static magnetic field is applied close to the transition temperature, the soft phonon may be amplified and a field-induced transition can occur. However, in this case, for a drive frequency of order 10^2, Hz significant soft phonon coupling may occur at 10 to 15°C below the martensite transition temperature. The coupling may possibly manifest itself by lowering the yield stress as which twin boundaries move or contribute nontrivial amounts of heat to the material. Decreasing the temperature below the transformation temperature increases the soft-mode frequency, which may, in turn, increase the twin boundary yield stress and decrease the phonon dissipation. Thus, the distinct possibility exists that soft-mode coupling is a source of yield stress benefit and hysteretic loss in Ni–Mn–Ga.

4.2.2 EDDY CURRENTS

A common cause of frequency-dependent coercivity and energy loss in magnetic materials is the generation of eddy currents. From Faraday's law, a time-varying magnetic flux within a circuit induces a voltage in that circuit. Furthermore, according to Lenz's law, this induced voltage will be such that the resulting current flow will contribute a magnetic flux that opposes the original time-varying magnetic flux. These induced currents tend to decrease the applied field's penetration into the material. Therefore, the inner portions of the material become magnetically "shielded." The exponential decay length of an AC electric field in a material due to induced eddy currents is given by the classical skin depth, $\delta = (\mu\sigma\omega)^{-1/2}$, where μ is the permeability, σ is the conductivity, and ω is the circular frequency. In FSMAs, the skin depth at 250 Hz is $\delta \approx 1$ cm, where $\mu_r = 3$, $\sigma = 1/\rho = 1.61 \times 10^6$ S has been used. This skin depth corresponds to the minimum dimension of sample B used in these frequency-dependent studies.

Since eddy currents flow in a material with some resistance, there is an Ohmic I^2R heating loss. According to O'Handley [38], the classical (uniform magnetization rotation) eddy current power loss per unit volume is,

$$\frac{P_{class}}{vol} = \frac{\omega^2 B_m^2 d^2}{48\rho} \qquad 4.2$$

where B_m is the maximum magnetic flux density, d is the thickness, and ρ is the resistivity. The classical eddy-current loss can be distinguished from the domain-wall eddy-current loss. Eddy currents circulate into and out of the domain wall as the local magnetic flux changes when the wall moves. The micro-eddy-current power loss per unit volume for a single domain wall is

$$\frac{P_{micro}}{vol} = \frac{P_{class}}{vol}\frac{W_{AB}}{2\pi^3 d} \qquad 4.3$$

where W_{AB} is the distance a wall travels during a half-cycle. These power losses can result in significant heating as shown in the next section. Equation 4.3 should apply in FSMAs., The area inside a B-H loop is exactly the energy per unit volume lost in one cycle of the hysteretic process. If the loop is traced at increasing frequency, it is observed that H_c increases and the loop becomes more rounded. The increase in loop area is a result of eddy currents induced in the sample by the increasingly rapid change in flux density (See appendix D.3 for frequency-dependent magnetization vs. field loops.)

4.2.3 HEAT GENERATION CALCULATIONS

Results in Figure 3.15 indicate that the strain response is only limited by the field drive frequency and the sample's ability to dissipate heat. Heat may be generated as a result of macro- and micro-eddy currents. Simple analytical calculations can establish the temperature rise in the material as a function of the frequency. Or, in direct observation with experiments, the time needed to increase the temperature to the austenite transition

temperature can be estimated. However, these times were not specifically recorded because tests were not allowed to be long enough to permit the phase transformation to austenite. These times can be qualitatively compared with testing durations.

In order to evaluate heat transfer equations, some assumptions need to made. For these experiments, the temperature rise was only 13°C (T_{aust} = 45°C, T_{rt} = 22°C). The rate of heat generation per cycle is assumed to be frequency independent at a constant value of 20 kJ/m^3, the maximum mechanical loss at the average bias stress of 1.5 MPa during shown in Figure 4.9. If soft-mode coupling is considered, the heat generation may be frequency dependent, though it cannot be quantified here. Eddy currents can also generate heat and will be assumed to follow equation 4.3. For the calculation, the heat generated is assumed be at the middle of the sample and conduct through half of the sample length (to the aluminum sample holders), $dx = 0.01$ m. The heat capacity, c, is about 430 J/kg·K (0.1 cal/g·K) [20] for Ni_2MnGa and the thermal conductivity, k, is about 15 W/m·K (typical range is 10–20 W/m·K) as typical of other Heusler alloys near stoichiometry [63]. It is assumed that once heat reaches the edge of the sample, aluminum sample holders can quickly conduct any amount of heat away. The aluminum sample holders are assumed to remain at room temperature throughout the test.

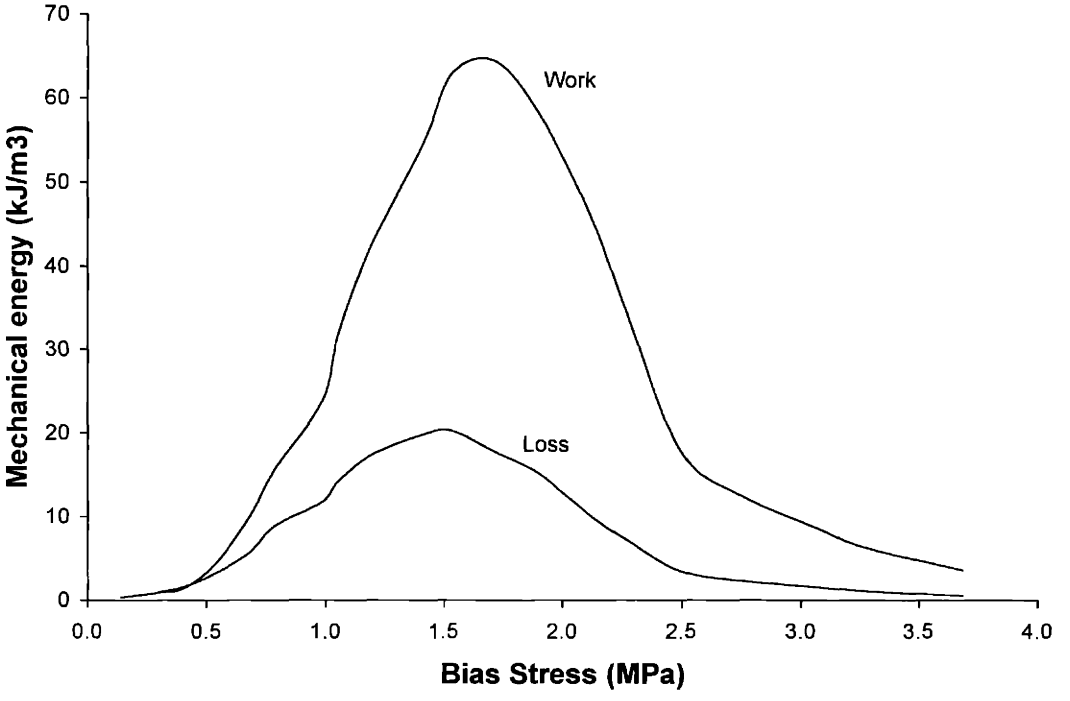

Figure 4.9: The steady-state mechanical work density and mechanical loss energy density as a function of the average bias stress. It is assumed that this work and loss is frequency independent and that other contributions add to frequency-depedendent loss.

According to the first law of thermodynamics, an energy balance must exist between the heat generated by dissipative mechanisms, the heat capacity of the sample and the thermal conduction to the aluminum sample holders at the ends of the sample. Thus the energy balance is:

$$\dot{Q} = V\rho c\left(\frac{dT}{dt}\right) + kA\left(\frac{dT}{dx}\right). \qquad 4.4$$

where $\dot{Q}$ is the heat generation rate, V is the volume, ρ is the density, A is the cross-sectional area. The solution to this first-order equation is:

$$T - T_n = \left(\dot{Q} / kA\right)\left(1 - e^{-t/\tau}\right) \qquad 4.5$$

where the time constant, τ, is expressed as:

$$\tau = V\rho c / kA. \qquad 4.6$$

For this sample, the time constant is calculated to be 0.9 hrs.

When $t \to \infty$, the maximum temperature rise in the sample becomes $\Delta T = \dot{Q} / kA$. For the steady-state, low-frequency energy loss at 1.5 MPa bias stress, the temperature rise becomes $\Delta T = 27°C$. When $t \to 0$, the initial rate of temperature rise is $dT / dt = \dot{Q} / V\rho c$. Under the same steady-state, low-frequency conditions, the rate of temperature rise is 8.23×10^{-3} °C/cycle per 20 kJ/m^3 energy loss. This value seems reasonable as Bozorth [58] reports that transformer iron heats 0.0003°C per 1 kJ/m^3 energy loss.

The time required to heat the sample to the transformation temperature can now be corroborated with observation. Figure 4.10 shows the heat generated as a function of the actuation frequency plus the steady-state energy loss on the left axis. The right axis shows the time required to heat the sample to the transformation temperature, given its heat capacity and assuming perfect conduction out of the aluminum sample holders. To compare this to observations, at the highest actuation frequency, 500 Hz, the time of the test was 1 second. During this time, the response dropped to about one-third of its initial value. Within 1 additional second of testing, the response would have dropped to zero.

An estimation of 2 seconds at 500 Hz is two times the value from Figure 4.10 to complete the transformation.

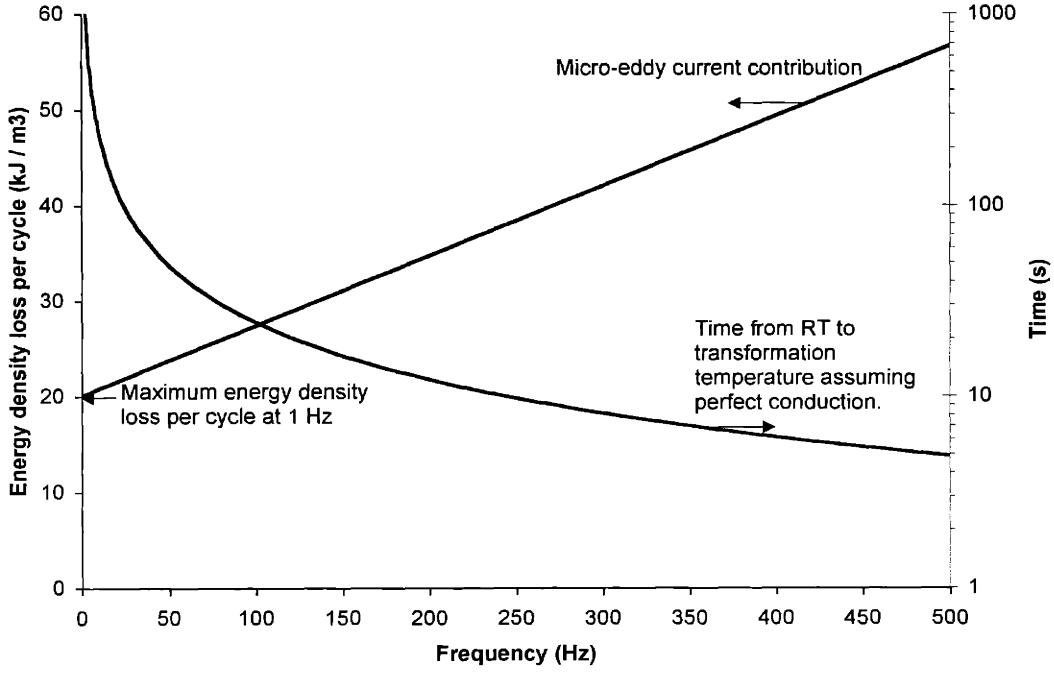

Figure 4.10: On the left axis, the steady-state mechanical energy loss at 1.5 MPa plus the linearly increasing micro-eddy current contribution. On the right axis, the solution in equation 4.5 is used to solve for the time given a temperature increase of $T_{aust} - T_{rt} = 13°C$.

Through short, high-speed measurements, the effects of eddy currents could be mitigated up to frequencies of 500 Hz. The effect of eddy currents should not be evident in Figure 3.15. For practical applications, these heating effects could be reduced through manufacture of laminations or particles. What seems to really limit the saturation strain at higher frequencies is the power supply and the electromagnet. See Appendix C for the issues regarding their performance. Though the performance limit of the hardware was

reached, the fundamental of limit dynamic MFIS actuation in Ni–Mn–Ga was not achieved and is being pursued by others. The resonance characteristics of Figure 3.15 can be predicted using response function theory modeled in a classical way by a forced damped harmonic oscillator.

4.2.4 FORCED DAMPED HARMONIC OSCILLATOR

Equation 4.7 is the standard forced, damped harmonic oscillator equation of motion, which is used to model kinematic motion.

$$m_{eff}\ddot{x} + \gamma_{eff}\dot{x} + k_{eff}x = F_0\cos(\omega t) \qquad 4.7$$

This general equation has four terms: inertial, damping, stiffness and a driving function. If the case of the DATS, the mass of the moving parts, the stiffness of the spring and forcing function are known. With this information, the damping coefficient can be determined. The effective, lumped system constants needed for equation 4.7 are given as:

$$m_{eff} = m_{sys} + m_{mat}$$
$$\gamma_{eff} = \gamma_{sys} + \gamma_{mat}$$
$$k_{eff} = k_{sys} + k_{mat}$$

where "*sys*" refers to the apparatus and "*mat*" refers to the material. Equation 4.7 models the forced harmonic oscillations of the entire system (sample plus the apparatus) and is not good for capturing the kinematic behavior of a material unless system parameters can be isolated from material parameters. If the system parameters are well known and

characterized, then the material specific parameters can be determined from the lumped parameters.

When determining the undamped natural frequency of the mass-spring system ($f_0 = 1/2\pi\sqrt{k_{sys}/m_{eff}}$), the properties of the system were measured as follows: m_{sys} = 26.75 g, and k_{sys} = 36,800 N/m produces f_0 = 165 Hz. This calculation corresponds well to the resonance and anti-resonance observed in the X4 DATS at this frequency. The mechanical quality factor, $Q_m = f_{nd}/(f_1 - f_2)$ = 2.26 is measured from Figure 3.15 directly. This corresponds to a critical damping ratio of $\xi = \gamma_{eff}/\gamma_c = \gamma_{eff}/2\sqrt{mk} = 0.2$ from which a damping coefficient of γ_{eff} = 12.4 can be calculated for this system, (sample and apparatus).

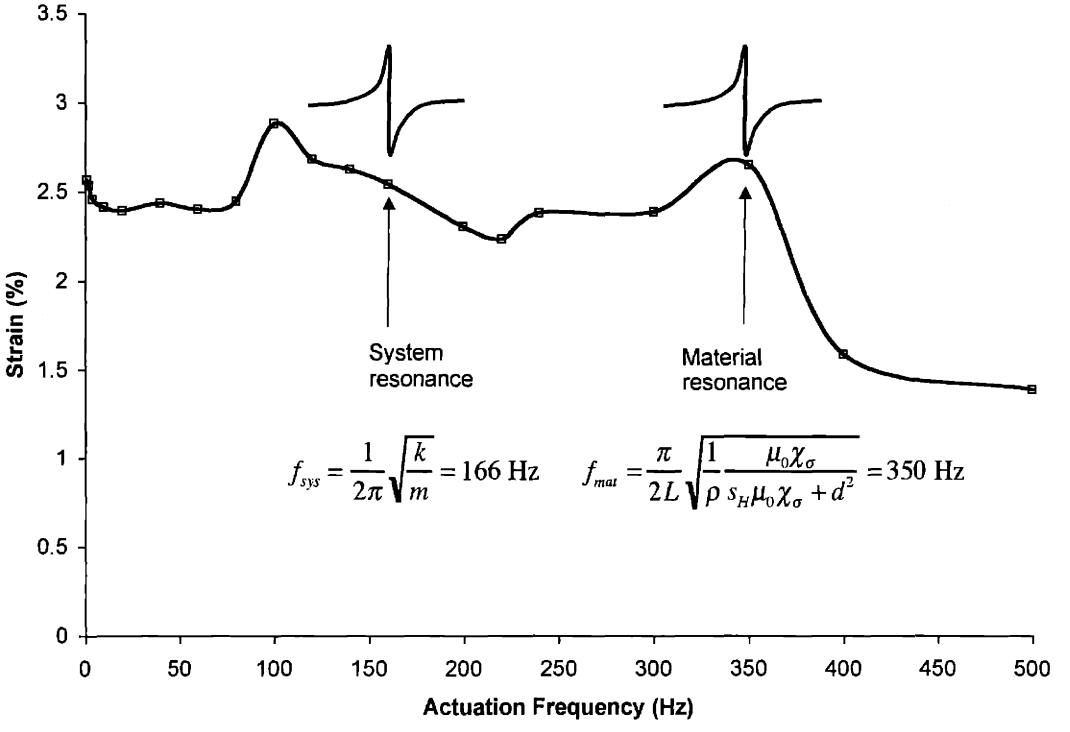

Figure 4.11: Saturation strain versus actuation frequency. The system resonance is calculated to be f_0 = 166 Hz with a mechanical quality factor, $Q = 2.26$ and a damping coefficient of $\gamma_{eff} = 12.4$.

The phase angle can be used to calculate the damping parameters for the magnetomechanical resonance at f_n =275 Hz. Using the equation for the phase angle, ϕ, the critical damping ratio, ξ, can be determined from rearranging the phase angle equation to be:

$$\xi = \frac{\omega_n}{2\omega}\left[1-(\omega/\omega_n)^2\right]\tan\phi. \qquad 4.8$$

A damping coefficient, $\gamma = 33$, and critical damping ratio, $\xi = 0.67$, are determined when the phase lag is fit as shown in Figure 4.12.

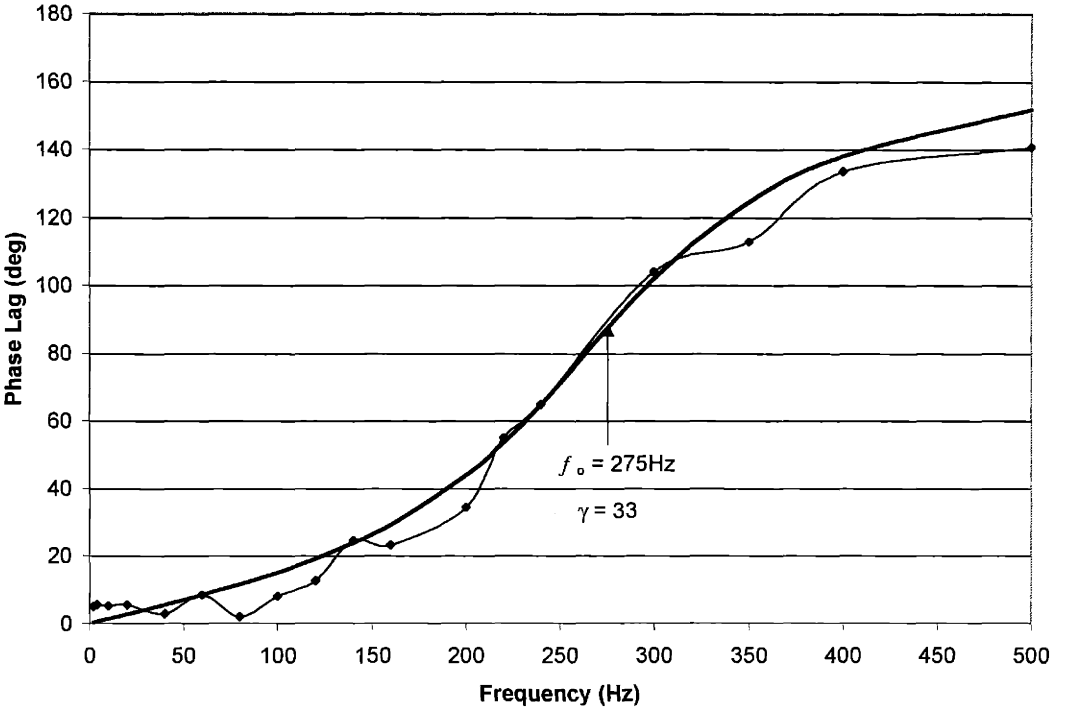

Figure 4.12: Phase lag versus actuation frequency for sample B at 1.7 MPa. A damping coefficient of 33 and damping ratio of 67% fits this frequency data well.

The second estimate using the phase angle to determine the resonant frequency is not only more reliable, but it gives a damping ratio that is useful for designers. When designing for good linearity, the frequency ratio (ω/ω_n) is kept within the range from 0%–40% [64]. This criterion is established to ensure the amplification ratio is unity, and that the phase shift is rather linear in this frequency range. With a damping ratio in the range of 65%–75%, the amplification ratio will be approximately unity over this frequency range. Furthermore, a linear phase shift with frequency may be important if a proper time relationship is to be kept between the multiple components of a complex

input and prevent signal distortion on the output. Thus, the characteristics of the damping, when evaluated with the phase information, give a damping ratio of 67% that is in the "sweet" spot" for linear transducer are sensor design.

4.2.5 RESPONSE FUNCTION THEORY

Response function theory was used by Mermelstein [65] for magnetoelastic materials and adapted by Pablo Tello. It utilizes the constitutive equations in equation A.49 to solve for the stress giving:

$$\sigma = \frac{-d}{(\chi_\sigma s_H - d^2)} M + \frac{\chi_\sigma}{(\chi_s s_H - d^2)} \varepsilon. \tag{4.9}$$

This result is substituted into the equation of motion:

$$\rho \frac{\partial^2 u}{\partial t^2} - \frac{\partial \sigma}{\partial y} = 0. \tag{4.10}$$

This results in the differential equation:

$$\rho \frac{\partial^2 u}{\partial t^2} + \frac{d}{(\chi_\sigma s_H + d^2)} \frac{\partial M}{\partial y} - \frac{\chi_\sigma}{(\chi_s s_H + d^2)} \frac{\partial \varepsilon}{\partial y} = \frac{\partial \sigma_{ap}}{\partial y}. \tag{4.11}$$

It can be shown that the solution of 4.11 is the complex response function, which relates the magnitude of the strain response to frequency through the materials constants.

$$G(\omega) = \frac{\omega_0^2}{C_M} \frac{\omega_0^2 - \omega^2}{\left(\omega_0^2 - \omega^2\right) + 4\gamma\omega^2} + i \frac{\omega_0^2}{C_M} \frac{2\gamma\omega^2}{\left(\omega_0^2 - \omega^2\right) + 4\gamma\omega^2} \tag{4.12}$$

where ω_0 is the resonant frequency given in terms of materials constants:

$$\omega_0 = \frac{\pi}{2L} \sqrt{\frac{1}{\rho} \frac{\mu_\sigma}{\mu_\sigma s^H + d^2}}. \tag{4.13}$$

Using the properties at a bias stress of 1.5 MPa: ρ= 8100 kg/m^3, $\mu_\sigma = 4\mu_0$, s_H = 5 10^{-7} (Pa)$^{-1}$, d = 1.2 × 10^{-7} m/A, and L = 0.014 m, gives f_0 = 275 Hz. This coincides with the previous natural frequency results from the phase data. However, this expression is sensitive to the value of the compliance, which can vary by three orders of magnitude, depending on whether twin boundaries are in motion or not.

A potential problem to this approach is the form of the constitutive equations: the model assumes linear dependence of the field variables on the dependent variables, which is clearly not the case as seen in Figure 3.2 and Figure 3.7. O'Handley's model gives reasonable form for the non-linear dependence of strain on field, so it may overcome some of the inherent linearity of the constitutive model. Another concern is the basis with which the equation of motion was derived: it is valid for small local deformation, which is not true in this case. This model, while elegantly providing the response function, is of very limited validity for FSMAs that create large deformations nonlinearly with an applied field. However, it does give the correct value for the material's resonant frequency.

4.2.6 FREQUENCY RESPONSE AND LOSS SUMMARY

Mechanisms to explain sample heating and frequency-dependent loss have been presented above. Phonon softening is a two-edged sword: the temperature and frequency conditions needed to take advantage of the possible lattice softening in the shear

directions are delicate, but energy absorption into the lattice may be efficient under these same conditions. Eddy currents appear to have a significant role in generating heat in the samples during actuation testing. Analytical calculations show that heating can dramatically reduce the length of time the FSMA remains martensitic at high frequencies. The fact that the time estimation, of 4 seconds at 500 Hz, is close to what is observed (2 seconds) leads one to think that the estimations of the energy losses and the assumption that all the mechanical loss goes into heating are not unreasonable. The use of published rather than measured values of the heat capacity and thermal conductivity for other Heusler alloys may be a source of error.

The continuum models presented—the forced, damped harmonic oscillator and the response-function theory—give estimates of the resonant and damping characteristics of the system (the sample and the apparatus). The resonant frequency was obtained when the phase data was applied to the harmonic oscillator equation for the phase lag. Response function theory corroborated the same resonant frequency, of 275 Hz, using material constants from Chapter 3. From the same phase data, a calculated damping ratio corresponded well to the optimum needed to design a linear actuator or sensor.

Chapter 5

5 EXTENSION OF FSMA PHENOMENOLOGICAL MODEL

Models are only as good as the assumptions upon which they were created. To make results possible or tractable, assumptions need be made that leave out or discount the complexity of the real system. One aspect that was not included explicitly in a model by O'Handley [49] is the stress generated in the FSMA in the presence of a magnetic field and bias stress. In Figure 3.7, the stress versus field data showed how the stress develops as the increasing field works on the FSMA against the spring, as the spring works on the FSMA against a decreasing field, and as the bias stress increases. Here the model by O'Handley is extended to include a phenomenological description of magnetization rotation and how it contributes to generating stress needed to initiate twin boundary motion.

To review O'Handley's model, a free energy expression, equation 5.1, is minimized to formulate constitutive relations relevant for twin-boundary motion.

$$\begin{aligned} g = f_1[-\mu_0 M_S H \sin\theta_1 - K_u \sin^2\theta_1 + e_0\sigma_{ext}] \\ +f_2[-\mu_0 M_S H \sin\theta_2 - K_u \sin^2\theta_2] \end{aligned} \qquad 5.1$$

where f_1 is the volume fraction of type 1 variants, $f_2 = 1 - f_1$ is the volume fraction of type 2 variants, θ_1 and θ_2 are the angles between the magnetic moment and the applied field in type 1 variants and type 2 variants respectively. All other symbols are either material constants or are particular to the sample geometry: $\mu_0 M_s = 0.6$ T is the

saturation magnetization, $K_u = 1.5 \times 10^5$ J/m^3 is the magnetocrystalline anisotropy energy, $e_0 = 1 - c/a = 0.06$ is defined by the shear across a twin boundary.

By differentiating the free energy expression in equation 5.1 and setting the result to zero, two relationships can be derived. The first relationship is for how θ_1 relates to the materials constants. The result is the definition of the reduced magnetic field, $h \equiv \sin\theta_1 = \mu_0 M_S H / 2K_u$. The second relationship is for how f_1 relates to the other variables and materials constants. The result is an expression for strain as a function of the field and applied stress resulting from twin boundary motion,

$$\varepsilon(\sigma, h) = \varepsilon_0 \delta f = 2K_u h(1 - h/2) - \sigma\varepsilon_0 / C\varepsilon_0 \qquad 5.2$$

where C is the effective stiffness in the twinning region of a stress vs. strain plot. For $\mu_0 M_S H < \sigma_{tby}\varepsilon$, no twin-boundary motion occurs and therefore no strain. The threshold field associated with the onset of twinning strain is $H_{th} = \sigma_{tby}\varepsilon / \mu_0 M_S$. Once strain initiates, it is linear in h until H approaches $2K_u / \mu_0 M_S$ where a negative term quadratic in H becomes appreciable up to $h = 1$. When the field starts to reverse, twin-boundary motion does not occur until $\sigma_{ext} > \mu_0 M_S H / \varepsilon_0$. Then the strain decreases back toward zero. As the bias stress is increased, the resultant strain is increasingly blocked as $\mu_0 M_S H < \sigma_{ext}\varepsilon$. If MFIS is to be consistent with observation, then it is necessary to establish a hierarchy of the relevant energy terms: $K_u > M_S H > \sigma_{ext}\varepsilon > \sigma_{tby}\varepsilon$.

5.1 Addition of Stress Dependence

The discussions in sections 3.2 and 4.1.4.1 illustrate that a magnetoelastic process could be responsible for generating the stress necessary to overcome the twin-boundary yield stress—the source of increasing field hysteresis. The phenomenological model resulting in equation 5.2 is expanded to incorporate magnetoelastic stress component and a bias stress component from a spring. This section shows how to include the magnetoelastic energy into the free energy expressions and solve for the stress as a function of the reduced field and the bias stress.

Figure 5.1 shows a schematic of the mechanical and magnetic system under consideration. In this arrangement, a magnetic field is applied transversely across the sample. Mechanical forces in the vertical load path are measured with a load cell. A spring in series with the sample provides a bias or restoring force. By changing the compression of the spring, with the variable y_0, the average bias stress can be set. The independent variables of the problem are the reduced field, h, and the external stress; the stress is a function of y_0 and h. The dependent variables in this model are the angles by which each magnetization deviates from the load axis, θ_1 and θ_2, the magnetoelastic strains in each variant ε_{1y}, and ε_{2y}, and the volume fraction of variant one, f_1 (volume fraction of variant 2 is $f_2 = 1 - f_1$).

Other constants in the model are given by the magnetoelastic coupling stress $B_1 = -\frac{3}{2}\lambda_{100}(c_{11} - c_{12})/2 = 10$ MPa, the uniaxial compressive modulus (non-twinning)

$E = (c_{11} - c_{12})/2 \approx 22 - 0.7$ GPa [20–66], the spring constants k = 12 kN/m or 36.8 kN/m (depending on the sample), the sample cross-section area a, the spring bias displacement y_0, and the sample length l.

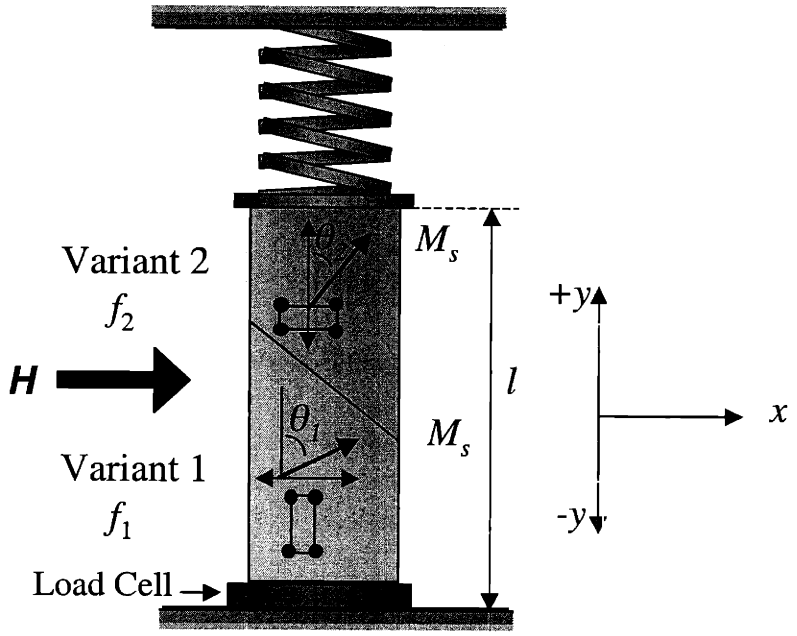

Figure 5.1: Sign and nomenclature conventions for dynamic actuation of a two variant FSMA. The dependent variables in this model are the angle that each magnetization deviates from the load axis, θ_1 and θ_2, magnetostrictive strains in each variant ε_{1y}, and ε_{2y}, and the volume fraction of variant one, f_1.

There are some important points to be made concerning this formulation. First, the externally applied stress favors the growth of variant 2 ($\delta f_1 < 0$) and is on the order of 1 to 2 MPa. However, the applied field for favors the growth of variant 1 ($\delta f_1 > 0$). The magnetostrictive strains are assumed to be of order 10^{-4} [24] and do not store energy in the spring. However, these magnetostrictive strains do store elastic energy within the

material. Twin-boundary strains are assumed not to store energy in the material, but rather store it by spring compression. The important contribution from magnetostriction is the stress that is developed within the sample when $\theta_2 > 0$. With the addition of magnetostrictive terms, one cannot simply drop energy density terms, such as B_1 or ε_{2y}, simply because they are smaller than others.

The free energy for the Zeeman, anisotropy, and elastic energy densities is divided into an expression for each variant in equations 5.3 and 5.4:

$$g_1 = f_1[-\mu_0 M_S H \sin\theta_1 - K_u \sin^2\theta_1 + e_0\sigma_{ext} + \tfrac{1}{2}E\varepsilon_{1y}^2], \qquad 5.3$$

$$g_2 = f_2[-\mu_0 M_S H \sin\theta_2 - K_u \sin^2\theta_2 + \tfrac{1}{2}E\varepsilon_{2y}^2], \qquad 5.4$$

where subscripts *1* and *2* represent variant 1 and variant 2 respectively, and σ_{ext} is given by:

$$\sigma_{ext}(h, y_0) = -\frac{k}{\mathrm{a}}\left[\frac{y_0}{l} + e_0 f_1(h, y_0)\right]. \qquad 5.5$$

5.2 Derivation of Magnetoelastic Energy Expressions

The magnetoelastic energy terms require more care and explanation. The proper treatment of magnetoelastic energy starts with the magnetoelastic anisotropy in cubic systems, which has the form:

$$g_{me} = B_1\left[\varepsilon_{xx}(\alpha_x^2 - \tfrac{1}{3}) + \varepsilon_{yy}(\alpha_y^2 - \tfrac{1}{3}) + \varepsilon_{zz}(\alpha_z^2 - \tfrac{1}{3})\right] \qquad 5.6$$

where ε_{ii} are the magnetostrictive strains and α_i are the magnetization direction cosines.

Because all the magnetoelastic energies are small ($B_1\varepsilon \approx 10^3 \text{J/m}^3$) compared to the magnetic anisotropy, the magnetization is confined to the x-y plane: $\alpha_x = \sin\theta$, $\alpha_y = \cos\theta = (1-\sin^2\theta)^{1/2}$, $\alpha_z = 0$. The magnetoelastic energy simplifies to:

$$g_{me} = B_1\left[\varepsilon_{xx}(\sin^2\theta - \tfrac{1}{3}) + \varepsilon_{yy}(1-\sin^2\theta - \tfrac{1}{3}) + \varepsilon_{zz}/3\right]. \qquad 5.7$$

Using the constant volume constraint, $\sum \varepsilon_{ii} = 0$, then the magnetoelastic energy in each variant becomes:

$$g_{me}^{i} = \frac{3}{2}\varepsilon_{iy}B_1\left[\sin^2\theta_i - 1\right]. \qquad 5.8$$

Because B1 is positive, this expression indicates that a positive magnetostrictive strain, ε_y, decreases the energy as H_x and therefore θ_i increases. This is the definition of negative magnetostriction. There is also a suppressing effect of the external stress on the formation of the magnetostrictive strains:

$$g_{me}^{i} = \frac{3}{2}\varepsilon_{iy}\sigma_{ext}\left[\sin^2\theta_i - 1\right]. \qquad 5.9$$

Large imposed stresses also generate a magnetoelastic anisotropy energy. These terms are generally small ($B_1\varepsilon \approx 10^3$ or $\sigma_{ext}\varepsilon_y \approx 10^2 \text{J/m}^3$) compared to the magnetocrystalline anisotropy. The largest terms of this type are the magnetoelastic terms that couple variant 2 to variant 1. When the magnetization rotates in variant 2, it exerts a compressive stress on variant 1 proportional to $-B_1\sin^2\theta_2$, which in turn causes a strain, ε_{1y}, in variant 1. Thus, the stress on variant 1 due to magnetostriction in variant 1 gives an energy density of the form:

$$g_1^{me} = -f_1 f_2 \varepsilon_{1y} B_1 \sin^2\theta_2 \left[\varepsilon_{xx}^1(\alpha_{1x}^2 - 1) + \varepsilon_{yy}^1(\alpha_{1y}^2 - 1) + \varepsilon_{zz}^1(\alpha_{1z}^2 - 1)\right]$$
$$= \frac{3}{2} f_1 f_2 \varepsilon_{1y} B_1 \sin^2\theta_2 \left[\sin^2\theta_1 - 1\right] \qquad 5.10$$

This indicates that as θ_2 increases, a positive magnetostrictive strain in variant 1 increases the energy.

5.3 TOTAL ENERGY DENSITY EXPRESSIONS

The total energy density expressions for each variant then sum to:

$$g_1 = f_1\{-\mu_0 M_S H \sin\theta_1 - K_u \sin^2\theta_1 + e_0\sigma_{ext}$$
$$-\tfrac{3}{2}\varepsilon_{1y}[B_1 \sin^2\theta_1(1 - f_2 \sin^2\theta_2) - \sigma_{ext}] + \tfrac{1}{2}E\varepsilon_{1y}^2\} \qquad 5.11$$

$$g_2 = f_2\{-\mu_0 M_S H \sin\theta_2 - K_u \sin^2\theta_2$$
$$-\tfrac{3}{2}\varepsilon_{2y}[B_1 \sin^2\theta_2(1 - f_1 \sin^2\theta_1) - \sigma_{ext}] + \tfrac{1}{2}E\varepsilon_{2y}^2\} \qquad 5.12$$

Using these energy densities, the direction of magnetization can be calculated by equating $dg / d\theta = 0$. The Zeeman and magnetocrystalline anisotropy energies dominate over the smaller torques caused by magnetostriction. Therefore, these terms are neglected when calculating the direction of M to be related to the reduced field, $h \equiv \sin\theta_2 = \mu_0 M_s H / 2K_u$ in variant 2. For variant 1, the solution reduces to $\theta_1 = 90°$ since $\sin\theta_1 = 1$ because physically M is already pointing in the direction of the field.

The total energy density expressions for each variant then simplify to:

$$g_1 = f_1\{-\mu_0 M_S H - K_u + e_0\sigma_{ext} - \tfrac{3}{2}\varepsilon_{1y}[(B_1 - \sigma_{ext})(1 - (1 - f_1)h^2)] + \tfrac{1}{2}E\varepsilon_{1y}^2\} \qquad 5.13$$

$$g_2 = (1 - f_1)\{-\mu_0 M_S H h - K_u h^2 - \tfrac{3}{2}\varepsilon_{2y}[(B_1 - \sigma_{ext})(1 - f_1)h^2] + \tfrac{1}{2}E\varepsilon_{2y}^2\}. \qquad 5.14$$

The magnetoelastic components in the brackets, [...], include the magnetoelastic stress that generates magnetostriction in the same variant, the energy due to ε_y in this variant, the magnetostrictive stress imposed from the other variant, and the stored energy due to ε_y from the external stress. The magnetostrictive strains are calculated by equating $\partial g / \partial \varepsilon_{1y} = 0$ and $\partial g / \partial \varepsilon_{2y} = 0$ to get the result:

$$\varepsilon_{1y} = \frac{3}{2}\frac{(B_1 - \sigma_{ext})(1-(1-f_1)h^2)}{E} \qquad 5.15$$

$$\varepsilon_{2y} = \frac{3}{2}\frac{(B_1 - \sigma_{ext})(1-f_1)h^2}{E}. \qquad 5.16$$

Care should be taken with these magnetostriction strains because the external stress is also a function of the reduced field, h, and the bias stress displacement, y_0. Now, to get the equilibrium expression for the volume fraction of variant 1 some negligible terms from the sum of 5.11 and 5.12 can be dropped and $\partial g / \partial f_1 = 0$ calculated. When the dropped elastic and magnetostriction terms are excluded from the calculation because they are ±1% of the other terms, the equilibrium volume fraction of variant 1 is:

$$f_1(h, y_0) = \frac{2K_u h(1-h/2)}{e_0^2 kl/a} - \frac{y_0}{e_0 l} \qquad 5.17$$

5.4 Stress Expression and Match to Stress versus Field Data

The final derivative is the stress that is generated by the combination of the magnetic torques, magnetostriction, bias stress, and elastic strains. The derivatives that

give the magnetostrictive strains plus the stress due to twin boundary motion define the stress generated in the material:

$$\begin{aligned}\sigma_y &= \frac{\partial g}{\partial \varepsilon_{2y}} + \sigma_{ext} = \sigma_{2y} + \sigma_{ext} \\ &= \tfrac{3}{2}[B_1(f_1 - h^2) - \sigma_{ext}(y_0, h)] + \sigma_{ext}(y_0, h)\end{aligned} \qquad 5.18$$

The independent variables are the reduced magnetic field H, and bias stress $\sigma_{ext}(y_0, h)$. The dependent variables are the orientations of the magnetization vectors in variant 2, θ_2, the magnetostrictive strains, ε_i, and the volume fraction f_1 ($f_2 = 1 - f_1$).

Magnetization rotation plays an important role in generating magnetostrictive stress in variant 2. This is illustrated with the H^2 quadratic rise in stress for the black curves of the model in Figure 5.2. Stress generated by straining against the spring overtakes the magnetostrictive stress at the coercive field. For intermediate stresses this transition is marked with a plateau, while for low or high average bias stresses, only a discontinuous slope marks the coercive field. In some cases the twinning strain saturates as the bias stress is too low or too high to permit significant reversibility of variant 1. However, at intermediate stresses, the twinning strain is high, enabling significant stress to develop in the spring and forcing compressive "reset" of variant 1 to variant 2. A good start toward validation of the model is made quantifying the stress vs. field relationships by collecting good data, then applying phenomenological principles to describe the field and bias stress dependence of the stress developed in the material.

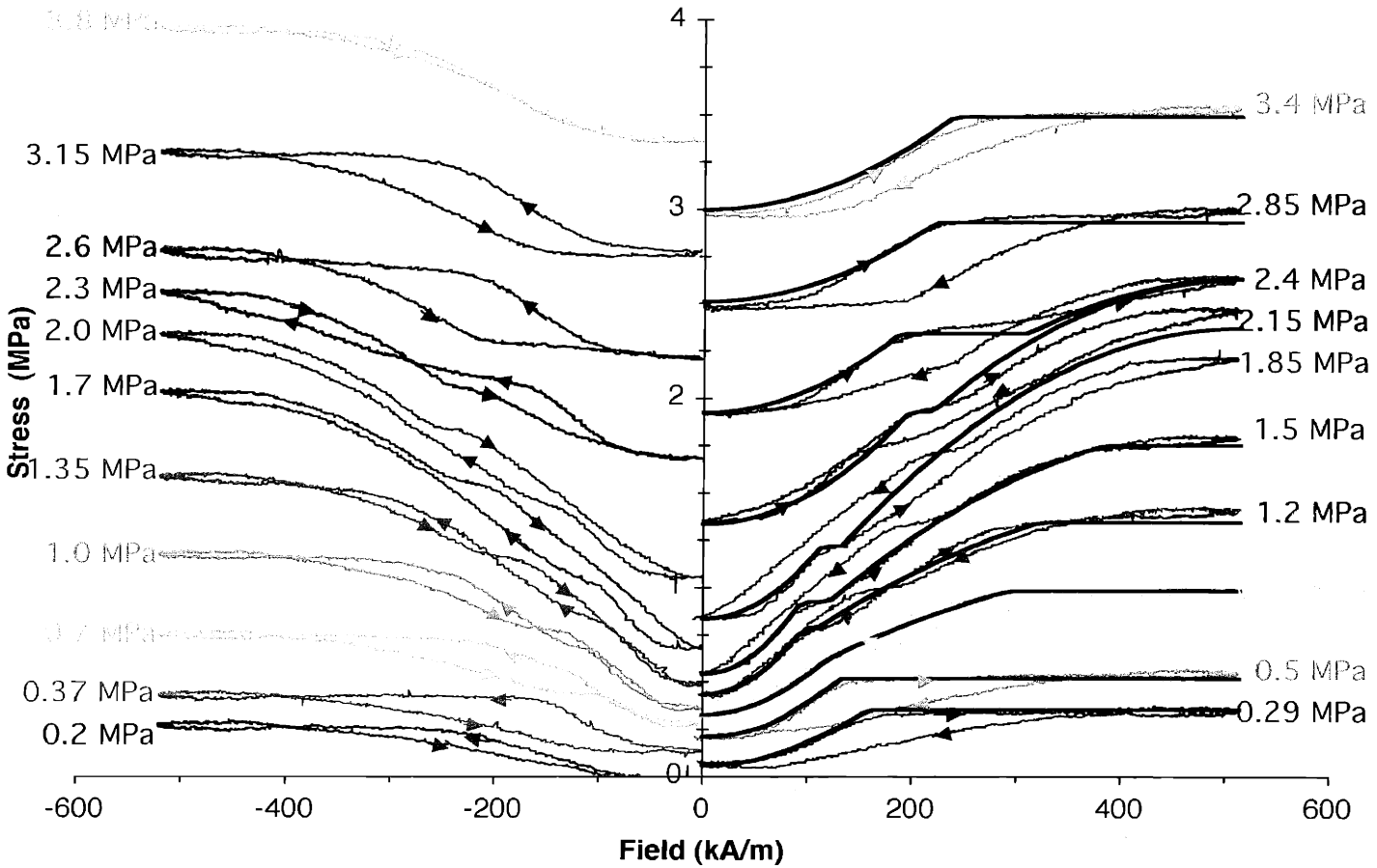

Figure 5.2:The results of equation 5.18 are plotted for half of the data set on from Figure 3.7. Different values of y_0 that correspond to the observed increasing field branches.

Chapter 6

6 CONCLUSIONS

- Hardware was designed and constructed to dynamically actuate Ni–Mn–Ga FMSAs and measure the bandwidth and unconstrained variables, MFIS, stress, and magnetization driven by a magnetic field.
- Dynamic measurements of MFIS indicate Ni–Mn–Ga can be actuated to cyclic strains of 3% and up to frequencies of *at least* 500 Hz.
- Though significant eddy current heating occurred, the primary frequency bandwidth limitation was the inductive reactance of the electromagnet and the power supply used to drive it.
- Harmonic oscillator models and modified response function theory account well for sample and measurement system resonant frequencies. Further, these models allow for loss tangent analysis that indicates Ni–Mn–Ga FSMAs are nearly optimized for damped linear actuators.
- Degradation of the dynamic MFIS actuation from 3.0% to 2.6% is observed with increasing number of cycles from $N \approx 1{,}000$ to $N \approx 100{,}000$.
- Measurement of unconstrained strain, stress, and magnetization driven by a magnetic field permitted the comparison of measured properties with properly defined thermodynamic properties.

- The peak thermodynamic piezomagnetic coefficient is $d_{31}|_{\sigma} = 2.5 \times 10^{-7}\,\mathrm{m/A}$ compared favorably to the measured slopes, $\partial\varepsilon/\partial H$, of 1.0 10^{-7} m / A at $N \approx 1{,}000$ cycles and 1.4×10^{-7} m / A at $N \approx 100{,}000$ cycles respectively.
- The thermodynamic piezomagnetic coefficient is five times greater than Terfenol-D with $d_{31} = 5.0 \times 10^{-8}\,\mathrm{m/A}$.
- Magnetic susceptibility varies between 3–10; and the twinning stiffness varies between 30–40 MPa within the average bias stress range of 0.3 to 2.8 MPa.
- With thermal analysis, close to the correct time to heat FSMAs to the transformation temperature is predicted.
- At optimum fields and bias stresses, the mechanical work density output during cyclic deformation was 65 kJ/m^3 per cycle with 20 kJ/m^3 lost per cycle.
- Actuation performance can be tailored by modifying the waveform of the applied field, *H(t)*.
- An important first observation of dynamic stress vs. field behavior is understood by an extension of a magnetomechanical phenomenological model.
- The mechanism of compressive stress generation in the sample before twin boundary motion has been shown to be magnetization rotation causing negative magnetostriction in type 2 variants with quadratic magnetic-field dependent stress on

type 1 variants ($\sigma \propto h^2$). Above the threshold for twin boundary motion, stress increases in proportion to the sample strain ($\sigma \propto 2K_u h(1-h/2)/\varepsilon_0$).

- The dynamic actuation measurements performed here help place Ni–Mn–Ga FSMAs into a regime of active materials performance between low bandwidth, high strain, high-energy density Nitinol and high bandwidth, low strain Terfenol-D and ferroelectrics.

6.1 FUTURE WORK

Studying single crystal FSMAs is a productive endeavor because there are still many aspects that are not yet known about this material. The following are avenues of research that may help reveal more about the basic nature of actuation in the FSMA and the many possible dependencies of properties.

- More dynamic MFIS actuation studies are needed to confirm, extend or differentiate the behavior observed in this thesis.
- The phenomenological model developed here should be further extended to predict the stress vs. strain behavior.
- The phenomenological model time-dependent relationships could be extended by using a kinetic model like the one by A. Soukhojak and Y. M. Chiang [67]. This may permit incorporation of time-dependent mechanisms into equilibrium phenomenological models.

- A processing route for Ni–Mn–Ga should be set to isolate sources of inconsistencies in material constants and sample properties.
- An in depth investigation could be pursued into the compositional variation of material constants and properties (such as in the static stress vs. strain plot in Figure 1.15).
- The role of mechanically training of samples on their actuation behavior could be readily investigated.
- The temperature sensitivity of material constants, MFIS and other sample properties could be measured. Check for any change in resonant frequency at different temperatures (as a consequence of phonon softening)
- MFIS fatigue, the possibility of a fatigue limit, and property degradation could be studied and attempts made to mitigate both through careful handling, processing, or alloying.
- Investigation into the possibility of a field-induced Bauschinger effect might aid the understanding of FSMAs.

Appendix A

A FREE ENERGY DERIVATION OF THERMODYNAMIC VARIABLES AND PROPERTIES

An common way to define material properties is to express the thermodynamic free energy as a Taylor series expansion of thermodynamic state variables. The internal energy of a system may be properly expressed as a function of extensive state variables where u_{en} is the internal energy density (per unit volume) as a function of the strain, ε, and the magnetization, M.

$$u_{en} = u_{en}(\varepsilon, M) \qquad \text{A.1}$$

The differential form of the first law of thermodynamics in three dimensions (i, j, k = 1, 2, or 3 in Einstein notation) becomes:

$$du_{en} = dq + \sigma_{ij} d\varepsilon_{ij} + \mu_0 H_k dM_k \qquad \text{A.2}$$

where q is heat into the material, σ_{ij} is the stress tensor, ε_{ij} is the strain tensor, H_k is the magnetic field vector, and M_k is the magnetization vector. Other thermodynamic state functions can be defined by Legendre transformation of the internal energy.

Gibbs free energy is a convenient thermodynamic function because its functional dependence is in experimentally-convenient intensive variables. The definition of Gibbs free energy, equation A.3, and in differential form, equation A.4, follow from the definition of the internal energy above:

$$g_{en} = g_{en}(\sigma, H) \equiv u_{en} - \sigma\varepsilon - HM \qquad \text{A.3}$$

$$dg_{en} = -\varepsilon_{ij} d\sigma_{ij} - \mu_0 M_k dH_k \qquad \text{A.4}$$

Here ε_{ij} is the strain, M_k is the magnetization and μ_0 is the permeability of free space. A differential change in these two energies can be expressed also in terms of a first-order Taylor series expansion of the internal energy, equation A.2 and the Gibbs free energy, equation A.4.

$$du_{en} = \left[\frac{\partial u_{en}}{\partial \varepsilon_{ij}}\right] d\varepsilon_{ij} + \mu_0 \left[\frac{\partial u_{en}}{\partial M_k}\right] dM_k \qquad \text{A.5}$$

$$dg_{en} = \left[\frac{\partial g_{en}}{\partial \sigma_{ij}}\right] d\sigma_{ij} + \mu_0 \left[\frac{\partial g_{en}}{\partial H_k}\right] dH_k \qquad \text{A.6}$$

Comparing the Taylor's expansion with the function definitions, the dependent variables can be defined as the derivative of the free energy with respect to an independent variable, while keeping the other independent variable constant in equations A.5 through A.6.

Internal $$\sigma_{ij} = \left[\frac{\partial u_{en}}{\partial \varepsilon_{ij}}\right], H_k = \left[\frac{\partial u_{en}}{\partial M_k}\right] \qquad \text{A.7–A.8}$$

Gibbs $$\varepsilon_{ij} = -\left[\frac{\partial g_{en}}{\partial \sigma_{ij}}\right], M_k = -\left[\frac{\partial g_{en}}{\partial H_k}\right] \qquad \text{A.9–A.10}$$

The variation of the newly defined dependent variables can again be expressed in terms of the independent variables by a first order Taylor's expansion of equations A.7 through A.10.

Internal

$$d\sigma_{ij} = \left[\frac{\partial \sigma_{ij}}{\partial \varepsilon_{kl}}\right]_M d\varepsilon_{kl} + \left[\frac{\partial \sigma_{ij}}{\partial M_k}\right]_\varepsilon dM_k \qquad \text{A.11}$$

$$dH_k = \left[\frac{\partial H_k}{\partial \varepsilon_{kl}}\right]_M d\varepsilon_{kl} + \left[\frac{\partial H_k}{\partial M_k}\right]_\varepsilon dM_k \qquad \text{A.12}$$

Gibbs

$$d\varepsilon_{ij} = \left[\frac{\partial \varepsilon_{ij}}{\partial \sigma_{kl}}\right]_H d\sigma_{kl} + \left[\frac{\partial \varepsilon_{ij}}{\partial H_k}\right]_\sigma dH_k \qquad \text{A.13}$$

$$dM_k = \left[\frac{\partial M_k}{\partial \sigma_{kl}}\right]_H d\sigma_{kl} + \left[\frac{\partial M_k}{\partial H_k}\right]_\sigma dH_k \qquad \text{A.14}$$

The first-order materials constants can be expressed as the first derivative with respect to the independent variables.

Internal

$$c^M_{ijkl} = \left[\frac{\partial \sigma_{ij}}{\partial \varepsilon_{kl}}\right]_M = \left[\frac{\partial^2 u_{en}}{\partial \varepsilon_{ij}\partial \varepsilon_{kl}}\right] \qquad \text{A.15}$$

$$b^M_{kij} = \left[\frac{\partial M_k}{\partial \varepsilon_{ij}}\right]_M = \left[\frac{\partial^2 u_{en}}{\partial M_k \partial \varepsilon_{ij}}\right] \qquad \text{A.17}$$

$$b^\varepsilon_{ijk} = \left[\frac{\partial \sigma_{ij}}{\partial M_k}\right]_\varepsilon = \left[\frac{\partial^2 u_{en}}{\partial \varepsilon_{ij}\partial M_k}\right] \qquad \text{A.19}$$

$$\left(\chi^{-1}\right)^\varepsilon_{kl} = \left[\frac{\partial H_k}{\partial M_l}\right]_\varepsilon = \left[\frac{\partial^2 u_{en}}{\partial M_k \partial M_l}\right] \qquad \text{A.21}$$

Gibbs

$$s^H_{ijkl} = \left[\frac{\partial \varepsilon_{ij}}{\partial \sigma_{kl}}\right]_H = -\left[\frac{\partial^2 g_{en}}{\partial \sigma_{ij}\partial \sigma_{kl}}\right] \qquad \text{A.16}$$

$$d^H_{kij} = \left[\frac{\partial M_k}{\partial \sigma_{ij}}\right]_H = -\left[\frac{\partial^2 g_{en}}{\partial H_k \partial \sigma_{ij}}\right] \qquad \text{A.18}$$

$$d^\sigma_{ijk} = \left[\frac{\partial \varepsilon_{ij}}{\partial H_k}\right]_\sigma = -\left[\frac{\partial^2 g_{en}}{\partial \sigma_{ij}\partial H_k}\right] \qquad \text{A.20}$$

$$\chi^\sigma_{kl} = \left[\frac{\partial M_k}{\partial H_l}\right]_\sigma = -\left[\frac{\partial^2 g_{en}}{\partial H_k \partial H_l}\right] \qquad \text{A.22}$$

The above properties for internal energy are stiffness at constant magnetization, c^M_{ijkl}, inverse converse piezomagnetic and inverse piezomagnetic constants, b^M_{kij} and b^ε_{ijk}, and the inverse magnetic susceptibility at constant strain, $\left(\chi^{-1}\right)^\varepsilon_{kl}$. The Gibbs free energy

properties are compliance at constant field, s^H_{ijkl}, converse piezomagnetic and piezomagnetic constants, d^H_{kij} and d^σ_{ijk}, and magnetic susceptibility at constant stress, χ^σ_{kl}. .

For the Gibbs energy expression, it is very difficult to set and maintain a known magnetization state and then measure the resulting stress vs. strain stiffness, c^M. As Callen and Callen point out there is no magnetic analog for "short-circuit" properties because there will always be magnetostatic "charge" on the surface. It is however, much easier to set and maintain a magnetic field within the material and measure the resulting stress vs. strain stiffness, c^H, as is reported in section 1.4, and then use the following conversions, A.27 or A.31.

Onsager's theorem shows that the coupled piezomagnetic properties are necessarily equal, resulting in Maxwell's relations, equations A.24 and A.26.

Internal $$\left[\frac{\partial H_k}{\partial \varepsilon_{ij}}\right]_M = \left[\frac{\partial \sigma_{ij}}{\partial M_k}\right]_\varepsilon \rightarrow \left[b^M_{kij}\right]^T = (b)^\varepsilon_{ijk} \qquad \text{A.23–A.24}$$

Gibbs $$\left[\frac{\partial M_k}{\partial \sigma_{ij}}\right]_H = \left[\frac{\partial \varepsilon_{ij}}{\partial H_k}\right]_\sigma \rightarrow \left[d^H_{kij}\right]^T = d^\sigma_{ijk} \qquad \text{A.25–A.26}$$

The other internal energy and Gibbs free energy properties can be related to each other in equations A.27 through A.34.

Internal

$$c^H = c^M - \frac{b^2}{(\mu_0 \chi^{-1})^\varepsilon} \qquad \text{A.27}$$

Gibbs

$$s^M = s^H - \frac{d^2}{\mu_0 \chi^\sigma} \qquad \text{A.28}$$

$$(\chi^{-1})^{\sigma} = (\chi^{-1})^{\varepsilon} - \mu_0 b^2 s^M \qquad \text{A.29} \qquad \chi^{\varepsilon} = \chi^{\sigma} - d^2 c^H / \mu_0 \qquad \text{A.30}$$

$$k^2 = b^2 / (c^M \mu_0 (\chi^{-1})^{\varepsilon}) \qquad \text{A.31} \qquad k^2 = d^2 / (s^H \mu_0 \chi^{\sigma}) \qquad \text{A.32}$$

$$\frac{c^H}{c^M} = (1 - k^2) \qquad \text{A.33} \qquad \frac{s^M}{s^H} = (1 - k^2) \qquad \text{A.34}$$

$$\frac{(\chi^{-1})^{\sigma}}{(\chi^{-1})^{\varepsilon}} = (1 - k^2) \qquad \text{A.35} \qquad \frac{\chi^{\varepsilon}}{\chi^{\sigma}} = (1 - k^2) \qquad \text{A.36}$$

where

$$c^H = \frac{1}{s^H}, \quad s^M = \frac{1}{c^M} \qquad \text{A.37, A.38}$$

$$\left(\chi^{-1}\right)^{\sigma} = \frac{1}{\chi^{\sigma}}, \quad \left(\chi^{-1}\right)^{\varepsilon} = \frac{1}{\chi^{\varepsilon}} \qquad \text{A.39, A.40}$$

$$d = s^H \chi^{\varepsilon} b, \quad \chi^{\sigma} / \chi^{\varepsilon} = s^H / s^M. \qquad \text{A.41, A.42}$$

The magnetomechanical coupling coefficient, k, is defined above in A.31 and A.32. It is an important performance measure for active materials and is used by designers. Second variations of the energy densities in the Taylor's series expansion are functions only of the independent variables and the properties defined in A.15 through A.22:

Internal $$d^2 u_{en} = \tfrac{1}{2} c^M_{ijkl} \partial\varepsilon_{ij} \partial\varepsilon_{kl} + b_{kij} \partial M_k \partial\varepsilon_{ij} + \tfrac{1}{2} \mu_0 \left(\chi^{-1}\right)^{\varepsilon}_{kl} \partial M_k \partial M_l \qquad \text{A.43}$$

Gibbs $$d^2 g_{en} = -\tfrac{1}{2} s^H_{ijkl} \partial\sigma_{ij} \partial\sigma_{kl} - d_{kij} \partial H_k \partial\sigma_{ij} - \tfrac{1}{2} \mu_0 \chi^{\sigma}_{kl} \partial H_k \partial H_l \qquad \text{A.44}$$

The constitutive equations for these energy formulations become:

Internal $$\sigma_{ij} = c^M_{ijkl} \varepsilon_{kl} + b^{\varepsilon}_{kij} M_k \qquad \text{A.45}$$

$$H_k = b^M_{ijk} \varepsilon_{ij} + \left(\chi^{-1}\right)^{\varepsilon}_{kl} M_l \qquad \text{A.46}$$

Gibbs $$\varepsilon_{ij} = s^H_{ijkl} \sigma_{kl} - d^{\sigma}_{kij} H_k \qquad \text{A.47}$$

$$M_k = -d^{\sigma}_{ijk}\sigma_{ij} + \chi^{\sigma}_{kl}H_l, \qquad \text{A.48}$$

The constitutive relationships in matrix form are equation A.49 for the internal energy expression and equation A.50 for the Gibbs energy expression.

Internal
$$\begin{bmatrix}\sigma\\ \mathbf{H}\end{bmatrix} = \begin{bmatrix}\mathbf{c}^{M} & b\\ b^{T} & \left(\chi^{-1}\right)^{\varepsilon}\end{bmatrix}\begin{bmatrix}\varepsilon\\ \mathbf{M}\end{bmatrix} \qquad \text{A.49}$$

Gibbs
$$\begin{bmatrix}\varepsilon\\ \mathbf{M}\end{bmatrix} = \begin{bmatrix}\mathbf{s}^{H} & -\mathbf{d}\\ -\mathbf{d}^{T} & \chi^{\sigma}\end{bmatrix}\begin{bmatrix}\sigma\\ \mathbf{H}\end{bmatrix}. \qquad \text{A.50}$$

These macroscopic properties (or constants) of crystals are tensorial in nature. These properties are tied to the specific crystal structure of the material. Nevertheless, a crystal's properties must remain invariant under the point group symmetry operations of the crystal. In determining constitutive relationships to use one usually tries to pick forms that attach a physical meaning to a phenomenological behavior. In the case of Ni–Mn–Ga, the traditional physical mechanism of MFIS via twin boundary motion is not associated with the piezomagnetic constant. The use of the piezomagnetic constant is to relate it to other active materials. In the case of $I4/mmm$ symmetry, no piezomagnetic constant is allowed for a single variant, single crystal in the full set of constitutive relations in equation A.51. Since other tetragonal and orthorhombic symmetries permit piezomagnetic constants, the slope of the MFIS via twin boundary motion would possibly need to be characterized by another constant.

$$\begin{bmatrix} \varepsilon_1 \\ \varepsilon_2 \\ \varepsilon_3 \\ \varepsilon_4 \\ \varepsilon_5 \\ \varepsilon_6 \\ M_1 \\ M_2 \\ M_3 \end{bmatrix} = \begin{bmatrix} s_{11}^H & s_{12}^H & s_{13}^H & \cdot & \cdot & \cdot & \cdot & \cdot & \cdot \\ s_{12}^H & s_{11}^H & s_{13}^H & \cdot & \cdot & \cdot & \cdot & \cdot & \cdot \\ s_{13}^H & s_{13}^H & s_{33}^H & \cdot & \cdot & \cdot & \cdot & \cdot & \cdot \\ \cdot & \cdot & \cdot & s_{55}^H & \cdot & \cdot & \cdot & \cdot & \cdot \\ \cdot & \cdot & \cdot & \cdot & s_{55}^H & \cdot & \cdot & \cdot & \cdot \\ \cdot & \cdot & \cdot & \cdot & \cdot & s_{66}^H & \cdot & \cdot & \cdot \\ \cdot & \cdot & \cdot & \cdot & \cdot & \cdot & \chi_1^\sigma & \cdot & \cdot \\ \cdot & \cdot & \cdot & \cdot & \cdot & \cdot & \cdot & \chi_1^\sigma & \cdot \\ \cdot & \cdot & \cdot & \cdot & \cdot & \cdot & \cdot & \cdot & \chi_3^\sigma \end{bmatrix} \begin{bmatrix} \sigma_1 \\ \sigma_2 \\ \sigma_3 \\ \sigma_4 \\ \sigma_5 \\ \sigma_6 \\ H_1 \\ H_2 \\ H_3 \end{bmatrix} \qquad \text{A.51}$$

However, in a single crystal consisting of two variants (type 1 and 2 for example), $I4/mmm$ symmetry is broken. The proportions of variant orientations and the average variant size govern the effective, macroscopic symmetry of the crystal. In this case, the limiting symmetry of the crystal may be of the twin boundary itself: a mirror operation. Mirror operations (as a monoclinic symmetry) permit the existence of piezomagnetic properties. This study evaluates experiment variables as a subset of A.51 and focuses on an effective piezomagnetic coefficient, d_{31} in the constitutive equation:

$$\begin{bmatrix} \varepsilon_1 \\ M_2 \end{bmatrix} = \begin{bmatrix} S_{11}^H & -d_{31} \\ -d_{31} & \chi_1^\sigma \end{bmatrix} \begin{bmatrix} \sigma_1 \\ H_2 \end{bmatrix}. \qquad \text{A.52}$$

To this point, only linear differential state equations have been derived. Some of the most important characteristics of SMAs (e.g. their hysteresis loops) and conventional magnetostrictors are fundamentally quadratic and hence require extension of the theory of higher orders. In principle, there is no difficulty in extending the energy definitions of A.2 or A.4 to arbitrarily high orders to define non-linear compliances. The practical

difficulty concerns the increasingly high order of the tensorial nature of these non-linear formulations. It is generally prohibitively difficult to continue in a fully consistent way to higher orders, and in practice physical insight is nearly always used to single out the most significant non-linearities in the particular context. In Chapter 5, the phenomenological model attempts to single out the significant stress-dependencies presented in Chapter 3.

As derived above the Gibbs energy expression correctly describes the dependent and indent convenient properties than the internal energy

Appendix B

B HYSTERESIS LOSS: DERIVATION AND MECHANISMS

Hysteresis is used as a generic term indicating a process that has a bi-valued state for the dependent variable on a closed loop. In some applications, hysteresis is an asset; but in most applications, hysteresis is detrimental. Hysteresis loss is usually a problem for actuation applications it can degrade the material's performance and the active material can build up heat each cycle. Active materials with low hysteresis losses and correspondingly high quality factors can have an amplified strain response at resonance. However, hysteresis loss can be an asset because low mechanical quality factors allow for a broader bandwidth with which to receive signals (either as a sensor or dampener).

Factors contributing to hysteretic loss are composition inhomogeneities, impurities, temperature and stress. One microscopic consequence of these factors is they create energy barriers preventing the movement local quasi-equilibrium boundaries (such as grain boundaries, domain walls and twin boundaries). When an intensive field is applied an energy difference is created across the boundary; energy builds up in the region (to overcome the boundary energy barrier) prior to the movement of the quasi-equilibrium boundaries and then the energy is dissipated as the boundary moves to a new quasi-equilibrium position.

This appendix derives the relationships between hysteresis loss, thermodynamic properties and experimental data found in Chapter 3 by starting with the thermodynamic constitutive equation, A.52. The derivation of these relationships is not limited to specific energy sources and its first-order coupling, so it is analogous to the piezoelectric treatment by Uchino and Hirose [68].

B.1 RELATION BETWEEN HYSTERESIS AND LOSS TANGENT

When hysteresis is not very large and there is no magnetomechanical coupling, the time dependence of the magnetization, M, can be expressed by using a phase lag relative to the applied magnetic field, H as shown in Figure B.1 (a). Assuming that the magnetic field oscillates at frequency $f = \omega / 2\pi$ as:

$$H = H_0 e^{i\omega t} \tag{B.1}$$

The magnetization also oscillates at the same frequency but with a phase delay, δ':

$$M = M_0 e^{i(\omega t - \delta')}. \tag{B.2}$$

If the relation between M and H is expressed as:

$$M = \mu_0 \chi^* H \tag{B.3}$$

then the complex magnetic susceptibility constant, χ^*, is:

$$\chi^* = \chi' - i\chi'' \tag{B.4}$$

and where

$$\frac{\chi''}{\chi'} = \tan\delta'. \tag{B.5}$$

This formulation of the loss tangent is based upon the observation that the magnetization lags the applied magnetic field. However, a proper expression of the energy lost in the material should come from variation of extensive variables, magnetization and displacement. By transposing the axes in Figure B.1 (a) a *gedenken* experiment can be carried out: by applying a magnetization, a phase lag δ, exists for the magnetic field. Rewriting B.1 through B.5 the proper definition of the loss tangent is obtained for energy lost in the material.

$$M = M_0 e^{i\omega t} \tag{B.6}$$

The magnetization also oscillates at the same frequency but with a phase delay, δ':

$$H = H_0 e^{i(\omega t - \delta)}. \tag{B.7}$$

If the relation between M and H is expressed as:

$$H = (\mu_0 \chi^*)^{-1} M \tag{B.8}$$

then the complex, inverse magnetic-susceptibility constant, χ^*, is:

$$(\chi^*)^{-1} = (\chi')^{-1} - i(\chi'')^{-1} \tag{B.9}$$

and where

$$\frac{(\chi^{-1})''}{(\chi^{-1})'} = \frac{\chi'}{\chi''} = \tan\delta. \tag{B.10}$$

It should be noticed that the negative relationship in B.9 comes from the time delay and the fact that $(\mu_0 \chi'')^{-1} = (H_0 / M_0)\cos\delta$ and $(\mu_0 \chi')^{-1} = (H_0 / M_0)\sin\delta$.

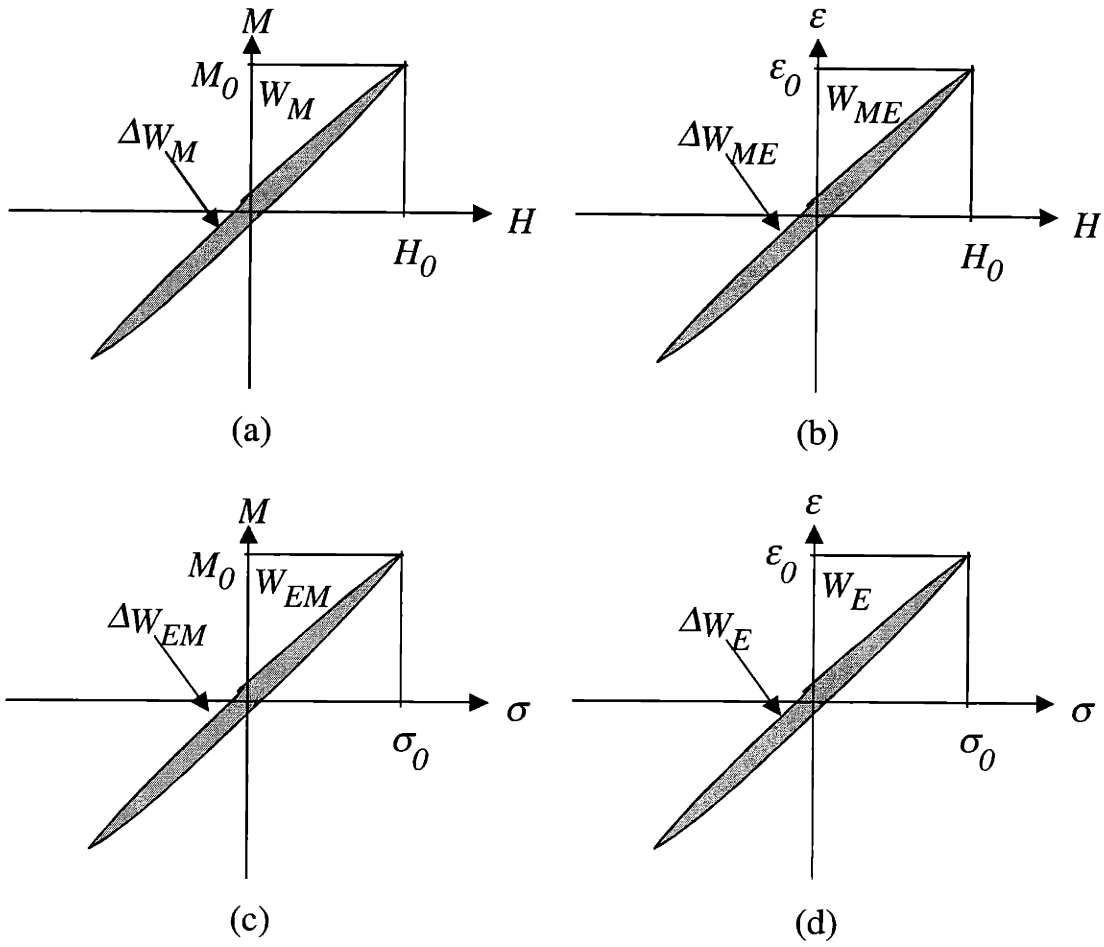

Figure B.1: Weak-field constitutive behavior that follows Gibbs formulation in A.49 with a small amount of hysteresis loss. (a) M vs. H (at $\sigma = 0$), (b) ε vs. H (at $\sigma = 0$), (c) M vs. σ (at H = const.), (d) ε vs. σ (at H = const.). ΔW is the hysteresis loss per cycle and W is the energy stored in the material.

The area ΔW_M in Figure B.1 corresponds to the energy lost in a magnetization cycle and can be related to the isotopic magnetic susceptibility χ'' and $\tan\delta$ as follows:

$$\Delta W_M = -\int H dM = -\int_0^{2\pi/\omega} H(dM/dt)dt = \pi M_0 H_0 \sin\delta$$
$$= \frac{\pi M_0^2}{\mu_0 \chi''} = \frac{\pi M_0^2}{\mu_0 \chi''} \tan\delta \qquad \text{B.11}$$

When there is no phase delay ($\delta = 0$, $\Delta W_M = 0$), the magnetic energy stored in the material will be recovered completely after a full cycle resulting in 100% efficiency. However, when there is a phase delay, a loss ΔW_M, will accompany it and the magnetic material generates heat. Therefore, $\tan\delta$ is called the magnetic loss tangent. When considering the stored magnetic energy during a half cycle from M_0 to -M_0 is equal to:

$$4W_M = (1/2)(2M_0)\left(\frac{2M_0}{\mu_0 \chi'}\right) = \frac{2M_0^2}{\mu_0 \chi'}, \qquad \text{B.12}$$

the loss tangent $\tan\delta$ can be found experimentally:

$$\tan\delta = \frac{1}{2\pi}\frac{\Delta W_M}{W_M} \qquad \text{B.13}$$

The extensive complex susceptibility, elastic, and piezomagnetic properties are written from the internal energy formulation of the constitutive equations in Appendix A as complex properties, c^{M*} and b^* along with $(\chi^{-1})^{\varepsilon*}$:

$$(\chi^{-1})^{\varepsilon*} = (\chi^{-1})^{\varepsilon}(1 + i\tan\delta) \qquad \text{B.14}$$

$$c^{M*} = c^M(1 + i\tan\phi) \qquad \text{B.15}$$

$$b^* = b(1 + i\tan\theta) \qquad \text{B.16}$$

which can be rewritten as phase lags with equations A.38 and A.40 into Gibbs properties:

$$\chi^{\varepsilon*} = \chi^{\varepsilon}(1 - i\tan\delta) \qquad \text{B.17}$$

$$s^{M*} = s^M(1 - i\tan\phi), \qquad \text{B.18}$$

$$d^* = d(1 - i\tan\theta) \qquad \text{B.19}$$

where ϕ is the phase lag of the stress with respect to an "applied strain" and θ is the phase lag of the magnetic field under an "applied strain" (which should also be the same as the phase lag of the stress under an "applied magnetization"). These phase lags are considered to be "extensive" loss contributions in the material.

The stored elastic energy and hysteresis loss can be calculated in an analogous way to B.11 and B.12, which are presented in their final forms here:

$$W_E = \tfrac{1}{2} c^M \varepsilon_0^2 \qquad \text{B.20}$$

$$\Delta W_{El} = \pi c^M \varepsilon_0^2 \tan\phi \qquad \text{B.21}$$

B.2 MAGNETOMECHANICAL HYSTERESIS AND LOSS TANGENT

The magnetomechanical loss is less straightforward, using the *gedenken* experiment, with the induced magnetic field as a result of an applied strain. The stored energy, W_{ME}, during a quarter of the strain cycle is:

$$\begin{aligned} W_{ME} &= -\int \sigma d\varepsilon = (1/2)(\sigma_0^2 / c^M) = (1/2)(\mathbf{b}M_0)^2 / c^M \\ &= (1/2)(\mathbf{b}^2 / c^M) M_0^2 \end{aligned} \qquad \text{B.22}$$

$$\Delta W_{ME} = \pi(\mathbf{b}^2 / c^M) M_0^2 (2\tan\theta - \tan\phi) \qquad \text{B.23}$$

If the losses are small in comparison the total energy, the B.22 and B23 may be estimated from experimental parameters:

$$\begin{aligned} 1 - W_{ME} &\approx -\int \varepsilon d\sigma = (1/2)(\varepsilon_0^2 / s^H) = (1/2)(\mathbf{d}H_0)^2 / s^H \\ &= (1/2)(\mathbf{d}^2 / s^H) H_0^2 \end{aligned} \qquad \text{B.24}$$

$$1 - \Delta W_{ME} \approx \pi(\mathbf{d}^2 / s^H) H_0^2 (2\tan\theta' - \tan\phi'). \qquad \text{B.25}$$

The strain versus magnetic field measurement provides the piezomagnetic loss $\tan\theta$ directly. Similar sets of stored energy and hysteresis loss for induced magnetization under a stress can be calculated during a quarter and a full stress cycle.

$$W_{EM} = (1/2)(\mu_0 \chi^{\varepsilon} \mathbf{b}^2)\varepsilon_0^2 \qquad \text{B.26}$$

$$\Delta W_{EM} = \pi(\mu_0 \chi^{\varepsilon} \mathbf{b}^2)\varepsilon_0^2(2\tan\theta - \tan\delta) \qquad \text{B.27}$$

so that:

$$\tan\theta = \frac{1}{2}\left[\frac{1}{2\pi}\frac{W_{EM}}{\Delta W_{EM}} + \tan\phi\right] \qquad \text{B.28}$$

From the measurements of M vs. H and ε vs. σ, $\tan\delta$ and $\tan\phi$ can be obtained experimentally. With either the piezomagnetic (M vs. σ) or the converse piezomagnetic (ε vs. H) provide $\tan\theta$ by numerical subtraction.

$$\tan\theta = \tan\phi - \tan\delta. \qquad \text{B.29}$$

In the case of loss tangent results for sample A in chapter 4, the magnetic loss tangent can be calculated by:

$$\tan\delta = \tan\phi - \tan\theta. \qquad \text{B.30}$$

B.3 PROPERTY RELATIONSHIPS

In order to relate the intensive losses to the extensive losses, the following equations can be obtained by manipulating some of the property expressions in A.27 through A.42:

$$\mu_0 \chi^{\sigma} = [\mu_0^{-1}(\chi^{-1})^{\varepsilon}(1 - b^2/(c^M \mu_0^{-1}(\chi^{-1})^{\varepsilon})]^{-1} \qquad \text{B.31}$$

$$s^H = [c^M(1 - b^2/(c^M \mu_0^{-1}(\chi^{-1})^{\varepsilon})]^{-1} \qquad \text{B.32}$$

$$d = [b^2 / (c^M \mu_0^{-1} (\chi^{-1})^{\epsilon})][b(1 - b^2 / (c^M \mu_0^{-1} (\chi^{-1})^{\epsilon})]^{-1} \quad \text{B.33}$$

By substituting B.9–B11 and B.19–B22 into B.25–B.27, the relationship between intensive and extensive losses is obtained in the following equations:

$$\tan\delta' = (1/(1-k^2))[\tan\delta + k^2(\tan\phi - 2\tan\theta)], \quad \text{B.34}$$

$$\tan\phi' = (1/(1-k^2))[\tan\phi + k^2(\tan\delta - 2\tan\theta)], \quad \text{B.35}$$

$$\tan\theta' = (1/(1-k^2))[\tan\delta + \tan\phi - (1+k^2)\tan\theta]. \quad \text{B.36}$$

So the intensive magnetic and elastic losses are mutually correlated with the extensive magnetic, elastic, and piezomagnetic losses through the magnetomechanical coupling, k^2 (defined in Appendix A). The mechanical quality factor is simply the inverse of the intensive mechanical loss tangent.

B.4 QUALITY FACTORS

Quality factor is related to the sharpness of the resonance and the resonance width directly in Figure B.2:

$$Q_m = \frac{f_{nd}}{f_2 - f_1} \text{ or } Q_m = (\tan\phi')^{-1} \quad \text{B.37}$$

where f_{nd} is the damped natural frequency, and $f_2 - f_1$ is the resonance width at 3 dB (0.707) of the maximum value. Or, it is equal to the intensive mechanical loss tangent as derived by Uchino and Hirose [68]. Lower intensive mechanical loss tangents give greater mechanical quality factors. The relations between the quality factor, Q, the critical damping ratio, ξ, and the natural damped frequency, ω_{nd}, are given in Table B.1. The

relationships of the critical damped ratio to the amplification ratio of the response to equation 4.7 can be seen in Figure B.2. The associated phase lag for the response is given for different critical damped ratios in Figure B.3.

Table B.1: Values of critical damping ratio, quality factor, and natural damped frequency.

Critical damping ratio, ξ	Quality factor, Q	Damped resonance freq., ω_{nd} / ω_n
0	∞	1
0.2	2.33	0.95
0.3	1.36	0.9
0.4	1.	0.85
0.5	1.154	0.69
0.707	1	0.16
1.0	1	0.005

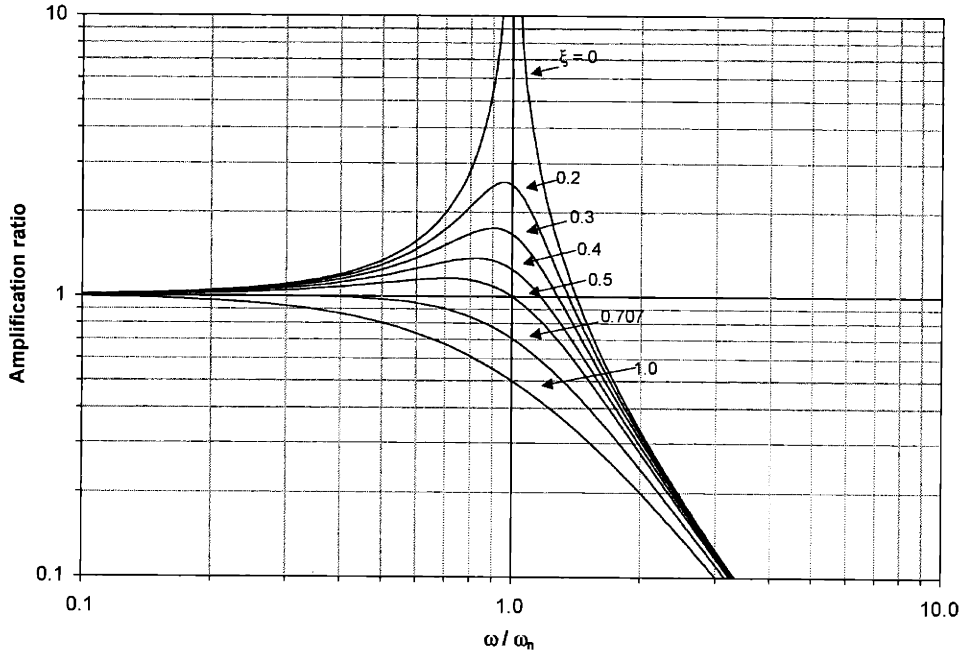

Figure B.2: Amplification ratio versus normalized frequency for different critical damping ratios, where $\xi = \gamma / \gamma_c = \gamma / 2\sqrt{mk}$. The quality factor,

Q, is simply the maximum amplification ratio on a given curve. The damped natural frequency is shifted to a lower frequency that corresponds with Q.

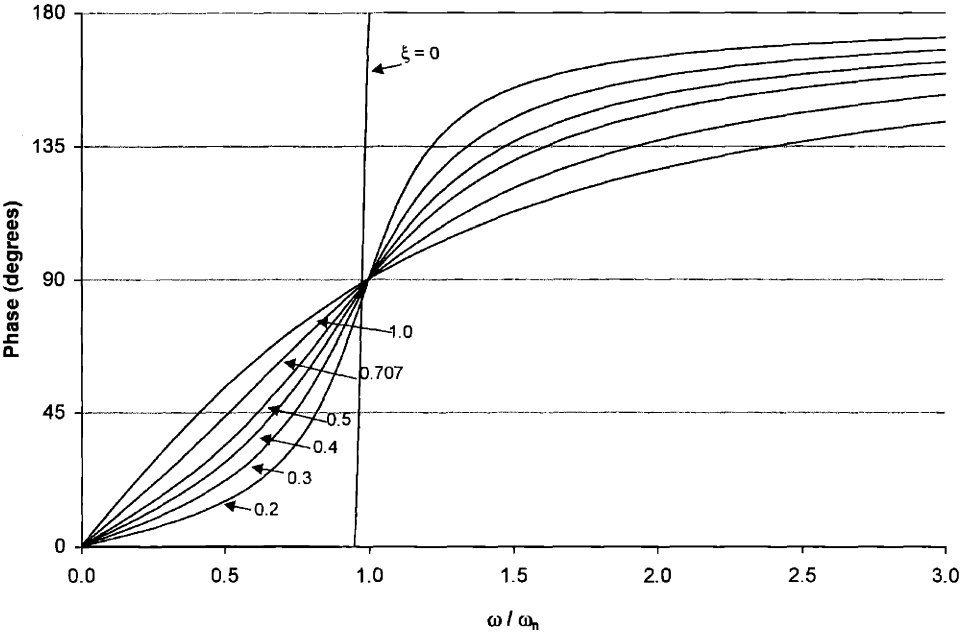

Figure B.3: Phase angle versus frequency ratio for different critical damping ratios.

Appendix C

C ELECTROMAGNET DESIGN

Appendix C reviews the efforts made to improve the electromagnets used in the AC actuation experimental apparatus. The purpose of the electromagnet revisions is to increase the frequency bandwidth while preserving a maximum magnetic field of 6 kOe. One electromagnet (X1) was borrowed and three were handmade (X2, X3, X4). Specifications for these electromagnets are given in Table C.1. The current versus field characteristics for all four lab-made electromagnet revisions X1 through X4 are shown in Figure C.1. Each electromagnet design had a successively lower DC resistance and lower inductance, which resulted in an electromagnet that could generate sufficient fields up to frequencies of interest. A rendering of the final X4 electromagnet is in Figure C.2. The following discusses some of the tradeoffs that were considered when designing the electromagnet for this project.

Table C.1: Specifications of electromagnet revisions.

	X1	X2	X3	X4
Wire gage (AWG)	18	15	12	10
Turns per coil	1000	750	214	140
Resistance in parallel	4.4 Ω	2.2 Ω	0.35 Ω	0.14 Ω
Inductance in parallel @ 60 Hz	117.7 mH	80.7 mH	34.3 mH	2.1 mH
Gap volume	8.2 cm^3	4.6 cm^3	4.6 cm^3	3.6 cm^3
Maximum current	14 A	11 A	20 A	40 A
Maximum field	6 kOe	7.2 kOe	6.6 kOe	8 kOe

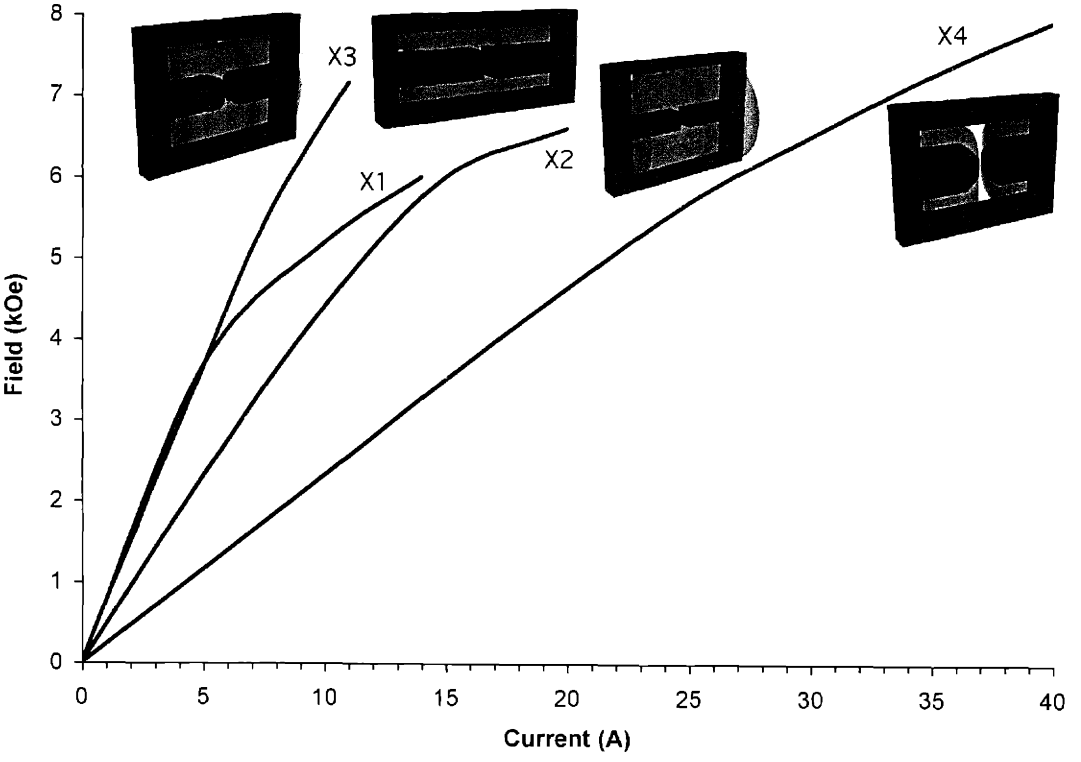

Figure C.1: Magnetic field versus current for each electromagnet revision, X1 through X4.

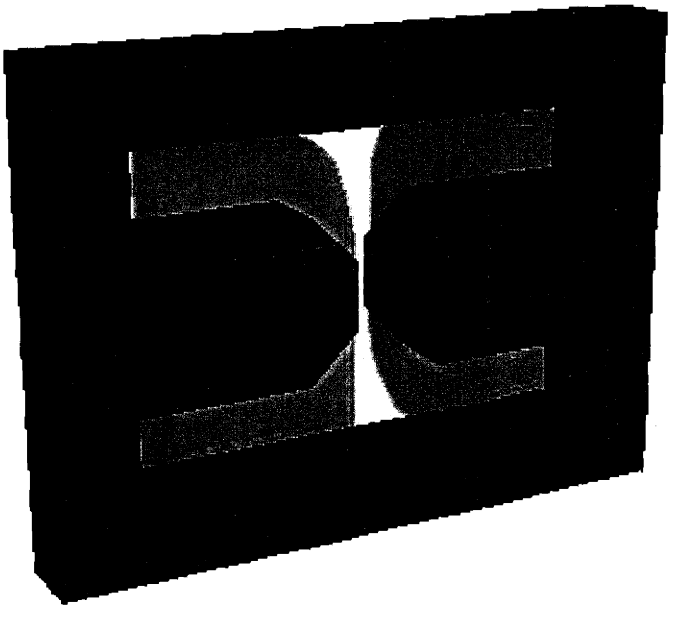

Figure C.2: Rendering of the X4 electromagnet. It acheived 8 kOe in the middle of the 1.1 cm gap at 40 A with 280 total turns with 10 AWG copper wire. The field calculated from $H = NI / gap = 1.4T$

Inductance is a difficult parameter to design an electromagnet around because of numerous design issues: tradeoff of the magnetic core dimensions versus coil size, tradeoff of the wire size and the number of turns, inductive reactance, eddy currents generated in magnetic core, self-inductance, and mutual inductance between each coil and between the coils and the magnetic yoke. In each of the electromagnet revisions the first three issues were considered explicitly and little was done concerning the last two issues.

The main concern for the first issue is that the coil should not saturate the magnetic core. If the magnetic core cross section is too small or if the size of the coil too large, the magnetic core will be saturated. Thus, the magnetic core cross section cannot be made too small compared to the size of the coil. This implies that a smaller coil is desired which reduces the inductance. The main concern for the second issue is that the magnetic field is proportional to the number of turns and the current, but the inductance is also proportional to the number of turns squared. For a high bandwidth electromagnet, the inductance needs to be as low as possible. However, as a number of turns decreases so does the magnetic field. So the current needs to increase proportionally to the decrease in number of turns so that the magnetic field remains constant. This issue is a primary concern for sizing the power supply.

The maximum magnetic field determines the maximum output current to the power supply, and the inductance determines the output voltage of the power supply necessary to achieve a certain bandwidth of the electromagnet. The main concern for eddy current generation is the uninterrupted cross sectional area of the magnetic core. Currents circulating around magnetic flux lines in the magnetic core produce heat and reduce magnetic induction through the core. In order to minimize these currents and without increasing the size of the coil, the magnetic core cross sectional area is composed of 0.014 in. thick MgO coated transformer laminations. Self-inductance and mutual inductance are functions of the complete electromagnet design. Complex expressions exist for self and mutual inductance, however the total inductance is usually just measured experimentally.

Electromagnet X1 was used with a 1 kW Crown Power Amplifier with output impedance of 10 Ω. For AC actuation testing, the electromagnet and the power supply were used in conjunction with 1–10 μF capacitors. Testing frequencies were chosen such that electrical resonance achieved maximum possible current and therefore field. Electromagnets X2 and X3 were never used for AC actuation testing. However, their properties measured with DC power supplies. Electromagnet X4 was incorporated into a second revision AC actuation testing apparatus (shown in Figure 2.3) with a 5 kW, 1.75 Ω output impedance power supply built to drive it.

As with any electrical load, the electromagnet must be matched to the power supply. Under DC operation this is an easy task, the maximum current rating of the windings and the voltage needed to drive that current, I and V in $R = V / I$ determine the necessary DC impedance requirements of the power supply. This DC impedance is the source of ohmic heating of the electromagnet and in turn, heating is the source of a temperature related resistance increase. The DC impedance is usually very small in comparison to the AC component and therefore the power supply virtually sees a short circuit under DC conditions. Therefore, the power supply must dissipate nearly the full load at full power (nearly 5kW dissipated!).

However in AC operation, not only must the DC impedance be included, but so must the AC inductive reactance of the electromagnet, $j\omega L$. During AC operation, power supply impedance is determined by the angular frequency, ω , and the inductance, L, in Equation F.1. The AC component of the impedance increases linearly as the frequency is increased shown in Figure C.3. Thus, the power supply specifications rely upon the current, voltage, and inductance of the electromagnet design.

$$Z = \frac{V}{I} + j\omega L \qquad \text{C.1}$$

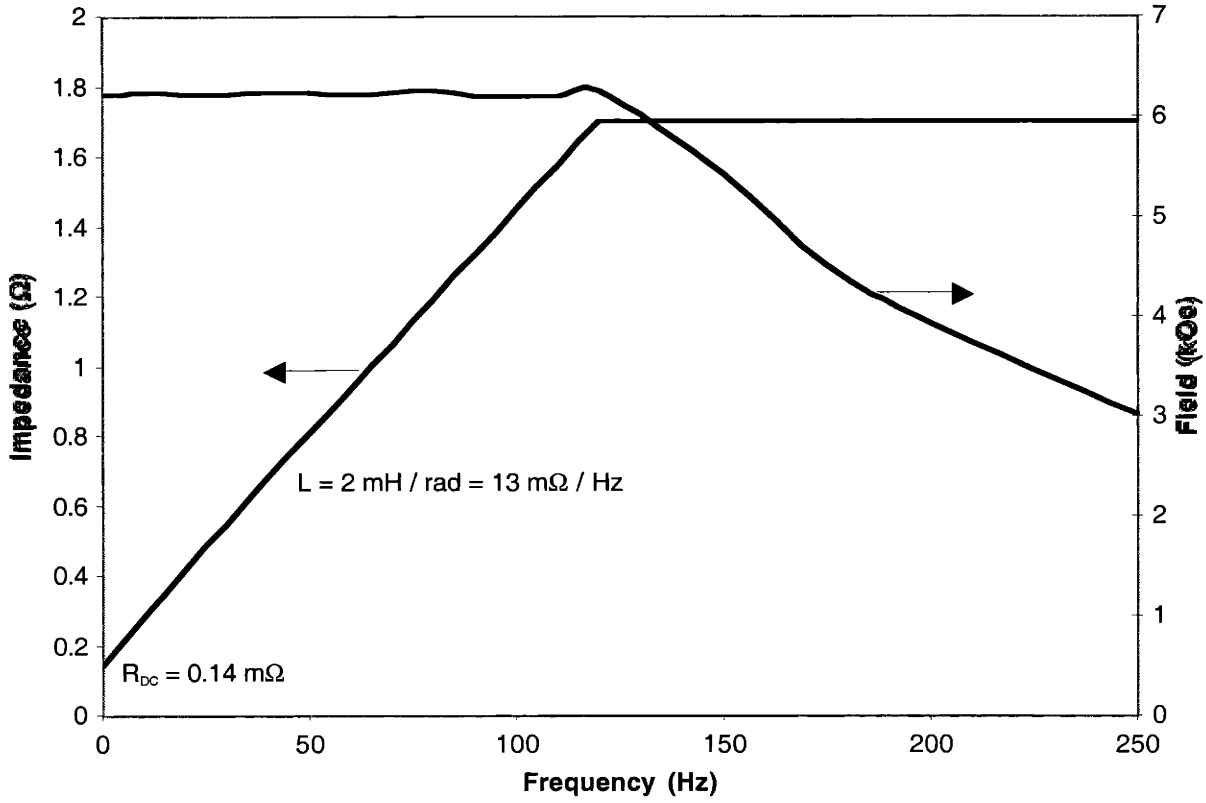

Figure C.3: Impedance and field for electromagnet X4 versus frequency used with a 5kW power supply with a 1.75 Ω ouput impedance. Above 110 Hz the inductive reactance starts to diminsh the maximum field.

Appendix D

D ADDITIONAL INTERESTING DYNAMIC MFIS ACTUATION MEASUREMENTS

This section contains data that is referenced by other plots in the main text but is not used explicitly. A synopsis is provided for the figures in this section.

D.1 STRAIN VS. FIELD FOR SAMPLE A AT 2 HZ, $N \approx 1000$ CYCLES

The first stress-dependent strain vs. field data set in Figure D.1 is from sample A after only $N \approx$ 1,000 cycles and will be compared with the $N \approx$100,000 cycles data to show evidence of fatigue in the next chapter. The second stress-dependent strain vs. field data set in Figure D.2 illustrates the MFIS actuation behavior in sample B after about $N \approx$ 100,000 cycles and is used for the frequency-dependent tests.

The left side of Figure D.1 is labeled with larger increasing bias stress values for which maximum MFIS grows. The right side of Figure D.1 is labeled with larger increasing bias stress values for which maximum MFIS is increasingly blocked. In this figure, extensional strain is measured such that zero strain is the compressed state during steady-state operation. As mentioned in Chapter 2, no reference strain state was maintained between tests in this family.

A load cell was not present in the X1 DATS hardware, but the stress is estimated (from spring displacements) to increase from 0.13 MPa to 2.2 MPa. Experience indicates that the actual maximum stress developed during straining may be up to 2 times larger

than is estimated. However, it is also possible that the sample twin-boundary yield stress became higher and the range of stresses over which twinning occurs changed as the sample cycled. Thus, the bias stress labels indicate the approximate lower bound of the applied stress.

During actuation under the smallest bias stress, 0.13 MPa, the field is capable of fully extending the sample, but the back force generated in the spring cannot compress the sample by shrinking the field-actuated variants. At such low stresses the twin-boundary yield stress has not yet been exceeded in the majority of variants aligned perpendicular to the field. The resulting steady-state MFIS is only 0.3%. At an intermediate stress of 0.64 MPa, a greater proportion of field-actuated variants are compressed in response to a greater spring compression, increasing the total actuation strain to 1.8%. Figure D.1 shows increasing MFIS up to bias stresses of 1.4 MPa, at which point the reversible steady state MFIS is 3.0%. At a bias stress of 1.67 MPa the strain drops to 2.75% because larger spring compressions start to prevent field-actuated variants from responding fully to the field. As the bias stress is increased to 2.2 MPa, the field-induced strain becomes increasingly blocked so the net MFIS decreases to about 0.6%. The twin-boundary coercive field at one-half maximum strain is noticeably smaller for bias stresses less than 1.67 MPa than for greater bias stresses in which mechanical blocking of MFIS occurs. See

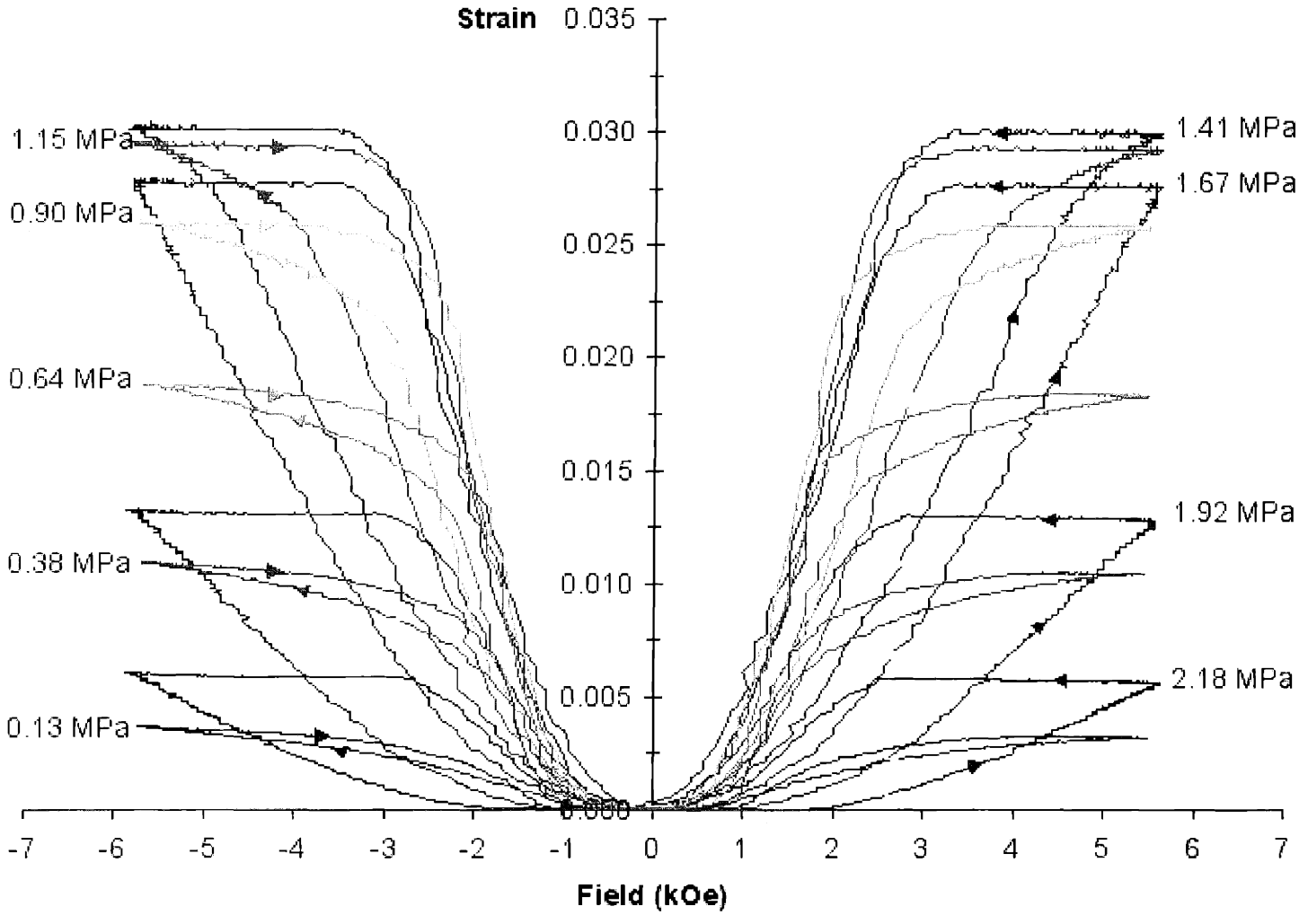

Figure D.1: Sample A on revision X1, N=1000 cycles. Steady-state strain versus magnetic field at 2 Hz response for the spectrum of applied stresses that give magnetic-field-induced strain.

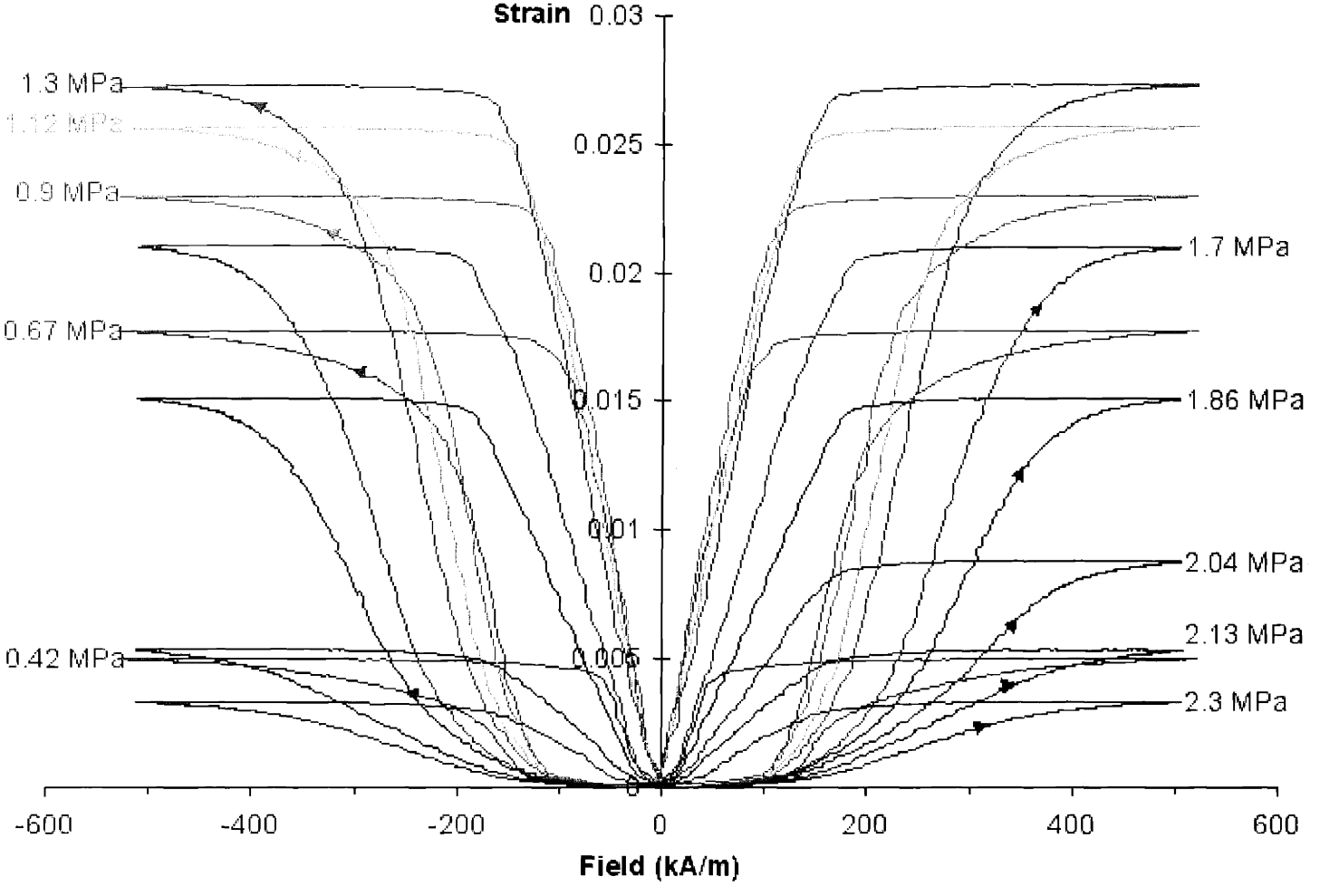

Figure D.2: Sample B on revision X4, N~100,000 cycles. Steady-state strain versus magnetic field at 2 Hz response for the spectrum of applied stresses that give magnetic-field-induced strain.

D.2 COERCIVE FIELDS IN STRAIN VS. FIELD BEHAVIOR

Figure D.3 and Figure D.4 show the strain vs. field coercivity versus applied bias stress at different strain levels for sample A at $N \approx 1000$ cycles and $N \approx 100{,}000$ cycles respectively. Both plots exhibit similar behavior. The coercive field is measured at three locations: at the maximum strain (square symbols), half maximum strain (triangles), and minimum strain (diamond symbols). The top curve represents the coercive field of the mechanism that is responsible for pinning the sample in its elongated state.

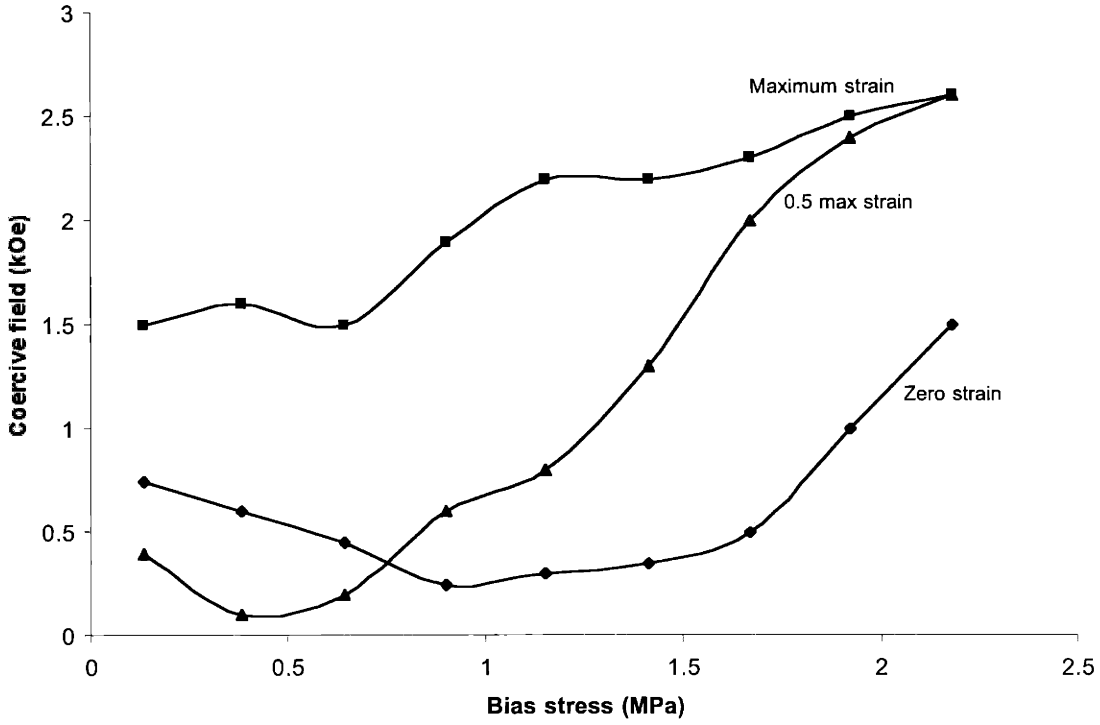

Figure D.3: For sample A and $N \approx 1000$ cycles, strain vs. field coercive field at three strain states: maximum field-induced strain (square symbols), minimum spring compression strain (diamond symbols), and half maximum strain (triangles). The coercive field changes its character from

low bias stress where it is more like the zero strain coercivity to high bias stress where it is more like the maximum strain coercivity.

One likely candidate mechanism is that the applied stress is concentrated at certain defects preventing twin-boundary motion. The bottom curve may represent a different mechanism to pin the sample in its compressed state. The defects pinning 90° domain walls may be different than those pinning twin boundaries by type or energy. The middle curve is measured in the middle (at 0.5 × maximum strain) and seems have a mixed character. But it shows minimal coercive fields of nearly 100 kA/m in the range from 0.5 to 1.85 MPa and is minimized at 1 MPa. Above 1.85 MPa, the coercive field increases in a linear fashion. Thus, one could attribute some or all of this behavior to magnetostriction.

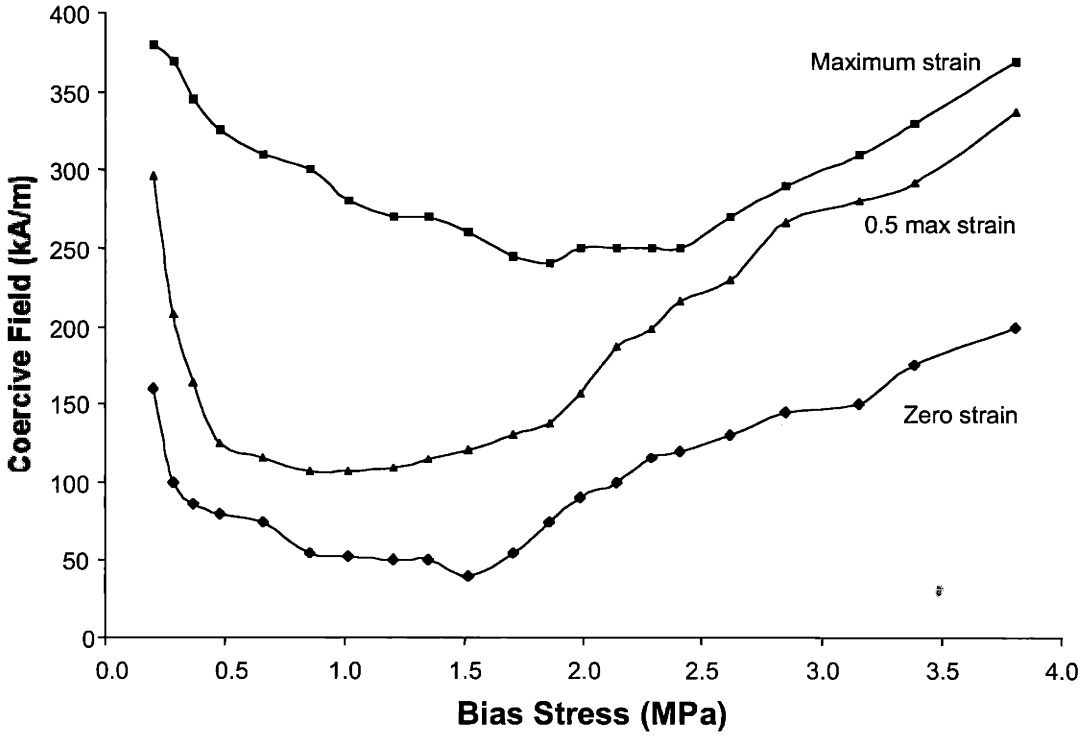

Figure D.4: For sample A and $N \approx 100{,}000$ cycles, strain vs. field coercive field at the maximum field-induced strain (square symbols), at the minimum spring compression strain (diamond symbols), and at the half maximum strain (triangles). The coercive field changes its character from low bias stress where it is more like the zero strain coercivity to high bias stress where it is more like the maximum strain coercivity.

At bias stresses lower than 1.85 MPa, the coercive field is closer to the lower coercivity curve, possibly suggesting that a magnetostrictive-like hysteresis mechanism of the lower curve is dominant in the sample as a whole. But at stresses greater than 1.85 MPa, the coercivity is closer to that of the upper curve, possibly suggesting a mechanical compression mechanism dominates hysteresis in the sample. In other Ni–Mn–Ga

samples, the apparent "coercive field" is noticeably smaller at comparable stresses less than 1.5 MPa like in Figure D.4.

The frequency dependent coercive field versus frequency is shown in Figure D.5. It shows the frequency that maximizes the energy loss occurs at 350 Hz.

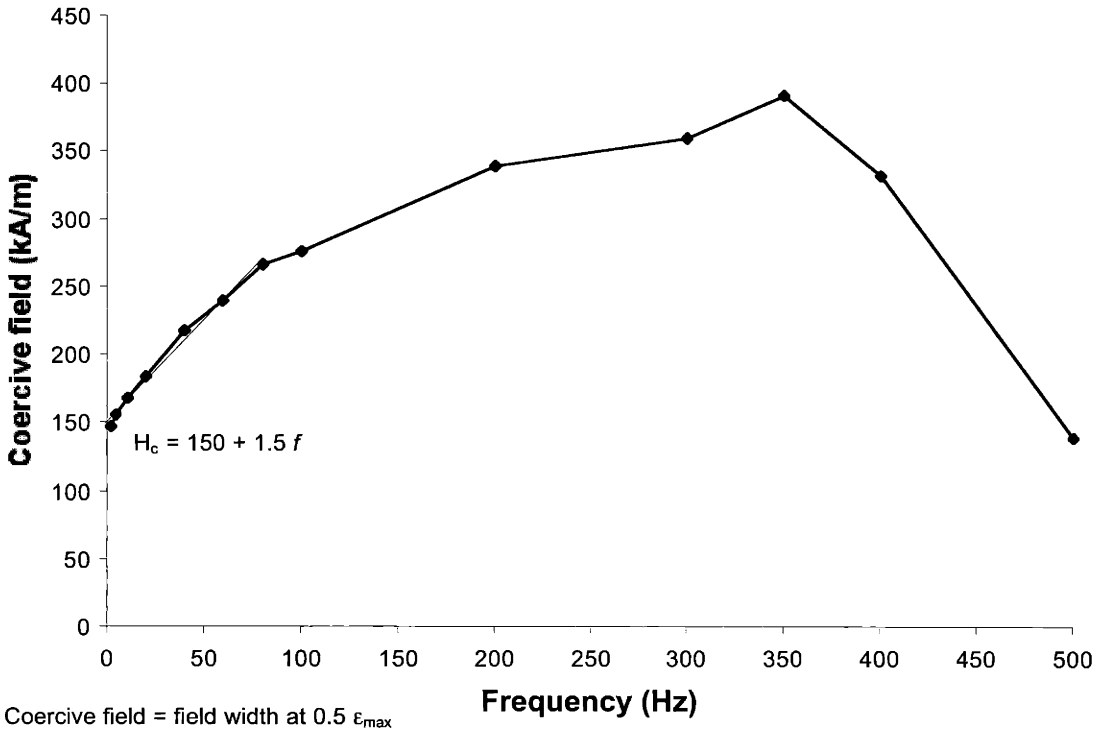

Figure D.5: Coercive field from Figure 3.13 and Figure 3.14 versus actuation frequency. Initial frequency dependence of the coercive field is linear.

D.3 MAGNETIZATION VERSUS FIELD DATA UP TO 250 HZ

Magnetization versus applied magnetic field plots are shown in Figure D.6 for frequencies between 1 Hz up to 100 Hz and in Figure D.7 for frequencies between 100

Hz and 250 Hz. These measurements were taken at a bias stress of about 1.1 MPa and are uncorrected for demagnetization fields. These plots retain the same saturation magnetization through 150 Hz though all of the curves are displaced along the x-axis. Power supply bandwidth limitations prevented sufficient fields to saturate the sample. Vertical displacement was done to facilitate comparisons within the family of curves.

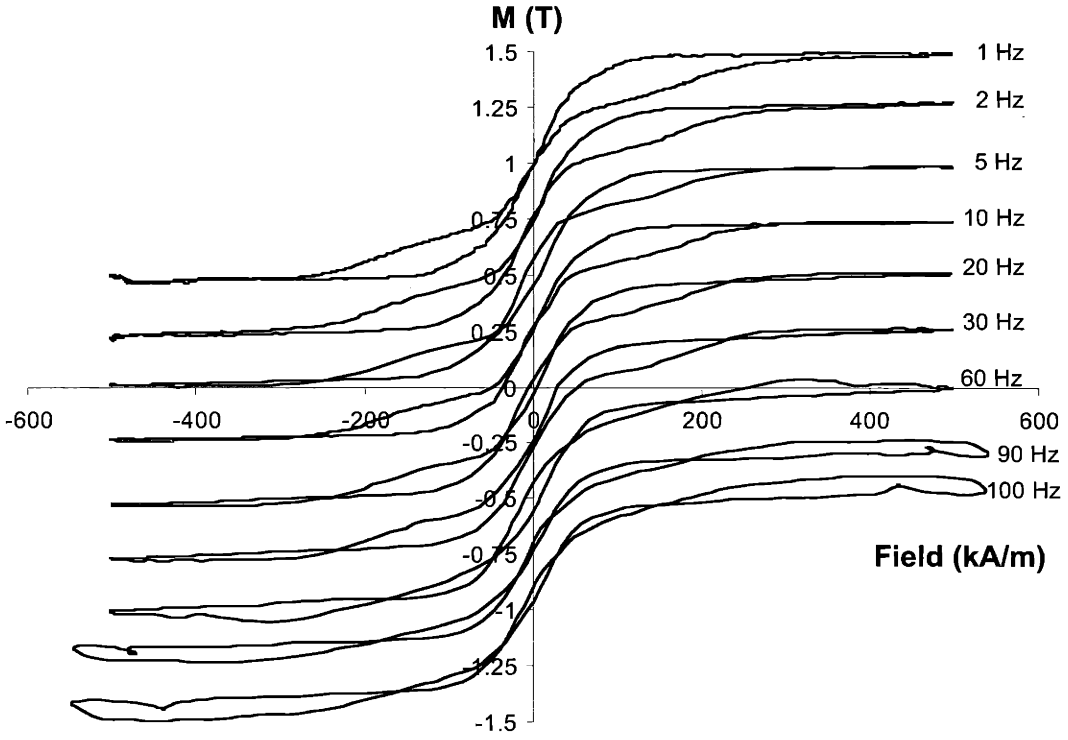

Figure D.6: Family of magnetization versus applied field for drive frequencies from 1 to 100 Hz. Though x-axis displacement of each curve is to facilitate easy visual comparison, saturation magnetizations are consistently about 0.55T.

In each of these plots, easy-axis magnetization occurs up to about 50 kA/m with a susceptibility of approximately 4. In increasing fields from 50 kA/m to about 250 kA/m

the susceptibility drops to 1 during hard-axis magnetization. Above about 300 kA/m, sample magnetization saturates at approximately 0.55 T. As the field reverses the magnetization remains saturated until the field decreases to about 150 kA/m. The susceptibility rises again to about 4 as the field decreases below 50 kA/m. These trends show to be consistent and relatively frequency independent throughout the family of curves.

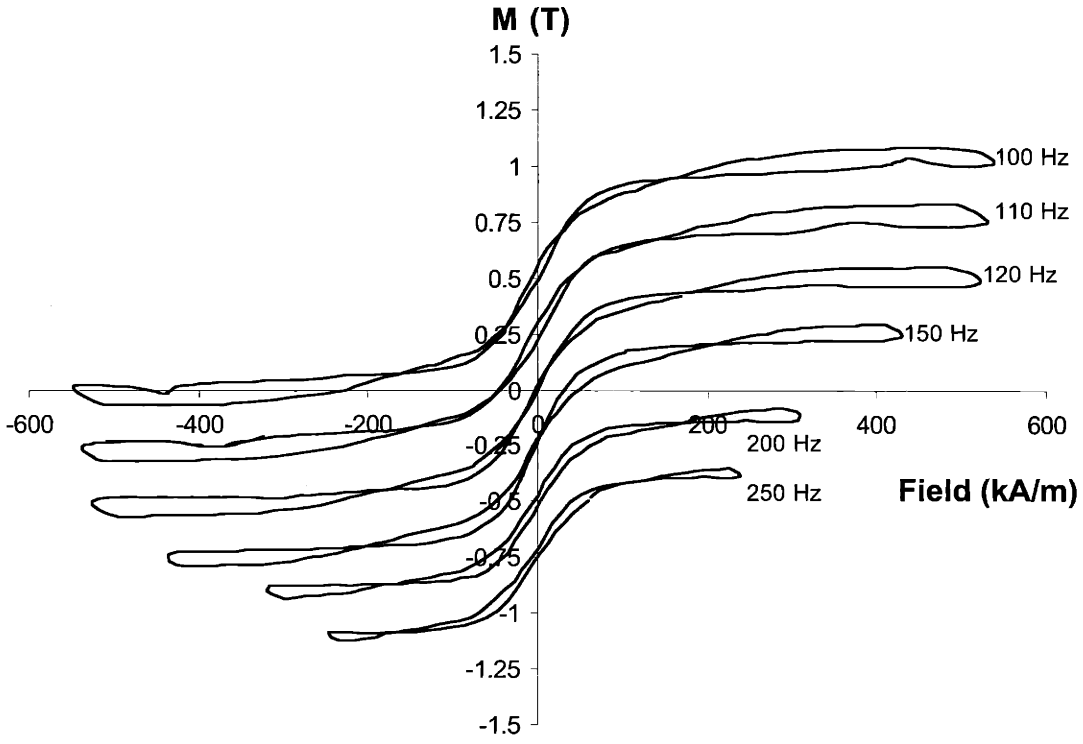

Figure D.7: Magnetization versus applied field for drive frequencies for 100 to 250 Hz. Vertical shifting of each curve is so that a visual comparison could easily be made. Again the bandwidth limitations of the electromagnet are evident

There are several aspects of this family of data, which should be explained. First, the high, decreasing field bumps in the magnetization for the 90 Hz through 120 Hz curves are an artifact from discontinuities in power when approaching the supply bandwidth. Second, the loops start opening up at 20 Hz, but in the opposite sense one might expect. If a phase lag existed between the magnetization and the field, then the magnetization would continue to increase as the field reverses direction. In this circumstance, the magnetization drops as the field reverses direction. This could be the result of compressive stresses at a high field could promote minor variant reorientation or a converse magnetostrictive effect. By 100 Hz, magnetization versus field loops stop opening any further and the magnetization loss remains constant at about 0.1 T.

BIBLIOGRAPHY

1 A. A. Bent, Department of Aeronuatical and Astronautical Engineering, MIT Ph.D. Thesis (1997).

2 S. J. Murray, M. Marioni, S. M. Allen, R. C. O'Handley and T.A. Lograsso, *Applied Physics Letters* **77** (6) (2001).

3 A. Sozinov, A. A. Likhachev, N. Lanska, K. Ullakko, V. K. Lindroos, "Crystal structure, magnetic anisotropy, and mechanical properties of seven-layered martensite in Ni–Mn–Ga," *SPIE Smart Structures and Materials Proceedings* **4699**, (2001) 189.

4 A. Sozinov, A. A. Likhachev, K. Ullakko, "Magnetic and magnetomechanical properties of Ni–Mn–Ga alloys with easy-axis and easy-plane of magnetization," *SPIE Smart Structures and Materials Proceedings* **4333**, (2002).

5 J. Pons, V. A. Chernenko, R. Santamarta, and E. Cesari, *Acta mater.* **48** (2000) 3027–3038.

6 E. Cesari, V. A. Chernenko, V. V. Kokorin, J. Pons, and C. Seguí, *Acta Mater.*, (1997), **45**, 999.

7 M. Khantha, V. Vitek, D. P. Pope, "Atomistic modeling of planar faults, dislocations and twins in a non-cubic intermetallic compound," *Modelling Simult. Mater. Sci. Eng.* **2** (1994) 587–596.

8 Unpublished study, February 2002.

9 M. De Greaf, M .A. Willard, M. E. McHenry, and Y. Zhu, "*In-situ* TEM cooling study of magnetic domain configurations in Ni_2MnGa," *IEEE Transactions of Magnetics*, **37**, No. 4, (2001) 2663–2665.

10 S. J. Murray, Department of Materials Science and Engineering, MIT Ph.D. Thesis (2000).

11 Webster, P. J., Ziebeck, K. R. A., Town, S. L. and Peak, M. S., *Phil. Mag. B* **49**, No. 3, 295–310 (1984).

12 V.V. Kokorin and V.V. Martynov, "The crystal structure of thermally- and stress-induced martensites in Ni_2MnGa single crystals." *J. Phys. III France* **2** 739-749 (1992).

13 V. A. Chernenko, and V. V. Kokorin, in *Proc. Int. Conf. on Martensitic Transf.*, ed. C. M. Wayman and J. Perkins. Monterey Institute of Advanced Studies, USA, p. 1205, (1992).

14 V. A. Chernenko, E. Cesari, V. V. Kokorin, and N. Vitenko, *Scrip. Met. et Mater.* **33**, 1239 (1995).

15 V. V. Kokorin, V. A. Chernenko, E. Cesarí, J. Pons, and C. Seguí, *J. Phys.: Condens. Matter*, (1996), **8**, 6457.

16 Chernenko, V. A., Seguí, C., Cesari, E., Pons, J. and Kokorin, V. V., *J. de Physique IV*, (1997), **7**, C5–137.

17 Chernenko, V. A., Seguî, C., Cesari, E., Pons, J. and Kokorin, V. V., *Phys. Rev. B*, (1998), **57**, 2659.

18 J. Pons, C. Seguí, C., Chernenko, V. A., Cesari, E., Ochin, P. and Portier, R., *Mater. Sci. Eng. A*, **273-275**, (1999) 315.

19 J. Pons, V. A. Chernenko, R. Santamarta, and E. Cesari, *Acta mater.* **48** (2000) 3027–3038.

20 Manosa, Ll, Gonzalez-Comas, A., Obrado, E., Planes, A., Chernenko, V. A., Kokorin, V. V. and Cesari, E., *Phys. Rev. B*, (1997), **55**, 11068.

21 R. D. James and D. Kinderlehrer, *Philos. Mag. B* **68**, 237, (1993).

22 R. D. James and M. Wuttig, *SPIE Smart Structures and Materials Proceedings* **2715**, (1996) 420.

23 R. D. James and M. Wuttig, "Magnetostriction of martensite," *Phil. Mag A*, (1998)

24 R. Tickle and R.D. James, *Journal of Magnetic Materials* **195**, 627 (1999).

25 K. Ullakko, J.K. Huang, C. Kantner, V.V. Kokorin and R.C. O'Handley, *Applied Physics Letters* **69** (13) (1996).

26 K. Ullakko, J. K. Huang, V.V. Kokorin and R.C. O'Handley, *Scripta Mat.*, **36** pp. 1133 (1997).

27. K. Ullakko, *Journal of Materials Engineering Performance* **5**, 405 (1996).

28. K. Ullakko, "New developments in actuator materials as reflected in magnetically controlled shape memory alloys and high-strength shape memory steels", *SPIE Smart Structures and Materials Proceedings* **2715** pp.42–50 (1996)

29. R.D. James and M. Wuttig, *Phil. Mag A*, (1998)

30. R. Tickle and R.D. James, *Journal of Magnetic Materials* **195**, 627 (1999).

31 R.D. James, R. Tickle, M. Wuttig, :*Materials Science and Engineering A* **273–275**, (1999) 320–325.

32 M. Pasquale, C. Sasso, S. Besseghini, F. Passaretti, E. Villa, and A. Sciacca, "NiMnGa Polycrystalline Magnetically Activated Shape Memory Alloys," *IEEE Transactions on Magnetics* **36**, No. 5, (2000) 3263–3265.

33 S. J. Murray, M. Farinelli, C. Kantner, J. K. Huang, S. M. Allen, and R. C. O'Handley, "Field induced strain under load in Ni–Mn–Ga in magnetic shape memory materials," *Journal of Applied Physics* **83**, No. 11 (1998) 7297-7299.

34 S. J. Murray, R. Hayashi, M. Marioni, S. M. Allen, and R. C. O'Handley, "Magnetic and Mechanical Properties of FeNiCoTi and NiMnGa Magnetic Shape Memory Alloys," *SPIE Smart Structures and Materials Proceedings*, Vol. 3675 (1999) p.25.

35 S. J. Murray, R. C. O'Handley, and S. M. Allen, "Model for discontinuous actuation of ferromagnetic shape memory alloy under stress," *Journal of Applied Physics* **89**, No. 2 (2001) 1295–1301.

36. K. Ullakko, Personal communication, October (1999).

37 O. Heczko and K. Ullakko, "Effect of temperature of magnetic properties of Ni–Mn–Ga magnetic shape memory (MSM) alloys," *IEEE Transactions on Magnetics*, **37**, No. 4, (2001) 2672–2674.

38 R. C. O'Handley, *Modern Magnetic Materials: Principles and Applications*, John Wiley, New York, (1998).

39 J. R. Cullen, J. P. Teter, M. Wun-Fogle, J. B. Restorff, *IEEE Transactions of Magnetics*, **33**, No. 5, (1997) 3949–3951.

40 Etrema documentation, "Better Sonar Driven by New Transducer Materials Origins & Important Differences Between Available Transducing Materials; TERFENOL-D, PZT, and Nickel," http://etrema-usa.com/terfenol/index.asp (Feb 2002).

41 J. B. Restorff, M. Wun-Fogle, J. P. Teter, J. R. Cullen, A.E. Clark, *IEEE Transactions of Magnetics*, **32**, No. 5, (1996) 4782–4784.

42 R. D. Greenough, A. J Wilkinson, R. J Smith, A. G. Jenner, "Controlled Magnetostrictive Actuation and Applications," Institution of Electrical Engineers, U.K., 1998.

43 Y.-M. Chiang, G. W. Farrey, A. Soukhojak, *Appl. Phys. Lett.*, **73**, (1998) 3683.

44 Webster, Peter; *Contemporary Physics*, **10**, No. 6, 559–577, (1969).

45 W. H. Wang, F. X. Hu, J. L. Chen, Y. X. Li, Z. Wang, Z. Y. Gao, Y. F. Yheng, L. C. Zhao, G. H. Wu, W. S. Zan, "Magnetic properties and structural phase transformations of NiMnGa alloys, *IEEE Transactions of Magnetics*, **37**, No. 4, (2001) 2715–2717.

46 X. J. Jin, M. Marioni, D. Bono, S. M Allen, R. C. O'Handley, T. Y. Hsu, "Empirical mapping of Ni-Mn-Ga properties with composition and valence electron concentration," *J. of Appl. Phys.*, special MMM proceedings, Nov. 2001.

47 C. Henry and S. Murray, unpublished stress-versus-strain data of different single crystal Ni–Mn–Ga compositions.

48 R. D. James and M. Wuttig, "Magnetostriction of martensite," *Phil. Mag A*, (1998)

49 R. C. O'Handley, "Model for strain and magnetization on magnetic shape memory alloys," *Journal of Applied Physics,* **83**, No. 6 (1998) 3262-3270.

50 A. A. Likhachev, K. Ullakko, "Magnetic-field controlled twin boundaries motion and giant magneto-mechanical effects in Ni–Mn–Ga shape memory alloys," *Physics Letters A,* **275**, (2000) 142–151.

51 V. A. L'vov, E. V. Gomonaj and V. A. Chernenko, "A phenomenological model of ferromagnetic martensite," *J. Phys.: Condens Matter,* **10**, No. 6 (1998) 4587–4596.

52 A. N Soukhojak and Y.-M. Chiang, "Generalized rheology of active materials," *J. Appl. Physics,* **88**, 6902 (2000).

53 R.D. James and Kinderlehrer, *Journal of Applied Physics*. **76**, 7012 (1994)

54 R. C. O'Handley, S. J. Murray, M. Marioni, H. Nembach, and S. M. Allen, "Phenomenology of magnetic-field-induced strain in ferromagnetic shape memory materials," *Journal of Applied Physics* **87**, No. 9 (2000) 4712–4717.

55 C. Henry, unpublished from Fall 2001.

56 S.-Y. Chu, R. Gallagher, M. De Graef, and M. E. McHenry, "Structural and magnetic phase transitions in Ni–Mn–Ga ferromagnetic shape memory crystals," *IEEE Transactions of Magnetics*, **37**, No. 4, (2001) 2666–2668.

57 A.E. Clark, J.P. Teter, and O.D. McMasters, *J. Appl. Physics,* **63**, 3910 (1988).

58 Bozorth, Ferromagnetism, 1951.

59 R.C. O'Handley, unpublished coercive field data on magnetostrictive amorphous alloys.

60 D. I. Paul, "General theory of the cohesive force due to domain wall pinning," *Journal of Applied Physics* **53**, (1982) 1649.

61 M. E. Lines and A. M. Glass, *Principles and Applications of Ferroelectrics and Related Materials* , Clarendon Press, New York, (1977).

62 Blinc and Zeks, *Soft Modes in Ferroelectrics and Antiferroelectrics*, Elsevier, New York, (1974).

63 J. Nakata, Y. Terada, S. Takizawa, K. Ohkubo, T. Mohri, and T. Suzuki, "Thermal conductivity in X_2YZ Heusler type intermetallic compounds," *Materials Transactions, JIM*, **37**, No. 3, (1996) 442–447.

64 T. Beckwith, R. Marangoni, and J. Lienhard, *Mechanical Measurements, Fifth Ed.*, Addison-Wesley, New York, (1993).

65 M. D. Mermelstein, "Coupled mode analysis for magnetoelastic metal sensors," *IEEE Transactions of Magnetics*, **22**, No. 5, (2001) 442–444.

66 AdaptaMat Materials Specifications Sheet for Ni–Mn–Ga, May 2001.

67 A. Soukhojak and Y.M. Chiang, "Generalized rheology of active materials," *J. Appl. Physics,* **88**, (2000) 6902.

68 K. Uchino and S. Hirose, *IEEE Transactions on Ultrasonics, Ferroelectrics, and Frequency Control*, **48**, No. 1, (2001) 307–321.